DIRECTED SELF-ASSEMBLY OF FERRITIN NANOCAGES BY SURFACE-REDESIGNED CARGO

Joshua A. Bulos

A DISSERTATION

in

Chemistry

Presented to the Faculties of the University of Pennsylvania

in

Partial Fulfillment of the Requirements for the

Degree of Doctor of Philosophy

2022

Supervisor of Dissertation

_____

Ivan J. Dmochowski

Alan MacDiarmid Term Professor of Chemistry

Graduate Group Chairperson

_____

Daniel J. Mindiola

Brush Family Professor of Chemistry

Dissertation Committee

Jeffery G. Saven, Professor of Chemistry
E. James Petersson, Professor of Chemistry
David M. Chenoweth, Professor of Chemistry

DIRECTED SELF-ASSEMBLY OF FERRITIN NANOCAGES

BY SURFACE-REDESIGNED CARGO

ACKNOWLEDGMENT

Nobody completes a PhD alone. It took the support of a lot of great people to mold me into the scientist I am today. First and foremost, I would like to thank Prof. Ivan J. Dmochowski, my dissertation advisor, for taking me into his lab, for all his guidance and mentorship. I appreciate how his door is always open and he seems to respond to emails at any hour of the day to help us. He always encourages us to take our projects in directions that we are passionate about, and he never stops inspiring us to push the limits of what we imagine is possible on our projects.

I would also like to thank my committee members, Prof. Jeffery G. Saven, Prof. E. James Petersson, and Prof. David M. Chenoweth. They helped me approach my project from outside of the lens of my own lab's expertise and provided me with a diverse set of opinions. They always had great advice every time I would meet with them, both in official capacities in my committee meetings or running into them in the hallways.

I couldn't ask for a better group of labmates. Although we had people from all four divisions in Penn Chemistry, we somehow found the nicest people every year. Not only were people happy to help each other at the drop of a hat with your science, but they were enjoyable to work alongside every day. I could not have accomplished everything I did without the help and advice of all of team ferritin, past and present: Katie Pulsipher, Zhiheng Wang, Yiwen Wang, Anuraj Sinha, Felix Nnaji, Zoeb Mohammedshah, and Maggie DeLessio. I'd like to give special thanks to Katie for teaching me everything she knew about ferritin in the few short months we overlapped in the lab even though she was trying to finish writing her dissertation. Serge Zemerov made me feel especially welcome from day one, bringing me to many social events and inviting me to participate in whatever creative endeavors he was pursuing. I'd like to thank current members Yannan Lin, Zhuangyu Zhao, Nathan Rudman, Zhiheng Wang, Dora von Trentini, Madison Herling, Jiayi He, Mina Ahmadi, Aria Fodness, Jason Marmorstein, and Stephen Crane as well as former members Teresa Rapp, Sean Yeldell, Benjamin Roose, Linlin Yang, Kang Du,

Madison Stringer, Kelsey Farenhem, Mara Greenberg, and Jordan Farina. I do not have the space to highlight how much each of these individuals has helped me along the way.

I've had the opportunity to work with a lot of great collaborators throughout my time at Penn. I'd like to extend monumental thanks Rui Guo from Prof. Jeffery Saven's lab for all of her work designing all of the novel supercharged proteins in this work. Without her help, none of this work would have been possible. It has been an honor to work with Vladimir Shuvaev from Prof. Vladimir Muzykantov's lab, he was always an enthusiastic collaborator in using ferritin for drug delivery. Benjamin Roose was a fantastic collaborator both when he was a member of our lab and as a postdoctoral researcher in Prof. David Christianson's lab working on crystallizing ferritin. He was always willing to screen any sample and meticulously helped me troubleshoot any problem I came across, whether it was for a collaboration we had together or an issue I was facing for a completely different project. After Ben left, Trey Ronnebaum and Matt Gaynes were both happy to work on my crystals. It has been fascinating to see how small mutations in ferritin can have such large impacts on structure, function, and overall health in humans ever since Prof. Xilma Ortiz-Gonzalez approached us in early 2020 about modeling ferritin in a novel disease. In the wake of SARS-CoV-2, working with Mark Yarmarkovich from Prof. John Maris' lab has led us in interesting directions with using ferritin as an antigen-presenting platform, even if we never completed the project. I would also like to thank Natalie Gogotsi from Prof. Chris Murray's lab for supplying us with interesting nanoparticles and helping us to continue exploring nanoparticle encapsulation.

There are many peers I need to thank in the department who I didn't collaborate with but taught me new techniques, threw ideas around with me, or were just good friends. These include my former roommates (and fellow scientists) Sam Melton, Dan Wu, Martin Iwanicki (not technically in the department but department-adjacent), former rotation mentors Alex Kasznel and Miklos Robkis, and other graduate students and postdocs Jack Ferrie, Marshall Lougee, Kristen Fiore, Chloe Jones, Sam Giannakoulias, Hoang-Anh Phan, Marie Shimogawa, Ryann Perez, Kyle Shaffer, Jaclyn Robustelli, Taylor Barrett, Joomyung Jun, Chris Walters, Jacque Faylo,

Jeremy Osko, Nick Porter, Corey Herbst-Gervasoni, Andy Glass, Mike Gau, Russell Shelp, Jay Aonbangkhen, Roy Malamakal, Jiawei Liu, Alec Coffman, Sunbin Deng, Sam Brooks, Phil Gilmartin, Ariana Spentzos, Alison Knasin, Paris Watson, Shiv Govind, Alex Weberg, and probably a million other people I'm forgetting.

There are countless other people in the department to thank who keep everything running smoothly and with whom I've interacted with various frequencies: Chris Jeffrey, Kersten Forsthoefel, Judith Currano, Kristen Simon, Dan Burke, Rico Vargas, Jon Burke, Yvonne Kline, Candice Adams, Cuong Nguyen, Andrei Korchynsky, Anna Boffice, Carol Hartranft, and Casey Celious. I'd like to highlight all the work that Ryan Kubanoff has done in training everyone to use the BCRC instruments and for keeping them running smoothly. I'd also like to thank Nadine Gruhn and Prof. Karen Goldberg for selecting me to be one of the inaugural graduate fellows for VIEST.

Choosing to pursue science started much earlier than graduate school. I was blessed to have truly fantastic science teachers in high school whose enthusiasm for science helped kindle my own. I would especially like to thank Thomas McNamara in chemistry, Jay Chugh in biology, and Laura Guthrie in physics. When I initially started at Haverford College, I thought I wanted to major in biology. While my eventual major of chemistry with a concentration in biochemistry wasn't a far reach from biology, I really enjoyed approaching biochemistry from the chemistry side. I could tell that the entire chemistry faculty at Haverford really enjoyed teaching, and it showed starting from day one when I walked into general chemistry lecture with Prof. Alexander Norquist and advanced general chemistry lab with Prof. Casey Londergan. Prof. Lou Charkoudian's passion for science was familiarly infectious and she always believed in me. I am grateful that she took me into her lab and mentored me for my undergraduate research and thesis. I'd be remiss not to mention key peers who helped along the way. Niki von Krusenstiern taught me a lot about research as an undergraduate. I never would have gotten through physical or quantum chemistry without the help of Noah Bloch, Neal Patel, Luis Rivas, and countless sleepless nights working on problem sets.

I’m thankful for my friends and family who have supported me throughout this entire process. My adopted Philadelphia family in After the Bar was integral to giving me an outlet to pursue leisure outside of chemistry and they ended up becoming some of my best friends. I’m so lucky my parents have always supported me in every endeavor and encouraged me to be the best version of myself. Although my sister unintentionally copied me in pursuing a PhD in biochemistry, she pushed me to be the best role model possible. Lastly, I could not have gotten through the final hurdles without my amazing partner, Carly Hecht. She was always brought joy to my life regardless of how well lab work or writing was going.

ABSTRACT

DIRECTED SELF-ASSEMBLY OF FERRITIN NANOCAGES

BY SURFACE-REDESIGNED CARGO

Joshua A. Bulos

Ivan J. Dmochowski

Self-assembling proteins cages are a popular platform for encapsulating, protecting, and delivering a variety of cargo due to their tunability, increased biocompatibility, lower immunogenicity, and added functionality over other synthetic delivery agents. The natural roles of protein cages tend to be for storage and protection, but they can be repurposed for uses as nanoreactors, drug delivery vehicles, and building blocks for supramolecular structures. One of the smallest naturally occurring protein cages is the iron oxidation and storage protein, ferritin. Maxi-ferritins studied here form hollow 24mer assemblies with an outer diameter of 12 nm and an inner diameter of 8 nm at neutral pH and disassemble into dimers at very low or very high pH. Loading non-native cargo into ferritin typically involves a harsh disassembly-assembly process or requires covalent attachment of the cargo inside the cage. One ferritin that can circumvent this challenge is thermophilic ferritin from *Archaeoglobus fulgidus* (AfFtn), which has unique high ionic strength-dependent assembly at physiologic pH. Previous work from our lab and others has shown that specific nanoparticles or the superpositively charged green fluorescent protein, GFP(+36), can direct assembly of the ferritin cage. As described in this work, we computationally designed the first active superpositively charged enzyme, human carbonic anhydrase II, with a theoretical net overall surface charge of +21. This superpositively charged enzyme is able to induce AfFtn 24mer assembly without the need for a GFP(+36) fusion partner or additional reagents. We also investigated the charge magnitude and distribution requirements for protein cargo to initiate formation of the AfFtn cage while also examining the role of pH on cargo-templated assembly. The technologies we developed pave the way for even more generalizable AfFtn loading for the ever-expanding applications of protein nanocapsules.

TABLE OF CONTENTS

Contents

ACKNOWLEDGMENT iii

ABSTRACT vii

LIST OF TABLES x

LIST OF ILLUSTRATIONS xi

CHAPTER 1: INTRODUCTION 1

1.1 Protein Cages 2

1.2 Ferritin 4

1.3 Computational Protein Redesign and Supercharged Proteins 9

1.4 Prospectus 11

CHAPTER 2: DESIGN OF A SUPERPOSITIVELY CHARGED ENZYME: HUMAN CARBONIC ANHYDRASE II VARIANT WITH FERRITIN ENCAPSULATION AND IMMOBILIZATION 12

2.1 Introduction 13

2.2 Materials and Experimental Details 18

2.3 Results and Discussion 26

2.4 Conclusions 37

2.5 Accession Numbers 38

2.6 Funding Sources 38

CHAPTER 3: EXPLORING GFP CHARGE MAGNITUDE AND DISTRIBUTION REQUIREMENTS FOR THERMOPHILIC FERRITIN ASSEMBLY 39

3.1 Introduction 40

3.2 Results and Discussion 42

3.3 Conclusions 53

3.4 Experimental Procedures 53

3.5 Acknowledgments 57

CHAPTER 4: CONCLUSIONS AND FUTURE DIRECTIONS 58

APPENDIX A: FERRITIN MODIFICATIONS 62

A.1 AfFtn in drug delivery 63

A.2 AfFtn protein arrays 65

A.3 AfFtn as a platform for vaccine presentation 68

APPENDIX B: Supplementary Figures 72

BIBLIOGRAPHY 79

LIST OF TABLES

Table 3.1 Zeta potential of GFP variants ……..…….. 46
Table 3.2 Loading number of AfFtn:GFP(+36) at pH 7.6..... 48
Table 3.3 Thermal shift results of AfFtn-GFP at pH 7.6 and 5.8 ……...……..50

LIST OF ILLUSTRATIONS

Figure 1.1. Examples of protein cages. 3
Figure 1.2. Structure of ferritin monomer and 24mer. 5
Figure 1.3. Structures of AfFtn E65r and wt. 8
Figure 1.4. Electrostatic maps of GFPs. 10
Figure 2.1. Renderings of hCAII and hCAII(+21) 28
Figure 2.2. pNPA assay of AfFtn, hCAII wt and hCAII(+21). 30
Figure 2.3. SEC of the 1:1 AfFtn-hCAII(+21) complex in no-salt buffer. 31
Figure 2.4. Native agarose gel of AfFtn and hCAII(+21). 32
Figure 2.5. Ni-NTA binding assay of hCAII(+21) 33
Figure 2.6. Centricon Assay of AfFtn and hCAII(+21). 34
Figure 2.7. pNPA activity assay of 1 µM enzymes from 30 °C to 60 °C. 35
Figure 2.8. pNPA activity assay of immobilized enzymes at rt and 60 °C. 37
Figure 3.1. SEC of AfFtn-GFP complexes. 43
Figure 3.2. Electrostatic surface maps of designed GFPs. 44
Figure 3.3 SEC of AfFtn and designed GFPs. 45
Figure 3.4. SEC of AfFtn wt in 20 mM phos at pH 5.8. 47
Figure 3.5. SEC of AfFtn-GFPs at pH 5.8. 47
Figure 3.6. AfFtn-GFP(+16)BE precipitation. 48
Figure 3.7. Thermal shift assays of AfFtn-GFPs at pH 7.6. 49
Figure 3.8. Thermal shift assays of AfFtn-GFPs at pH 5.8. 51
Figure A.1. Scheme of antibody/AfFtn/cargo preparation. 63
Figure A.2. GFP-SOD activity. 64
Figure A.3. Scheme of proposed AfFtn capsule and array formation. 66
Figure A.4. AfFtn Y119H Zn2+ binding. 67
Figure A.5. DLS of Y119H assemblies. 67
Figure A.6 Scheme for antigen presentation using AfFtn. 69
Figure A.7 33mer-E65R SEC. 70
Figure A.8. 33mer-E65R 24mer formation. 70
Figure B.1. Probability (p+) of K and R for incorporation at exterior residues 73
Figure B.2. Ramachandran plot showing torsional angles, ϕ and ψ, of all residues in hCAII. 74
Figure B.3. SDS-PAGE analysis of overexpression of hCAII(+23). 74
Figure B.4. SEC analysis of hCAII(+23) mutant. 75
Figure B.5. SDS-PAGE analysis of hCAII(+21) mutant. 75
Figure B.6. CD thermal melts of hCAII 76
Figure B.7. Sequence alignment of hCAII wt and hCAII(+21). 76
Figure B.8. Inhibition of hCAII(+21) by acetazolamide. 77
Figure B.9. SEC analysis of AfFtn-hCAII wt at 0 mM NaCl. 77
Figure B.10. DLS analysis of hCAII(+21) and AfFtn-hCAII(+21). 78

CHAPTER 1: INTRODUCTION

1.1 Protein Cages

Compartmentalization is a fundamental principle in life. Having a mechanism to physically separate spaces allows for simultaneous processes to occur within the same organism to avoid off-target side reactions. These sequestering mechanisms can also help to increase local concentrations of specific molecules to high concentrations to create precise microenvironments. Compartments observed in nature include the lipid bilayer defining and protecting the volume of a cell, organelles such as mitochondria and nuclei, or even smaller specialized containers like carboxysomes or viral capsids.

Protein cages are naturally occurring molecules available to organisms for compartmentalization, and they come in a variety of shapes and sizes (Figure 1.1)[1]. On the large end, carboxysomes range from 90-600 nm and they house ribulose-1,5-bisphosphate carboxylase/oxygenase (RuBisCO) and carbonic anhydrase, and help to concentrate carbon dioxide to overcome the inefficiencies of RuBisCO[2,3]. Vault particles, with still yet to be understood function, form 13 MDa complexes that come together in ~30 nm x ~60 nm barrels[4,5]. Viral capsids protect, transport, and deliver viral genetic material and have a wide variety of sizes from 20-250 nm[6–8]. On the smaller end, ferritin is just 12 nm and plays a major role in iron homeostasis, oxidizing iron from Fe^{2+} to Fe^{3+} to protect cells from radical damage, and storing the iron-oxide mineral within the protein shell[9,10].

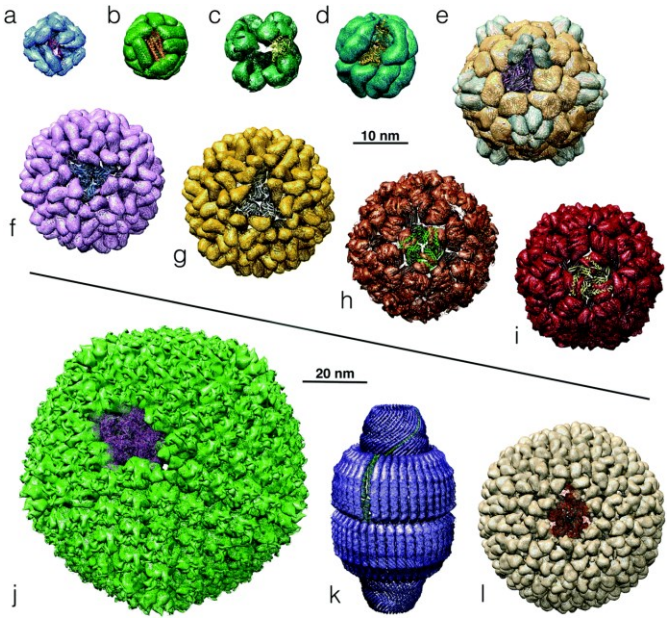

Figure 1.1. Examples of protein cages. Protein cages come in a wide range of shapes and sizes, as pictured above, showing a) small heat-shock protein; b) apoferritin; c) pyruvate dehydrogenase multienzyme complex; d) thermosome; e) cowpea mosaic virus; f) brome mosaic virus; g) cowpea chlorotic mottle virus; h) Qβ bacteriophage; i) bacteriophage MS; j) human adenovirus; k) vault particle; l) bacteriophage P22. Reproduced from Reference 1.

Due to their size, protective abilities, and other advantages, protein cages have long been used for the encapsulation of materials including nucleic acids, nanoparticles and enzymes for use as nanoreactors[7,11,12], drug delivery vehicles[3,7,8,12–18], and in bioimaging[19,20]. Some cages are even repurposed for the loading of non-native cargo. The main methods for cargo-directed loading within these protein capsules rely on electrostatic interactions, affinity methods, or gene fusion[21]. Examples of loading using electrostatics include using nucleic acid tags on enzyme cascades inside cowpea chlorotic mottle virus (CCMV)[22] and highly charged green fluorescent protein variant GFP(+36) inside an engineered lumazine synthase[23]. Affinity-based methods typically rely on insertion of tags and recognition sequences, such as elastin-like polypeptide-CCMV fusions encapsulating cargo with a C-terminal SrtA recognition site[24], a His tag and Ni^{2+}-based assembly system[25], a SpyTag/SpyCatcher two-enzyme indigo biosynthetic pathway within

MS2-based capsid system[26], an α-helical Ca^{2+} pump sequence in hepatitis B viral capsids using partial calmodulin peptides[27], and different anchoring sequences allowing cargo loading into encapsulins[28–31]. In the genetic fusion approach, cargo is directly fused to the monomers or subunits of the target protein cage, such as bacteriophage P22 monomer fusions with alcohol dehydrogenase D[11], CelB glycosidase[32], GFP and mCherry[33], and cytochrome P450[34], among other enzymes, and 13-MDa vault cages fusions with GFP and luciferase[35].

1.2 Ferritin

Ferritin is a family of small protein cages that are found in almost all living organisms outside of a small number of archaeal species[36]. They can be broken down into two major classes, maxi-ferritins with 12-nm outer diameter, and mini-ferritins measuring ~8 nm. While ferritin may have low sequence homology across organisms, the overall 3-dimensional structure is highly conserved. On the smallest level, ferritin monomer is a ~20 kDa four-helix bundle, sometimes with a short fifth E-helix[9] (Figure 1.2 left). Maxi-ferritins are primarily iron-storage proteins that can also oxidize iron from Fe^{2+} to Fe^{3+}. 24 monomers can assemble into 24mer cage-like structures with octahedral (4-3-2) symmetry which have a 12 nm outer diameter and 8 nm inner diameter based on the pH of the surrounding environment (Figure 1.2 right). They are thought to hold ~4500 iron atoms, with some variation between different published studies[9,10,36,37]. Certain maxi-ferritins have di-iron binding ferroxidase centers in the center of the four-helix bundles. Iron enters the cage through the 3-fold symmetrical channel formed at the interface between subunits, eventually makes its way to the ferroxidase center for oxidation, then ultimately migrates to the cavity to form the ferrihydrite core. In certain organisms, like humans, ferritins can form heteropolymers. Human heavy chain ferritin (FTH, 21 kDa) containing the ferroxidase center and light chain ferritin (FTL, 19 kDa) will form statistical mixtures with varying ratios of each ferritin depending on the organ of localization[9]. Mini-ferritins, on the other hand, like DNA binding protein from nutrient starved cells (Dps), form 12mer structures that have an outer diameter of ~9

nm and inner diameter of ~5 nm. In addition to its smaller size, Dps forms cages with tetrahedral (2-3) symmetry, and the primary function is to bind and protect DNA, as its name suggests.

Figure 1.2. Structure of ferritin monomer and 24mer**.** (left) A ferritin monomer, comprising of a four-helix bundle and an optional short fifth E-helix, sometimes containing a ferroxidase site shown by di-iron in blue. (right) A self-assembled 24mer octahedral ferritin. Figure reproduced from reference 37.

Ferritin, as one of the smallest protein cages and one with better biocompatibility than many other cages such as viral capsids, has been used for applications in biochemistry and nanomaterials, including nanoreactors, MRI contrast agents, biosensing, supramolecular scaffolds, and targeted drug delivery. Other metal ions besides Fe^{2+} can enter the ferritin cage via the ion channel, including Mg^{2+}, Zn^{2+}, Ca^{2+}, Cu^{2+}, Pd^{2+}, Au^{3+}, Ag^{2+}, Ir^{3+}, Cd^{2+}, and Se^{2-}, and the ions can be reduced to form metallic nanoparticles[37–44]. While methods exist for the synthesis of nanoparticles and quantum dots in solution, synthesizing particles within ferritin constrains the size of the particle to the volume of the ferritin cavity. Cargo can also be loaded into ferritin using a pH-based disassembly-assembly process where it is brought to very low or very high pH, mixed with the cargo of interest, then brought back to neutral pH and reassembled around the cargo. Encapsulating these particles within ferritin as well as synthesizing them directly in ferritin can increase their solubility, biocompatibility, and help prevent leakage of toxic cations. Encapsulation of nanoparticles, quantum dots, or fluorescent dyes within ferritin have allowed for bioimaging and biosensing[45,46] while also sometimes serving as MRI contrast agents[47]. In materials, ferritin can

be deposited onto surfaces using a layer by layer approach[48,49], or by introducing specific metal binding sites at the 3-fold symmetrical pore for directed assembly of protein arrays[50,51]. FTH has natural affinity for transferrin receptor-1 (TfR1)[52,53] and can also be specifically or non-specifically labeled for use in drug delivery[13–15,20,47]. Recently, the ability to specifically label ferritins or fuse cargo with ferritin while retaining the 24mer structure has led to ferritin being explored as a vaccine presentation platform[54–58].

One ferritin of specific interest to our laboratory is a thermophilic ferritin from the deep-sea thermal vent-dwelling archaeon, *Archaeoglobus fulgidus* (AfFtn). While still a maxi-ferritin, it has a variety of unique features that separate it from most other maxi-ferritins. Despite coming together in the same 12 nm sized 24mer cage, AfFtn exhibits tetrahedral symmetry much like most mini-ferritins (Figure 1.3b). It has four large tetrahedrally-arranged triangular pores that are 4.5 nm from base to vertex. These pores could allow ions to flow in and out of the cavity more easily, although Fe^{2+} is instead observed to enter the cavity through the same 3-fold channels as in most other ferritins and the large pores are only used in iron release[59]. AfFtn is extremely thermostable, with a T_m > 84 °C. It also has unique assembly and disassembly requirements, existing as a dimer under low ionic strength conditions, then assembling into 24mers at high ionic strength at neutral pH[60]. Some advantages of this system are that cargo is not subjected to very low or very high pH conditions to achieve loading, and specific cargo can actually template the formation of 24mers under low ionic strength conditions where AfFtn is normally a dimer. Much of the previous work in our lab has focused on templating AfFtn assembly using gold nanoparticles (AuNPs)[61–65]. We and others have encapsulated a superpositively charged GFP(+36) and GFP(+36)-enzyme fusions[66,67]. Recently, active enzymes without any fusion partners have been encapsulated as well, including lysozyme with a little help from salt[68], and a superpositively charged human carbonic anhydrase II (hCAII(+21))[69], which will be discussed in detail in Chapter 2.

In addition to researchers just using the wild-type ferritin protein, AfFtn has been the subject of various design efforts. In terms of the actual architecture of AfFtn itself versus octahedral ferritins, the hexameric assemblies are joined by 4-fold symmetry elements in octahedral ferritins, while AfFtn hexamers are joined in 2-fold symmetry. It is thought that the specific amino acid residues at the hexamer–hexamer assembly determine whether it will form 4-fold or 2-fold symmetry[60]. It was found that residues in the E-helix of AfFtn played a critical role in stabilizing the tetrahedral assembly, specifically K150 and R151, which establish a positively charged cluster at the 4-fold interface, with the former participating in stabilizing hydrogen bonding. A double alanine mutant of AfFtn K150A R151A (AfFtn-AA) results in the cage reverting to octahedral symmetry while still retaining the unique salt-dependent assembly property at neutral pH, opening the door for a variety of interesting uses[59]. Another work looking at a different interaction, a trimeric interface rich in negatively charged residues, has also been explored. It was hypothesized that electrostatic repulsions between these residues prevented 24mer assembly at low ionic strength, so three mutants were made to investigate this, A127R, D138K, and E65R[65]. E65R ended up being a very interesting mutant, which stays assembled at neutral pH regardless of the ionic strength of the solution. It also reverted to octahedral symmetry (Figure 1.3a) much like AfFtn-AA, providing a second interesting octahedral ferritin based on AfFtn, one with salt-dependent assembly and one without.

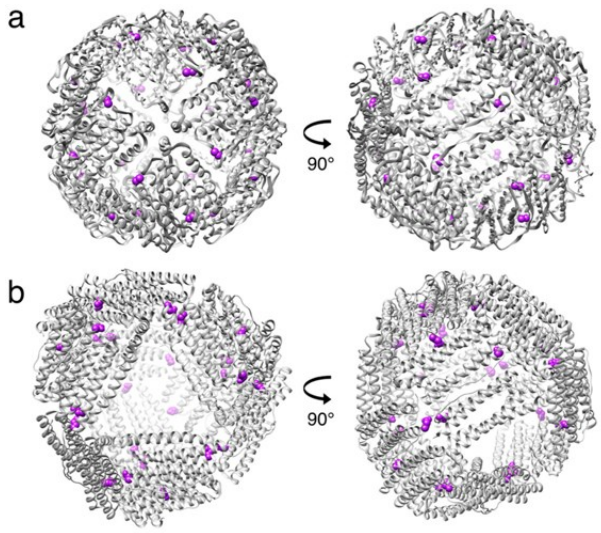

Figure 1.3. Structures of AfFtn E65r and wt. A comparison of the crystal structures of octahedral AfFtn E65R (a) and tetrahedral wt AfFtn with its large triangular pores (b). Residue 65 is shown highlighted in purple. Figure reproduced from reference 65.

One more interesting project in protein design is a humanized version of AfFtn (HuAfFtn). Due to ferritin's nanocapsule size, it can pass through biological barriers much more easily than larger cages or non-protein delivery vehicles and deliver its cargo with enhanced precision compared to freely diffusing therapeutic agents[70]. As a protein from another organism, however, AfFtn does not have specificity for human TfR1 and might also be recognized as a foreign material by the immune system. To overcome these issues, a sequence from FTH was substituted into the B-C loop of AfFtn to mimic the function of the FTH loop[71]. The resulting HuAfFtn retained the salt-dependent assembly property of AfFtn wt while gaining recognition by TfR1, and has been used for HeLa cell uptake[71], delivery of cytochrome *c* to the transfection resistant Acute Promyelocytic Leukemia (APL) NB4 cell line[16], and pre-miRNA to CD71 receptors overexpressed in leukemia cells[72].

1.3 Computational Protein Redesign and Supercharged Proteins

Nature has evolved a vast expanse of proteins with unique folding, structures, and functions. Proteins are defined by the primary sequence of amino acids that make up the polypeptide, but sequences with high homology can end up with very different structures and sequences with low homology can end up folding into highly similar structures. Structure is defined by many competing forces that are highly condition dependent. Computation has made advances in structure prediction using deep learning[73] and improved energy functions[74,75]. DeepMind claims its AI algorithm AlphaFold is able to predict the structure of any protein "with atomic accuracy even in cases in which no similar structure is known"[76,77]. Despite the time and computational power it may take, *de novo* protein design offers some advantages over tweaking existing proteins in that small changes may disrupt overall structure and completely novel functionalities can be created that bear no similarity to existing molecules in nature. Other popular methods of protein design including rationally modifying an existing protein or using directed evolution[78] also require time and effort as well. A number of *de novo* designed proteins have been made, including protein cages[79–82], and have been used for applications in biosensing[83], ligand binding[84,85], ion transport[86], and delivery,[17,87] among others.

Despite the emergence of *de novo* protein design, computational redesign of proteins is still immensely popular, whether it is adding specific sites for bioconjugation, modifying active sites to tune specificity or imbue novel reactivity, or redesigning the entire surface of a protein. This last approach is of special interest to us, as we know that superpositively charged GFP(+36) can get encapsulated by AfFtn. Most proteins in nature have a low overall net charge, with a small subset being naturally supercharged[88]. These naturally occurring supercharged proteins serve critical roles in DNA condensation, fatty acid and protein synthesis, signal transduction, and antibacterial defense.

Several proteins have undergone a surface redesign to have more charged surfaces. Green fluorescent proteins (GFPs) were designed with theoretical surface charges between -30

to +48 (Figure 1.4). The resulting proteins gained thermal stability, increased aggregation resistance, and have even been shown to cross cell membranes[89–91]. Similarly, antibodies against MS2 have been supercharged from +5 to +20, greatly increasing their thermal stability and binding affinity[92]. A handful of supercharged enzymes have been designed as well, as glutathione-S-transferase (GST) has been supercharged[89] to -40 and enteropeptidase[93] to -9, increasing solubility and thermal stability while retaining enzyme activity. Cellulases have been supercharged to a range between -28 and +16[94–96]. Genetically fusing enzymes with supercharged GFPs has been a simple way of gaining the benefits of supercharging without worrying about the unintended effects of changing many residues in a protein. GFP-enzyme fusions have been used for biomimetic packaging, cell delivery, and lipid nanoparticle formation[66,97–99]. However, to date, there are no examples to our knowledge of an engineered superpositively charged enzyme that goes beyond the limits of naturally occurring enzymes prior to the work described in Chapter 2.

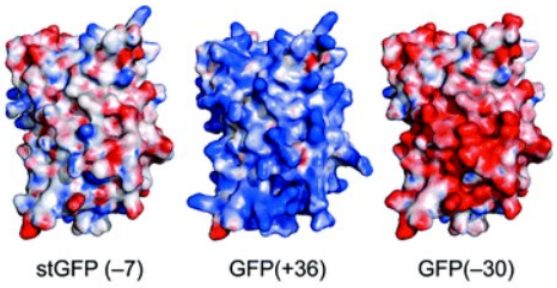

Figure 1.4. Electrostatic maps of GFPs. Superfolder GFP (stGFP) with a theoretical net overall surface charge of -7 has been redesigned through computation to have theoretical surface charges from -30 to +48. Above are electrostatic surface potentials of stGFP, GFP(+36), and GFP(-30) to show the effects of the redesign, with positive charges in blue and negative charges in red. Figure reproduced from reference 89.

1.4 Prospectus

The work described in this dissertation explores the vast potential for AfFtn to be used as a nanocontainer to form stable complexes with supercharged cargo. In Chapter 2, we report a computationally designed superpositively charged surface-redesigned enzyme, human carbonic anhydrase II with a theoretical net overall charge of +21 (hCAII(+21)). This work highlights the benefits of incorporating enzyme cargo within AfFtn. In Chapter 3, we examine the charge magnitude and distribution of GFP required for encapsulation by AfFtn and highlight the role of pH in modulating cargo loading. In the appendices, we explore preliminary data in furthering AfFtn as a platform for drug delivery, protein arrays, and vaccine presentation.

CHAPTER 2: DESIGN OF A SUPERPOSITIVELY CHARGED ENZYME: HUMAN CARBONIC ANHYDRASE II VARIANT WITH FERRITIN ENCAPSULATION AND IMMOBILIZATION

Material in this chapter was originally published in *Biochemistry*. It has been adapted here with permission from the publisher:

Reprinted with permission from Bulos, J. A., Guo, R., Wang, Z., DeLessio, M. A., Saven, J. G., and Dmochowski, I. J. (2021) *Biochemistry* 60, 3596–3609.

2.1 Introduction

Enzymes are increasingly employed in many green chemistry initiatives[78,100–107], particularly for chemical transformations that are difficult to achieve synthetically, often requiring low-yielding steps, expensive metal catalysts, and long workups in organic solvents. Living organisms have evolved systems of enzymes that carry out these reactions under mild aqueous conditions. Enzymes can be modified using directed evolution[78,108,109] or rational design[110–112] to enhance existing activities or gain new biosynthetic capabilities. The applications for engineered enzymes range from pharmaceuticals and organic transformations[113–115] to light harvesting and green feedstock generation[116]. Generally, enzymes are only marginally stable, and perform with optimal activity under very specific conditions. Beyond protein design and directed evolution, the stability and utility of these enzymes, such as increased tolerance to denaturing environments, can be increased through immobilization or encapsulation[117–120]. In employing these strategies, however, a decrement in enzyme activity often results when an enzyme is immobilized or modified[121], so it is useful to develop strategies for maintaining and protecting enzymatic activity.

Most proteins in nature have a low overall net charge, with a small subset being naturally supercharged[88]. These supercharged proteins serve functions in DNA condensation, fatty acid and protein synthesis, signal transduction, and antibacterial defense. While many naturally supercharged proteins are disordered, the small subset of folded supercharged proteins have inspired protein engineering efforts to redesign protein surfaces to display additional charged residues. Green fluorescent proteins (GFPs) were designed with theoretical surface charges ranging from -30 to +48, and these supercharged proteins gained thermal stability and a remarkable resistance to aggregation, as well as the ability to cross cell membranes[89,90]. Similarly, single-chain F_v antibodies against the bacteriophage MS2 have been supercharged from +5 to +20, giving them greatly enhanced thermal stability and binding affinity[92]. Supercharged enzymes have also been designed; glutathione-S-transferase (GST)[89] and enteropeptidase[93] have been supernegatively charged (to -40 and -9, respectively), leading to

increased solubility and thermal stability while still retaining enzymatic activity. Cellulases have been supercharged by multiple groups, ranging from -28 to +16[94,95], but none of the superpositively charged variants had their activity characterized. In other examples, the cellulase charge was engineered between -32.2 and +11.7[96], with the positive charge (+11.7) falling in the range of naturally occurring basic enzymes. More negatively supercharged enzymes may exist due to stabilization from surface-bound cations, and repulsion of anions that disrupt native hydrogen bonds[96,122]. Enzymes have also been genetically fused to supercharged GFPs for uses ranging from biomimetic packaging, cell delivery, and lipid nanoparticle formation[66,97–99]. However, to date, there are no examples to our knowledge of an engineered superpositively charged enzyme that goes beyond the limits of naturally occurring enzymes.

One goal of enzyme engineering is to leverage the unique catalytic capabilities of enzymes in new contexts and applications. For carbon capture and storage (CCS), nature has evolved highly efficient enzymes for the transport and conversion of carbon dioxide. Such enzymes are promising targets for exploring and engineering relevant features for CCS. Current industrial CCS processes include amine scrubbing[123], mineral carbonation into sedimentary basins and reactive rocks[124], capture by microalgae[125], and sequestration via adsorption onto a variety of materials[126–130], which require high pressure, large energy inputs, and/or the identification of specialized storage reservoirs. A potentially milder, more sustainable strategy involves leveraging nature's molecular machinery for carbon fixation, which begins with the chemical transformation of carbon dioxide. Carbonic anhydrases (CAs) are a family of highly efficient enzymes that reversibly hydrate CO_2, generating HCO_3^-.

The well-studied isozyme, the 29 kDa human carbonic anhydrase II (hCAII) operates with near-diffusion-limited rates at ambient carbon dioxide pressures. Its active site contains Zn^{2+} coordinated in a distorted tetrahedral geometry with three histidine residues and a hydroxide ion or water molecule[131]. The enzyme is inexpensive to produce and purify in an active form using heterologous overexpression. In addition to its anhydrase activity, it can also act as an esterase,

allowing for straightforward colorimetric detection of enzymatic activity. While hCAII has very fast kinetics ($k_{cat}^{CO2} \approx 10^6$ s^{-1}, $k_{cat}/K_m^{CO2} \approx 10^8$ M^{-1} s^{-1})[131], it is not well-suited for CCS at elevated temperatures (T > 50 °C). In addition, using hCAII in industrial applications requires enzyme immobilization, as free enzyme cannot be recycled from the reaction[132]. The efficiency of enzymes, including hCAII, is decreased upon immobilization via current methods involving adsorption[133], covalent crosslinking[134], entrapment[135,136] and encapsulation within a supramolecular host[137]. Using other robust proteins to protect or sequester enzymes provides a route to retaining enzyme activity in harsh environments, while facilitating immobilization or recovery of the associated enzymes.

Controlling the molecular features important for enzyme encapsulation and activity can be achieved within nanoscale supramolecular protein hosts. These host proteins range in size from 100-150 nm carboxysomes[3], to 20-250 nm viral capsids[7,8], ~30 nm lumazine synthase[99,138] and ~12 nm ferritin[9,10]. These protein hosts encapsulate a wide variety of cargo, including nucleic acids, nanoparticles and enzymes for use as nanoreactors[7,11,12], drug delivery vehicles[3,7,8,12–18], and bioimaging[19,20]. The three major methods for enzyme loading within these protein capsules rely on electrostatic interactions, affinity methods, or gene fusion[21]. Examples of loading using electrostatics include using nucleic acid tags on enzyme cascades inside cowpea chlorotic mottle virus (CCMV)[22] and highly charged GFP(+36) inside lumazine synthase[23]. Affinity-based methods typically rely on insertion of tags and recognition sequences. One example includes making elastin-like polypeptide-CCMV fusions to encapsulate cargo with a C-terminal SrtA recognition site[24] while another utilizes a His tag and Ni^{2+} to form the assembly[25]. A SpyTag/SpyCatcher system was utilized to incorporate a two-enzyme indigo biosynthetic pathway within MS2-based capsids[26]. An α-helical sequence derived from the membrane plasma Ca^{2+} pump was inserted into the assembly domain of hepatitis B viral capsids to allow for Ca^{2+}-mediated assembly using cargo tagged with the C-terminal domain of calmodulin[27]. The addition of a C-terminal anchoring sequence allows cargo loading into encapsulins[28–31]. Many different cargoes have been investigated from a gene fusion standpoint, in which the cargo is fused

directly to the protein cage monomers or other subunits. Bacteriophage P22 monomers have been fused with alcohol dehydrogenase D[11], CelB glycosidase[32], GFP and mCherry[33], and cytochrome P450[34], among other enzymes, and 13-MDa vault cages have been fused with luciferase and GFP[35]. Issues arise from the need for complicated fusions of enzymes with other proteins or increased steric hindrance within host proteins due to the additional components, so the use of a host-guest system that doesn't require additional proteins or protein domains is appealing.

Recent work from our lab and others has shown that thermophilic ferritin from Archaeoglobus fulgidus (AfFtn) can assemble around a superpositively charged protein, GFP(+36) as well as GFP(+36)-enzyme fusions[66,67], while high ionic strength is normally required for AfFtn assembly in the absence of a templating cargo. The AfFtn 24mer assembly is tetrahedrally symmetrical and has four large 4.5 nm triangular pores, allowing for more facile diffusion of substrate and products into and out of the cage[60]. While self-assembly of AfFtn around GFP(+36)-enzyme fusions has been reported, there are no examples of direct encapsulation of supercharged enzymes, which allows the potential to fit more cargo inside the cage due to the absence of a 30 kDa fusion partner. Furthermore, this provides more opportunity for the enzyme itself to interact directly with the ferritin, instead of this interaction being mediated by the appended supercharged GFP. Previous studies from our laboratory showed that enzyme cargo can be loaded by using maleimide-mediated conjugation of superoxide dismutase to an engineered cysteine on the interior of AfFtn for use in targeted drug delivery[15]. We have also shown simpler methods of loading, as AfFtn can self-assemble around gold nanoparticles with complementary diameter and surface ligands, without requiring additional reagents[61,63,139,140]. One major advantage of encapsulation within AfFtn is that it can confer additional thermal stability to the cargo[66,68]. A general, one-step method for incorporating an enzyme within AfFtn would greatly expand the utility of this approach for enzyme immobilization. With thermally stable CAs from other organisms, encapsulation at room temperature results in only 60% retention of activity[137,141,142]. The highest activity upon encapsulation was a recent report showing 85%

activity with a GFP(+36)-hCAII fusion[66]. Here, we explore the exciting potential to encapsulate hCAII in a stable ferritin protein scaffold, by engineering complementary surface charge interactions to favor encapsulation and robust enzyme activity.

We hypothesized that the surface of hCAII could be redesigned to give the enzyme a high overall net positive charge to promote encapsulation by AfFtn. This task is not straightforward, as many mutants have issues with expression, stability, and activity due to disruption of structure or from alterations to the catalytic mechanism. In a study where libraries of human 3-methyladenine DNA glycosylase (AAG) mutants were tested for viability, it was determined that the overall probability of inactivating AAG with a single random mutation is 34% [143]. Some smaller proteins appear to accept mutations more readily, as a random mutation in T4 lysozyme (164 residues) and barnase (110 residues) led to inactivation at 16% and 5% of sites, respectively[144,145]. Nonetheless, the probability of inactivation of a protein is expected to increase with the increasing numbers of mutations.

An alternative to combinatorial methods is to use computational design to identify the positions on the hCAII surface that can be modified to positive charges. Computational design to modulate protein charge and electrostatic features has been established[92,96,146,147]. Herein, we applied a computational, probability-based design approach to redesign the enzyme[62,148–151]. Candidate exterior residues for mutation were selected by their solvent accessible surface areas (SASA)[152], and those mostly likely to support mutation to K and R were identified and used to guide the choice of mutations. In the resulting designed variant, twenty exterior residues were mutated from either a neutral or negatively charged amino acid to a positively charged amino acid. The putative net charge of each designed variant was quantified by simply neglecting variation of side-chain pK_a with location in the structure and summing amino acid ionization states expected at pH 7. The designed set of mutations increased the expected net charge of hCAII by +22 (in units of the electron charge), from a net charge of -1 for wild-type hCAII to +21 for the mutant. This designed construct hCAII(+21) was experimentally characterized for activity as well

as for encapsulation within AfFtn, and the resulting AfFtn-hCAII(+21) complex was tested for activity at ambient and elevated temperature. Computational design of the superpositively charged enzyme enabled AfFtn encapsulation. Most promisingly, the resulting mutant maintained enzyme activity and gained thermal stability upon encapsulation within the ferritin host. The host-guest complex retained high enzymatic activity at elevated temperatures after immobilization on solid support.

2.2 Materials and Experimental Details

Design of superpositively charged enzyme

To identify the exterior residues of hCAII to target for substitution, the solvent accessible area calculation tool GetArea[152] was applied to two crystal structures of human carbonic anhydrase II (PDB ID: 3KS3 and 3K34)[153] to determine the relative solvent accessible surface areas (SASA) of individual residues. A probabilistic protein design method as described previously[62,65,148,149,154] was applied to the hCAII structure 3KS3. This probability-based design method has been applied previously to design variants of ferritin and ferritin-like proteins[62,65,149]. We note that others have also computationally designed protein charge properties, often by applying a bias toward a particular charge state[92,96,146,147]. The probabilities of a positively charge amino acid (R or K) at each of the 48 residue sites were rank ordered. The top 20 mutations were used to specify hCAII(+23) and, after restoring wild type at D110, the remaining 19 mutations gave the +21 enzyme. The resulting sequence hCAII(+21) contains the following mutations: S152C, S73R, L57R, E187R, Q53R, T37R, L100R, S50K, T177R, S43R, E239R, S220K, Q158R, H36R, N253R, Q136K, S166K, Q74R, E14R, and L240R. For more detailed experimental details performed by Rui Guo, refer to reference 69.

Primers used for mutagenesis of hCAII(+23) to hCAII(+21)

Forward: CCGAGCATACCGTGGATAAGAAAAAATACGCAG

Reverse: CTGCGTATTTTTTCTTATCCACGGTATGCTCGG

AfFtn protein expression and purification

AfFtn wt (UniProtKB O29424) was expressed and purified with slight modifications to previous publications[65]. Briefly, a plasmid containing AfFtn wt was transformed in BL21(DE3) cells (New England Biolabs). Cells were grown overnight at 37 °C in LB broth supplemented with 100 µg/mL ampicillin at 225 rpm. Cultures were transferred to 1 L Terrific Broth and grown at 37 °C supplemented with 100 µg/mL ampicillin at 225 rpm until OD_{600} ~0.8. Expression was induced with 1 mM IPTG for 4 h at 37 °C at 225 rpm. Cells were pelleted by centrifugation (10 min, 6 krpm, 4 °C) and stored at −20 °C. Cells were resuspended in buffer (20 mM sodium phosphate, 20 mM NaCl, pH 7.6) and lysed by treatment with lysozyme (~1 mg/mL final concentration), Benzonase® nuclease (Millipore Sigma) after addition of $MgCl_2$ to a final concentration of 2 mM, and sonication (amplitude of 30, 1 s on, 1 s off, 10 min total processing time). Cellular debris was removed by centrifugation (30 min, 13 krpm, 4 °C) and the soluble fraction was treated with Benzonase® nuclease for 30 min at rt after addition of $MgCl_2$ to a final concentration of 2 mM. The solution was heat shocked for 10 min at 80 °C to precipitate most E. coli proteins and centrifuged (9 krpm, 30 min, 4 °C). The supernatant was passed through a 0.22 µm filter and treated with Benzonase® nuclease for 60 min at rt after addition of $MgCl_2$ to a final concentration of 2 mM (so the AfFtn subunits were still dimers). The protein was concentrated and buffer exchanged (20 mM sodium phosphate, 2.5 M NaCl, 2 mM EDTA, pH 7.6) with Amicon Ultra-15 centrifugal filters (MWCO = 30 kDa) and injected onto a HiLoad 16/60 Superdex 200 size exclusion column (GE Healthcare Life Sciences) equilibrated with high-salt buffer (20 mM sodium phosphate, 800 mM NaCl, pH 7.6). Fractions corresponding to 24mer (~60 mL elution volume) were collected and concentrated with Amicon Ultra-15 centrifugal filters (MWCO = 100 kDa), and were run through the size exclusion column two more times. Protein concentration was determined by the extinction coefficient at 280 nm calculated using ProtParam[155] (1.67 mL mg^{-1} cm^{-1}), and purity was confirmed using SDS-PAGE and A_{280}/A_{260} > 1.7. Expression and purification yielded ~50 mg protein/L of media. Protein solutions were stored at 4 °C until needed for experiments.

hCAII wt protein expression and purification

hCAII wt (UniProtKB P00918) was expressed and purified with slight modifications to our previous publication[156]. Briefly, a plasmid containing hCAII wt was transformed in BL21(DE3) cells. Cells were grown overnight at 37 °C in LB broth supplemented with 100 µg/mL ampicillin at 225 rpm. Cultures were transferred to 1 L LB supplemented with 100 µg/mL ampicillin at 225 rpm and grown at 37 °C until OD_{600} ~0.8. Expression was induced with 1 mM IPTG and 1 mM $ZnSO_4$ (final concentrations) overnight at 18 °C at 225 rpm. Cells were pelleted by centrifugation (10 min, 6 krpm, 4 °C) and stored at −20 °C. Cells were resuspended in phosphate-buffered saline (PBS) and lysed by treatment with lysozyme (~1 mg/mL final concentration), Benzonase® nuclease after addition of $MgCl_2$ to a final concentration of 2 mM, and sonication (amplitude of 20, 1 s on, 2 s off, 10 min total processing time). The lysate was clarified by centrifugation, and the supernatant was loaded onto a 5 mL HisTrap HP nickel immobilized-metal affinity chromatography column (GE Healthcare Life Sciences) in PBS. hCAII was washed with PBS with 20 mM imidazole and eluted with PBS with 500 mM imidazole. Fractions containing hCAII were pooled, concentrated with an Amicon Ultra-15 centrifugal filter (MWCO = 10 kDa), and further purified by size exclusion chromatography using a HiLoad 16/600 Superdex 200 column. Fractions containing hCAII were pooled and concentrated using Amicon Ultra-4 centrifugal filters (MWCO = 10 kDa). Protein concentration was determined by the previously published extinction coefficient[67] at 280 nm (ε_{280} = 57,000 M^{-1} cm^{-1}) and purity was confirmed using SDS-PAGE. A280/260 > 1.7, expression and purification yielded ~25 mg protein/L of media. Protein solutions were stored at 4 °C until needed for experiments.

hCAII(+23/+21) protein expression and purification

hCAII(+23)-His_6 plasmid was purchased from ATUM, based on the computationally designed sequence and expressed based on previously published procedures[67,89], and hCAII(+23)-His_6 plasmid was obtained using PCR site-directed mutagenesis. The hCAII(+23/+21) plasmids were transformed in E. coli BL21(DE3) cells. Cells were grown at 37 °C overnight in LB

broth supplemented with 50 μg/mL kanamycin at 225 rpm, transferred to 1 L LB supplemented with 50 μg/mL kanamycin, and grown at 37 °C at 225 rpm until OD_{600} ~0.8. Expression was induced with 1 mM IPTG and 1 mM $ZnSO_4$ (final concentrations) overnight at 18 °C at 225 rpm. Cells were harvested by centrifugation and stored at −20 °C. Cells were resuspended in lysis buffer (PBS with 2 M NaCl) and lysed by treatment with lysozyme (~1 mg/mL final concentration), Benzonase® nuclease after addition of $MgCl_2$ to a final concentration of 2 mM, and sonication (amplitude of 20, 1 s on, 2 s off, 10 min total processing time). The lysate was clarified by centrifugation (13 krpm for 30 min). Initial purification was performed using HisPur™ Ni-NTA spin columns (Thermo Fisher), washing three times with lysis buffer containing 20 mM imidazole and 10% glycerol, followed by elution with lysis buffer containing 500 mM imidazole and 10% glycerol. Elution fractions were collected and buffer exchanged to PBS with 10% glycerol. Benzonase® nuclease and $MgCl_2$ (2 mM final concentration) were added and the solution was incubated at rt for 60 min to further remove nucleic acids. Using a HiTrap SP HP column (GE Healthcare Life Sciences), cation exchange was performed by running a gradient 0–100% lysis buffer over 25 mL using PBS and lysis buffer. The sample was then concentrated using Amicon Ultra-15 centrifugal filter (MWCO = 10 kDa), and further purified by size exclusion chromatography in PBS using a HiLoad 16/600 Superdex 200 column. Fractions from the peak showing qualitative ability to convert 4-nitrophenyl acetate (pNPA) to 4-nitrophenol (pNP) (yellow color change) were pooled and concentrated using Amicon Ultra-4 centrifugal filters (MWCO = 10 kDa). Purity was verified by SDS-PAGE (Fig. S14) and concentration was determined using the extinction coefficient at 280 nm calculated using ProtParam (ε_{280} = 50,500 M^{-1} cm^{-1}). This process yielded titers around 25 mg of enzyme per L of culture. Protein solutions were stored at 4 °C until needed for further experiments. hCAII(+21) samples from which nucleic acids were rigorously removed during purification gave a ratio of absorbances at 280 nm (A_{280}) and 260 nm (A_{260}) of $A_{280}/A_{260} > 1.7$. Expression and purification yielded ~15 mg protein/L of media.

hCAII(+21) Non-Native Surface Cys152 Dye Labeling

From the purified protein stock, a 500 µL solution of 100 µM hCAII(+21) was prepared with 5 mM TCEP in an opaque Eppendorf tube and incubated for 1 h at 4 °C to ensure that the protein was fully reduced. Following the incubation, freshly dissolved Oregon Green Maleimide (Thermo Fisher) in DMSO was added dropwise to the hCAII(+21) protein incorporating C152. Final concentrations gave dye in 20-fold excess. The reaction proceeded overnight at 4 °C. The reaction was then purified by PD-10 desalting column (GE Healthcare Life Sciences) and the resulting fractions were analyzed by UV-Vis spectroscopy. The dye-labeled protein fractions were pooled and concentrated using Amicon Ultra-0.5 centrifugal filters (MWCO = 10 kDa).

Determination of hCAII(+21) Labeling

The measured A_{280} of dye-labeled hCAII(+21) has contributions from both hCAII(+21) and Oregon Green, while A_{492} is only due to Oregon Green. The concentration of Oregon Green was determined using the manufacturer's extinction coefficient (ε_{492} = 87,000 M^{-1} cm^{-1}). The ratio of A_{280}/A_{492} for Oregon Green Maleimide was experimentally determined to be 0.145. This was used to calculate the A_{280} that can be attributed to hCAII(+21) in the dye-labeled hCAII(+21). The concentration of hCAII(+21) was determined using the extinction coefficient previously described, correcting for the absorbance due to Oregon Green, yielding the labeling percentage or [Oregon Green]/[hCAII(+21)] = 56%.

$$Labeling\ \% = \frac{[Oregon\ Green]}{[hCAII(+21)]} = \frac{\frac{A_{492}}{\varepsilon_{492\ Oregon\ Green}}}{\frac{A_{280} - (A_{492}\ \times\ 0.145)}{\varepsilon_{492\ hCAII(+21)}}} = 56\%$$

AfFtn-hCAII(+21) Complex Formation

AfFtn–hCAII(+21) complexes were formed by mixing hCAII(+21) and AfFtn dimer in a 1:12 or 1:6 ratio in no-salt buffer (20 mM sodium phosphate, pH 7.6) at a concentration of 0.6 µM for native agarose gel electrophoresis, 1.0 µM for pNPA assay and 6.0 µM for size exclusion

chromatography (based on AfFtn 24mer), equilibrating overnight at 4 °C. AfFtn-hCAII(+21) samples used in the Ni-NTA assays, Centricon MWCO assays, and activity assays were isolated 24mer peaks after further SEC purification.

Native Gel Electrophoresis

Native gels (0.7% agarose) were prepared in 5 mM NaCl, 20 mM sodium phosphate, and pH 7.6. Samples were mixed with glycerol (final concentration 16% v/v) immediately prior to running. Gels were run at 100 V for 20 min on ice. Gels were imaged using a Typhoon FLA7000 imager using an excitation wavelength of 472 nm and PMT setting of 500 V. Following fluorescence imaging, gels were stained with Coomassie Brilliant Blue R-250.

Size Exclusion Chromatography

Analytical SEC was performed with an AKTA Pure FPLC system using a Superdex200 Increase 10/300 GL column equilibrated with no-salt buffer (20 mM sodium phosphate, pH 7.6). Samples were prepared as indicated above. Sample (200 µL) was injected and A_{280} and A_{492} were monitored. The sample was eluted at rt using a flow rate of 1.0 mL/min.

Dynamic Light Scattering

Sample (100 µL) was pipetted into a disposable micro cuvette (BrandTech Scientific). DLS was performed on a Malvern ZetaSizer Nano ZS with a scattering angle of 173° at 25 °C (1 min equilibration time).

Fluorescence measurements

Fluorescence analysis of Ni-NTA assay and Centricon MWCO assay samples was performed with a Tecan M1000 microplate reader. Sample (100 µL) was pipetted into a black 96-well plate (Greiner Bio-One). Oregon Green-labeled protein samples were excited at 492 nm and fluorescence was measured at 516 nm.

Ni-NTA Assay

AfFtn-hCAII(+21) samples (100 µL) were prepared as described above and mixed with 100 µL of Ni-NTA resin that had been pre-washed with no-salt buffer (20 mM sodium phosphate, pH 7.6). Samples were incubated for 1 h at 4 °C on an end-over rocker, covered in foil. Post-incubation, samples were centrifuged for 1 min at 13 krpm to pellet the resin. The supernatant was moved to a clean tube for later analysis ("load"). The resin was resuspended in lysis buffer containing 20 mM imidazole, centrifuged, and again the supernatant was removed ("wash 1"). This was repeated twice more ("wash 2," "wash 3"). After washing, the resin was resuspended in lysis buffer containing 500 mM imidazole, centrifuged, and the supernatant was removed ("elution 1"). Again, this was repeated twice more ("elution 2," "elution 3"). The fluorescence of all supernatant samples was measured using a microplate reader as described above.

Centricon MWCO Assay

AfFtn-hCAII(+21) samples (500 µL) were prepared as described above and spun in Amicon Ultra-0.5 centrifugal filter (MWCO = 10 kDa) for 15 min at 13 krpm. The fluorescence of the flowthrough and the retained volume were each measured using the microplate reader.

Determination of hCAII(+21) Loading

AfFtn-hCAII(+21) samples were analyzed by SEC and the A_{280} and A_{492} values were used to calculate the number of hCAII(+21) proteins per AfFtn 24mer. The concentration of AfFtn was calculated using $A_{280,AfFtn}$ and the extinction coefficient above, correcting for the relative absorbance of dye-labeled hCAII(+21) at 280 nm using its absorbance at 492 nm while the concentration of hCAII(+21) was calculated based on A_{492} and dividing by the labeling percentage. The loading, [hCAII(+21)] / [AfFtn 24mer], was then calculated.

$$Loading = \frac{[hCAII(+21)]}{[AfFtn\ 24mer]} = \frac{\frac{A_{492}}{\varepsilon_{492\ Oregon\ Green} \times 56\%\ loading}}{\frac{A_{280} - (A_{492} \times 0.658)}{\varepsilon_{280\ hCAII(+21)}}}$$

pNPA Assay

pNPA assays were performed in a Multizone CARY 3500 UV-Vis spectrometer with slight modifications to published procedures[157]. Samples (270 µL) were prepared at an enzyme concentration of 1 µM. Inhibition assays were performed with 10 µM acetazolamide. Samples were then pipetted into 1 mL quartz cuvettes (Starna Cells, Inc.) and brought to temperature in the UV-Vis instrument as measured by the in-cuvette temperature probes. pNPA (30 µL at 10 mM) was added to the cuvette and the solution was pipetted up and down 7 times to mix (0.9 µM enzyme, 1 mM pNPA). A_{410} was measured every 10 s for 2 min to monitor the evolution of pNP, and the rate was calculated from the linear rate determined between 30 s and 60 s, with one unit being defined as the mg amount of enzyme that releases 1 µmol of pNP per min[132,158].

Enzyme immobilization on agarose resin

hCAII wt, hCAII(+21), and AfFtn-hCAII(+21) were covalently immobilized to 33 mg Pierce NHS-Activated Agarose Spin Columns (Thermo Fisher) according to manufacturer recommendations. Briefly, 400 µL samples of 0.5 or 1.0 µM enzyme/complex in PBS were incubated with dry resin mixing end-over-end for 2 h at rt then overnight at 4 °C. The solution was spun down and coupling efficiency was measured based on the Bio-Rad Protein Assay (Bio-Rad) (hCAII wt and hCAII(+21) >99%, AfFtn-hCAII(+21) 50-80%). The resin was washed at least twice with PBS and remaining resin active sites were blocked by incubating with 400 µL quenching buffer (1 M tris pH 7.4) for 20 minutes at rt with end-over-end mixing. The resin was washed at least thrice with PBS and resin with immobilized enzyme was ready to use in subsequent studies.

pNPA Assay of immobilized enzyme

Immobilized enzyme samples were prepared as described above. PBS (270 µL) was added to each spin column then pNPA (30 µL at 10 mM in ACN) was added and the solution was

pipetted up and down 7 times to mix. Columns were rotated end-over-end at rt or 60 °C for 60 s then the solution was spun through. Flowthrough A_{410} was measured via UV-Vis to monitor the evolution of pNP, then the resin was washed with at least thrice with PBS until one wash after all yellow color was gone. Resin was then used for two more subsequent pNPA assays. All values were corrected against resin-only samples.

CD T_m Determination

10 μM samples of hCAII wt and hCAII(+21) (300 μL) were prepared in no-salt buffer and pipetted into 1 mm quartz cuvettes (Hellma USA). Samples were run in a JASCO J-1500 circular dichroism spectrometer and heated at a rate of 12 °C/h from 10 °C to 90 °C, monitoring θ_{205} (hCAII). The melting temperature, T_m, was determined by finding the temperature at which 50% of starting ellipticity was lost. Thermal melt shown as fraction folded, comparing θ and θ_{max} as described below.

$$Fraction\ Folded = 1 - \frac{\theta_{max} - \theta}{\theta_{max}}$$

2.3 Results and Discussion

Design of superpositively charged enzyme

A high resolution structure of hCAII (PDB ID: 3KS3)[159] was chosen as the template structure for computational design. Exterior residues were identified as those having greater than 40% solvent accessible surface area (SASA),[152] and those whose wild-type identities were G, P, K or R residues not considered for mutation; this yielded a set of 49 exterior residues (and no active site residues) as potential sites for redesign. The design calculations apply a computational method that yields the probabilities of amino acids at variable positions in a given protein structure[62,65,148,149,154]. Computational studies were performed to identify where a C (cysteine) could be introduced to the surface of hCAII as a site for fluorophore attachment. This initial calculation allowed only wild type or C amino acids at each of the selected exterior

residues, and residue 152 was chosen for the mutation S152C as it had the highest C probability. To identify exterior positions suitable for positive charges, calculations were carried out for the remaining 48 exterior residues (152 was kept as C), where the wild-type amino acid, K, R and A were allowed at each variable residue position and all positions were allowed to vary in the calculation. The inclusion of A was used to accommodate mutation from wild type to a smaller amino acid if required to accommodate mutations to K or R elsewhere in the structure. The sum of the probabilities of K and R, $p_+ = p(K) + p(R)$, was used to quantify a site's propensity for presenting a positively charged amino acid. The 48 candidate sites were ranked by their p_+ probability values. The top 20 residues exhibited $p_+ > 0.4$, and if all 20 were mutated they would yield a variant with a +23 overall net charge (Figure B.1). The backbone dihedral angles (ϕ,ψ) were examined using the usual Ramachandran plot (Figure B.2). D110 in the crystallographic structure occupies the left-handed alpha-helical region (near $\phi = \psi = +60°$), which is known from database studies to be mainly populated predominantly by only G, N, and D residues[160]. Residue 110 is within a loop in hCAII, and mutation at this site has the potential to disrupt the stability of the enzyme. Designed variants with (D110K) and without (D110) the mutation and having charges of +23 and +21, respectively, were both advanced for experimental studies. We denote these two constructs by their expected charges: hCAII(+23) and hCAII(+21).

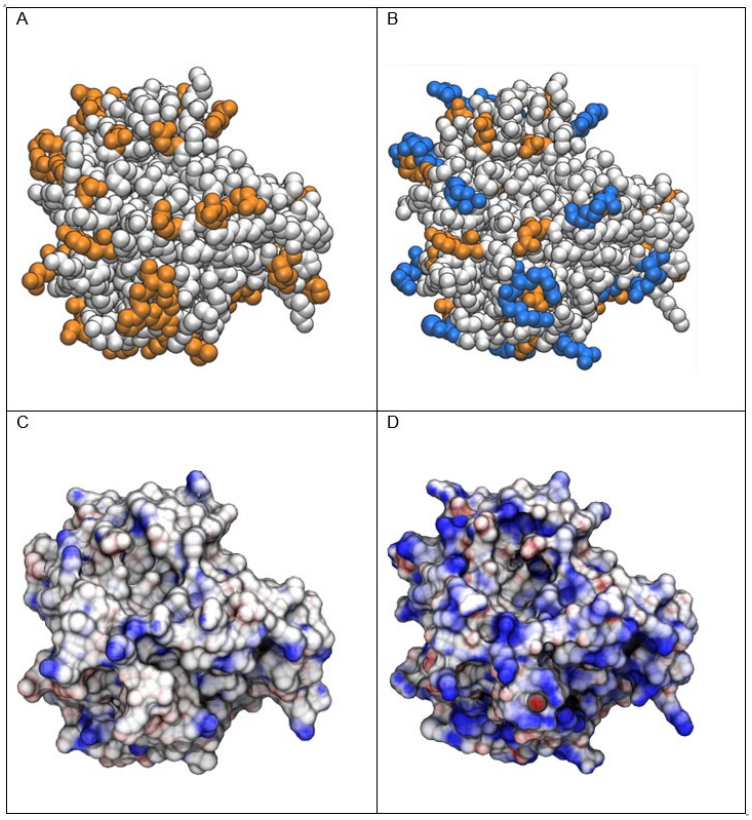

Figure 2.1. Renderings of hCAII and hCAII(+21) (A) Rendering of wild type hCAII. Residues selected for redesign (49 exterior residues) are colored in orange. (B) Rendering of hCAII(+21). Unchanged exterior residues considered for substitution are colored in orange. Twenty mutated residues (including S152C) are colored in blue. (C) Electrostatic surface of wildtype hCAII. (D) Electrostatic surface hCAII(+21). Electrostatic surface renderings are colored to indicate expected charge from negative (red) to positive (blue) and rendered using the APBS plugin[161] of VMD[162].

The plasmid for hCAII(+23) with a C-terminal hexahistidine tag was ordered (Atum Bio), site-directed mutagenesis was performed to make the plasmid for hCAII(+21). Both proteins were expressed in E. coli. A large population of the expressed hCAII(+23) protein ended up forming inclusion bodies (Figure B.3) that did not refold upon snap dilution after pre-extraction with urea and Triton X-100 and solubilization with 8 M guanidine HCl and dithiothreitol (DTT). The small portion of expressed hCAII(+23) that remained soluble purified as inactive, soluble aggregates,

eluting in the void volume of the size exclusion column during size exclusion chromatography (SEC) (Figure B.4). In contrast, hCAII(+21) expressed as a soluble, monomeric, active protein and eluted during SEC with the expected retention time for a 29 kDa protein (Figure B.5). The surface mutations of hCAII(+21) led to a slight loss of thermal stability and reduction in the folding temperature (T_m = 55 °C → 51 °C) relative to wild type as shown by thermal melts monitored by circular dichroism (CD) (Figure B.6). The large number of mutations of like charge may reduce stability and structural integrity of the enzyme to a degree. As a result of these findings, hCAII(+21) was chosen as the supercharged enzyme variant for further study (Figure 2.1, Figure B.7).

We found that the esterase activity of hCAII(+21) is 81% of that of hCAII wt (Figure 2.2), where activity is monitored via the conversion of 4-nitrophenyl acetate (pNPA) to 4-nitrophenol (pNP) at rt,. To confirm that esterase activity is due to hCAII(+21), the pNPA assay was also performed with 10 μM acetazolamide, a widely used non-competitive inhibitor of CAs. The sample with both protein and inhibitor exhibited the same low activity as inhibitor alone, suggesting that turnover occurs at the active site of the enzyme (Figure B.8). No pNP formation was observed in the presence of only AfFtn; this ferritin does not catalyze the hydrolysis.

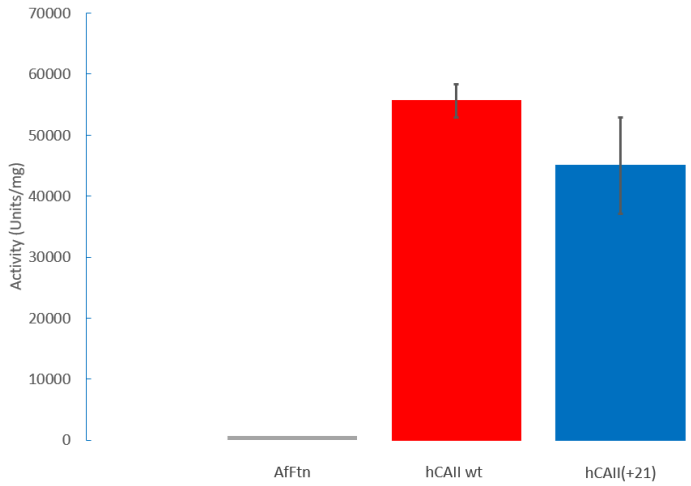

Figure 2.2. pNPA assay of AfFtn, hCAII wt and hCAII(+21). pNPA activity assay of AfFtn, hCAII wt and hCAII(+21) at rt show that expressed hCAII(+21) is an active enzyme that is able to hydrolyze pNPA to pNP at 81% of the rate of hCAII wt, while AfFtn does not hydrolyze pNPA. Error bars indicate the standard error of triplicate measurements.

Superpositively charged enzyme is encapsulated by AfFtn

hCAII (wt or hCAII(+21)) and AfFtn (as dimers of four-helix bundles) were mixed in 1:12 stoichiometry in a low ionic strength buffer ("no-salt" buffer, meaning no added NaCl, 20 mM sodium phosphate, pH 7.6) to maintain AfFtn as dimers prior to mixing. The solutions were assessed by size-exclusion chromatography (SEC). AfFtn and hCAII wt did not interact, as shown by the elution of an AfFtn dimer peak at 17 mL and a free hCAII wt peak at 23 mL (Figure B.9). In contrast, hCAII(+21) induced formation of AfFtn 24mer. We fluorescently labeled hCAII(+21) to monitor the encapsulation. Oregon Green-labeled hCAII(+21) induced AfFtn 24mer assembly and encapsulation, as indicated by an elution peak (both A_{280} and A_{492}) at 13 mL, the normal elution volume of ferritin 24mer on the Superdex200 Increase column. Monitoring A_{280} and A_{492} during SEC of Oregon Green-labeled hCAII(+21)-AfFtn (Figure 2.3), we were able to determine that the average number of hCAII(+21) molecules per AfFtn 24mer was 1.6 ± 0.1,

suggesting a range of 1-to-2 hCAII(+21) molecules encapsulated per AfFtn 24mer. This loading ratio is smaller than prior studies with GFP(+36)-AfFtn (2.5:1)[67] and is also smaller than the ratio observed with most other cargo in much larger protein cages (2-96:1)[12,24,26,30,35,138,163]. The sample homogeneity and nearly 1:1 stoichiometery of hCAII(+21)-AfFtn facilitates biophysical measurements and enzyme studies.

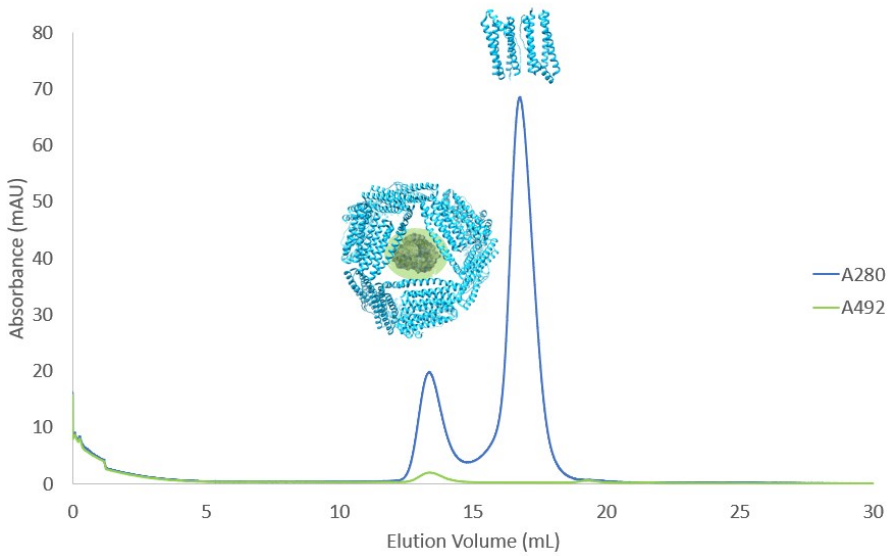

Figure 2.3. SEC of the 1:1 AfFtn-hCAII(+21) complex in no-salt buffer. The peak at 13 mL (A_{280} and A_{492}) corresponds to the formation of AfFtn 24mer. A_{492} peak from the Oregon Green-labeled hCAII(+21) confirms that hCAII(+21) is encapsulated by AfFtn.

The 24mer AfFtn-hCAII(+21) sample was then measured by dynamic light scattering (DLS), yielding an average diameter of 14.5 nm (PDI = 0.06), which is similar to the previously published 13.9 nm diameter for empty AfFtn 24mer[65] in high-salt buffer. This indicated that hCAII(+21) was successfully encapsulated and not simply adsorbed to the surface or contained in non-specific aggregates (Figure B.10).

Samples of Oregon Green-labeled hCAII(+21) and AfFtn were prepared and run on a 0.7% agarose gel under low-salt conditions (5 mM NaCl, 20 mM sodium phosphate, pH 7.6)

(Figure 2.4). Gel fluorescence imaging shows that hCAII(+21) on its own stays in the loading well, which is expected given the polarity of the applied voltage and the large positive charge of the protein. In the presence of AfFtn, hCAII(+21) migrates with the AfFtn 24mer band further down the gel than AfFtn dimer. The Coomassie-stained image of the same gel corroborates these findings, as samples containing both AfFtn and hCAII(+21) migrate furthest towards the positive terminal.

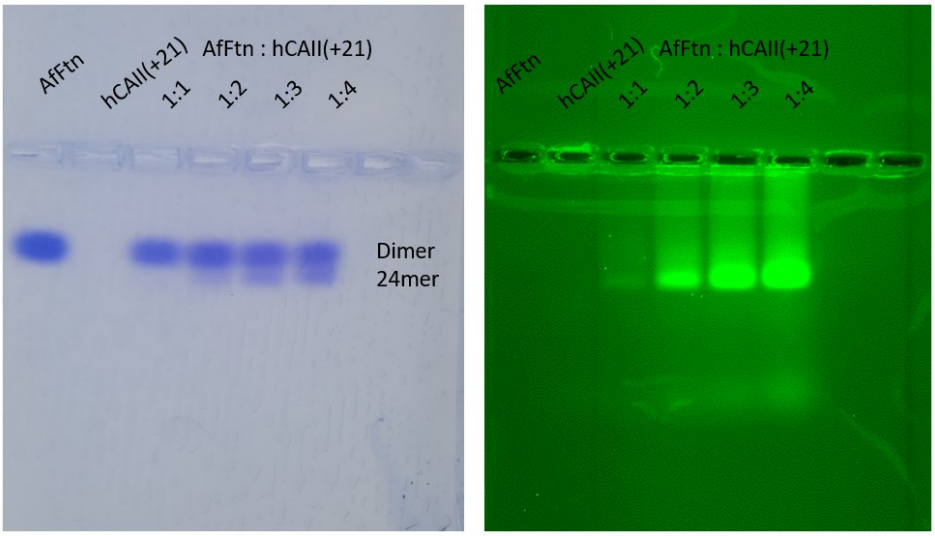

Figure 2.4. Native agarose gel of AfFtn and hCAII(+21). Native agarose gel electrophoresis of AfFtn 24mer:Oregon Green-labeled hCAII(+21), stained with Coomassie blue (left) and fluorescently imaged (right). AfFtn (dimer) alone runs towards the positive terminal and in the presence of excess hCAII(+21) the emergence of a second (24mer) band can be seen. Alone, hCAII(+21) stays in the loading well but in the presence of AfFtn, the complex runs towards the positive terminal.

To further confirm encapsulation of hCAII(+21), we incubated Oregon Green-labeled hCAII(+21) and Oregon Green-labeled hCAII(+21)-AfFtn samples with nickel nitrilotriacetic acid (Ni-NTA) agarose resin (Figure 2.5). Only hCAII(+21) should bind the Ni-NTA resin due to its His_6 tag. When hCAII(+21) was incubated with the resin alone, most of the fluorescence was

seen in fractions after exposure to 500 mM imidazole (elution), confirming that hCAII(+21) binds the resin. For the AfFtn-hCAII(+21) sample, most of the fluorescence was observed in the flowthrough and wash fractions, indicating that hCAII(+21) was encapsulated inside AfFtn, where the His_6 tag interacted minimally with the beads.

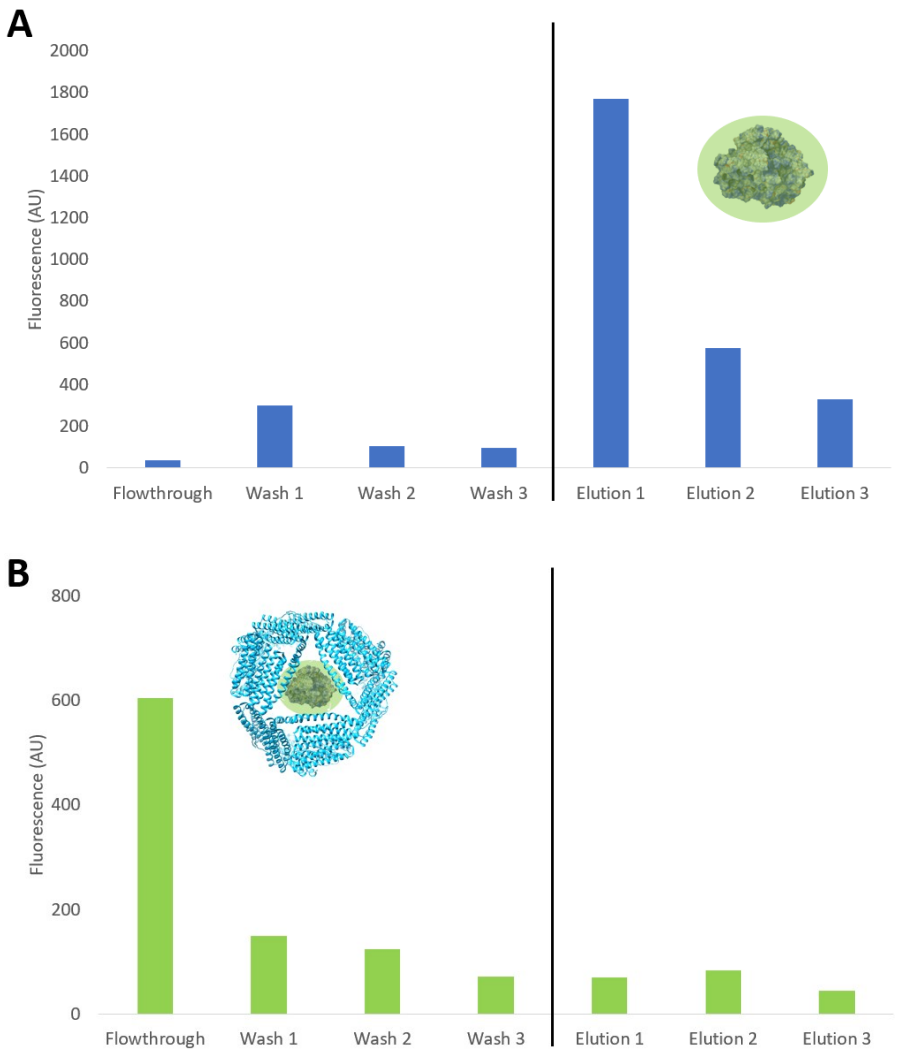

Figure 2.5. Ni-NTA binding assay of hCAII(+21) (A) and the AfFtn-hCAII(+21) complex (B). By itself, hCAII(+21) binds the Ni-NTA resin and very little fluorescence is seen in the load and wash (20 mM imidazole) fractions (A). When eluted with 500 mM imidazole, greater fluorescence is

seen in the elution fractions. For the AfFtn-hCAII(+21) sample (B), most of the fluorescence is seen in the load and wash fractions.

Another method testing encapsulation was a molecular weight cutoff (MWCO) filter-based assay using Centricon tubes (Figure 2.6). Based on the 100 kDa MWCO of the Centricon tube, AfFtn dimer and unencapsulated hCAII(+21) should flow through the membrane after spinning, while the AfFtn-hCAII(+21) sample should be retained. In the hCAII(+21) control, a majority of the fluorescence was indeed seen in the flowthrough, confirming that hCAII(+21) passes through the 100 kDa MWCO filter membrane. The AfFtn-hCAII(+21) sample showed almost all of the fluorescence in the retained volume and comparatively little fluorescence in the flowthrough, further confirming that hCAII(+21) was encapsulated.

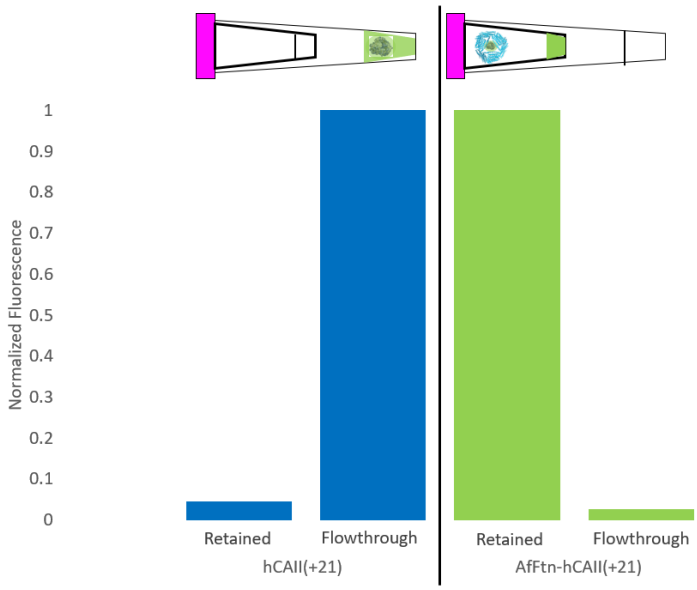

Figure 2.6. Centricon Assay of AfFtn and hCAII(+21). MWCO based Centricon Spin Filtration Assay of hCAII(+21) and the AfFtn-hCAII(+21) complex. Alone, the ~30 kDa hCAII(+21) sample easily passes through the 100 kDa MWCO filter membrane and a majority of the fluorescence is seen in the flowthrough. For the AfFtn-hCAII(+21) sample, the ~500 kDa AfFtn 24mer is too large

to pass through the 100 kDa MWCO filter membrane and most of the fluorescence is seen in the retained volume, agreeing with the results of the Ni-NTA assay.

Superpositively charged enzyme retains high activity within AfFtn

Having established that engineered hCAII(+21) is an active enzyme that can be encapsulated by AfFtn, we tested the enzyme activity of encapsulated hCAII(+21) (Figure 2.7). At 30 °C, hCAII(+21) has 88% of the activity of hCAII wt. More strikingly, upon encapsulation within AfFtn, 97% of hCAII(+21) activity was retained relative to non-encapsulated hCAII(+21). This is the most efficient encapsulated CA system to date, compared with 85% retention of activity after encapsulation of a GFP-enzyme fusion and only 60% retention of activity shown in prior protein host-guest examples[133–135]. Upon increasing the temperature to 40 °C, hCAII wt activity increased by 40% while hCAII(+21) decreased in activity by 32%. AfFtn-encapsulated hCAII(+21) showed 63% enhanced activity at 40 °C relative to free hCAII(+21). At 50 °C and 60 °C both enzymes lost most of their activity.

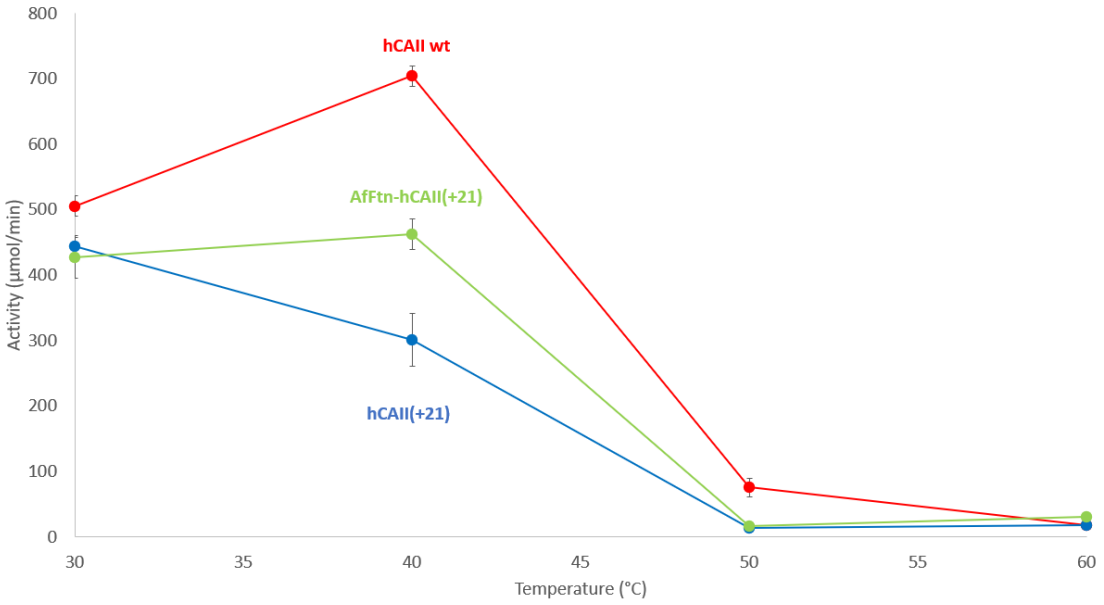

Figure 2.7. pNPA activity assay of 1 µM enzymes from 30 °C to 60 °C. While both hCAII wt and hCAII(+21) experience a large decrement in activity at 50 °C, encapsulating hCAII(+21) within

AfFtn preserves activity at 40 °C. Error bars indicate the standard error of triplicate measurements.

Host-guest complex exhibits high activity at elevated temperatures after immobilization to solid support

One of the biggest challenges in surface enzyme immobilization is the loss of activity that many enzymes experience upon immobilization. NHS-agarose activated resin was selected due to the ease of reacting NHS groups with primary amines on the enzyme surface and the stability and hydrophilicity of the agarose[164]. hCAII wt and hCAII(+21) were loaded with close to 100% efficiency while AfFtn and the AfFtn-hCAII(+21) complex were loaded with 50-80% efficiency. Although the activity of the enzymes decreased upon immobilization at rt, they remained highly active towards pNPA, while AfFtn showed no activity (Figure 2.8). Immobilization to the resin provided considerable thermal stability to both hCAII wt and hCAII(+21), which had comparable activity at 60 °C vs rt. Activity of the AfFtn-hCAII(+21) complex nearly tripled at the elevated temperature. One possible explanation for this phenomenon is that the AfFtn adopts a more compact structure upon immobilization and forms more contacts with hCAII(+21), similar to how enzymes loaded into size-matched metal-organic frameworks (MOFs) exhibit enhanced stability and activity[118,165]. Enzyme immobilization often results in an expansion of the temperatures where the enzyme is active and can also shift the maximum activity towards higher temperatures[133,135,166–168]. Importantly, the ferritin-encapsulated and immobilized enzyme is also reusable, retaining activity after multiple runs. This demonstrates the versatility of immobilizing enzyme-loaded AfFtn and could be generalizable to other types of solid supports.

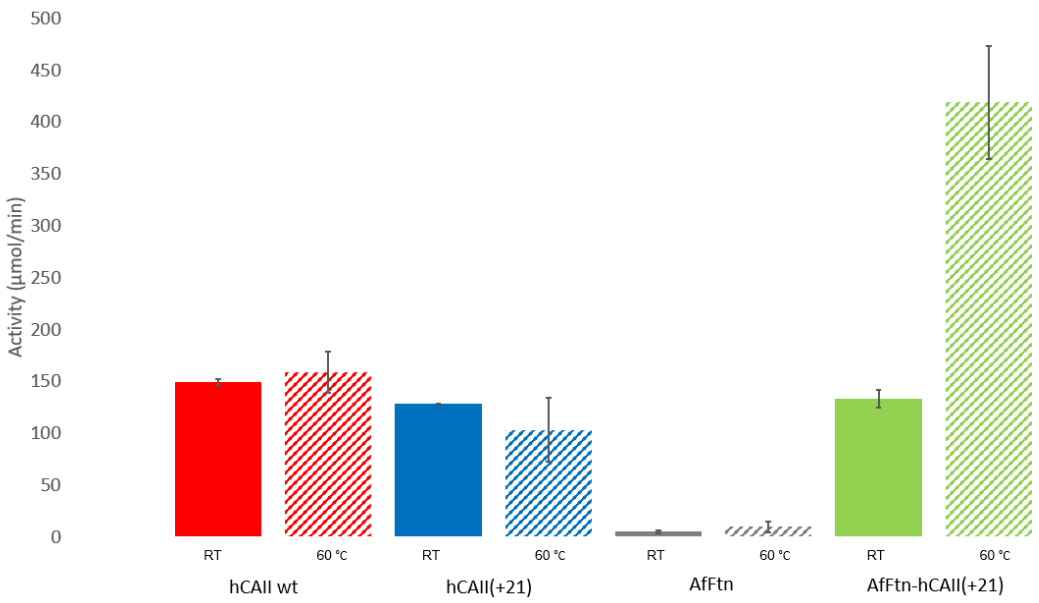

Figure 2.8. pNPA activity assay of immobilized enzymes at rt and 60 °C. Immobilized enzymes lose activity upon immobilization relative to free enzyme in solution, but activity is little affected when raising the reaction temperature to 60 °C except for the AfFtn-hCAII(+21) complex, which experiences a threefold increase. Immobilized AfFtn shows negligible activity at both temperatures. Error bars indicate the standard error of triplicate measurements, in which enzymes were reused for subsequent runs.

2.4 Conclusions

In conclusion, we have engineered the surface of hCAII to display a theoretical overall charge of +21 to give it the ability to template the formation of AfFtn 24mers around it while maintaining enzyme activity. Methods of characterizing hCAII(+21) by SEC, DLS, SDS-PAGE, CD thermal melts and esterase assays confirm the identity and activity of the enzyme. SEC, Ni-NTA and Centricon MWCO assays, and native agarose gels verify that hCAII(+21) is encapsulated within AfFtn cages. hCAII(+21) retains high activity even upon encapsulation and immobilization and gains thermal stability within the AfFtn cavity, especially after immobilization.

We provide the first example of a designed superpositively charged enzyme, which is able to induce AfFtn 24mer assembly without the need for salt or a superpositively charged fusion partner. This provides a general strategy for redesigning the surface of an enzyme for encapsulation within the thermally stable AfFtn protein host. Having immobilized a superpositively charged enzyme within AfFtn and the resulting host-guest complex on solid support and observing both the retention of high enzymatic activity and thermal stabilizing effects, AfFtn emerges as an even more intriguing protein host. Strategies for maximizing enzyme activity in scenarios relevant to carbon dioxide sequestration still remain to be explored. Additionally, due to sample homogeneity and the low guest:host ratio, these complexes are attractive candidates for further characterization, e.g., to elucidate the charge complementarity at the AfFtn-enzyme interface, its role in 24mer assembly, and effects associated with immobilization. Overall, this approach can be employed with a variety of other enzymes that could benefit from the protection of a thermophilic protein cage for applications in green chemistry and therapeutic enzyme delivery.

2.5 Accession Numbers

Sequences for hCAII(+23) (GenBank Accession No. MW770314) and hCAII(+21) (GenBank Accession No. MW770315) have been deposited in the GenBank Data Libraries.

2.6 Funding Sources

Funding for this work was provided by the NSF (CHE-1905203) to I.J.D. and J.G.S., the Vagelos Institute for Energy Science and Technology (graduate fellowship) to J.A.B., and the LRSM MRSEC IRG-3 (NSF DMR-1720530) to I.J.D. Protein modeling and design employed the Extreme Science and Engineering Discovery Environment (XSEDE), which is supported by NSF grant no. ACI-1053575, under grant no. TG-CHE110041.

CHAPTER 3: EXPLORING GFP CHARGE MAGNITUDE AND DISTRIBUTION REQUIREMENTS FOR THERMOPHILIC FERRITIN ASSEMBLY

3.1 Introduction

Compartmentalization is a fundamental principle in life. The separation of membrane-bound organelles from the rest of the cytoplasm allowed for some of the most monumental changes that gave rise to living organisms. Protein cages are naturally occurring spaces for organisms to conduct isolated chemical reactions. These cages range in size from ~ 9 nm spherical DNA-binding protein from starved cells (Dps) on the small end[9] to 70 nm × 40 nm × 40 nm barrel-shaped vault nanoparticles on the large end[35]. Three commonly used naturally occurring cages are MS2 capsids (27 nm)[26], lumazine synthase (16 nm with the ability to switch to 29 nm architecture under the right conditions)[138,169] and ferritin (12 nm)[63]. Other cages have been designed based on these scaffolds and tuned in order to hold specific cargoes or to better serve specialized applications[17,51,80,170,171].

Ferritin is a 20 kDa four-helix bundle iron-storage protein that exists as a 24mer cage-like structure under physiological conditions with an internal diameter of 8 nm and an external diameter of 12 nm[9,10]. Ferritins have long been used for a wide range of applications, including catalysis[172,173], biosensing[45,47], nanoelectronics[10,174], and drug delivery[14,15,20,47] due to their small size and biocompatibility. Traditional methods for loading non-iron cargo into ferritin either involves ion diffusion into the cage and reduction to form a nanoparticle[175] or a disassembly-reassembly procedure in which the ferritin is disassembled at very low pH, the cargo is added to the ferritin, and encapsulation by the ferritin is achieved upon returning to neutral pH[176].

We and others have reported a facile cargo-directed self-assembly method of loading, taking advantage of the unique salt-dependent assembly of *Archaeoglobus fulgidus* ferritin (AfFtn) at neutral pH[66–69]. AfFtn has a highly electronegative interior surface, and salt and/or superpositively charged cargo can help screen unfavorable charge repulsions between AfFtn dimers so they can assemble into 24mers. Current protein cargo that can be loaded under low ionic strength conditions include the superpositively charged green fluorescent protein, GFP(+36), GFP(+36)-protein fusions, and an engineered supercharged human carbonic anhydrase II (hCAII(+21)).

It is currently unknown how much charge is actually needed to form these cages and whether the positioning of these charges affects assembly. The starting point for GFP(+36) was superfolder GFP (stGFP), and it was redesigned to have a net overall surface charge of +36 with the charge evenly distributed around the entire surface of the GFP[89,97]. The total charge, +36, is much higher than most naturally occurring charged proteins in nature[88], and it is likely that charges lower than +36 should be able to template assembly of ferritin as well. GFP is a ~3 nm β-barrel structure, which occupies < 10% of the 8 nm spherical cavity volume. Based on its smaller size, GFP is unable to interact with all 24 ferritin subunits simultaneously, leading to questions about the charge distribution requirements for assembly and encapsulation. Furthermore, all previous work with electrostatic loading has explored a narrow pH range, pH = 7.0-7.6. Lowering the pH of the buffer could decrease the electrostatic repulsion between ferritin dimers, potentially leading to more facile cage formation. Similar observations have been made in *E. coli* ferritin, where pH can affect assembly rate at low ionic strength[177].

Fluorescence anisotropy is a popular tool for studying biomolecular interactions in solution[178–182]. The polarization of a fluorophore is inversely related to its tumbling time and light emitted by a slow-tumbling fluorophore can have different intensities in different polarization planes. A small, freely diffusing fluorophore will typically tumble rapidly in solution and emit largely unpolarized light. When a fluorescent protein or a fluorescently labeled protein binds a target, the tumbling typically slows down as a result of the increase in hydrodynamic radius and it emits polarized light in the plane of excitation. Performing time-resolved fluorescence anisotropy is an especially robust way of measuring local viscosity or observing homo-Förster Resonance Energy Transfer (FRET) between fluorescent proteins that are in close contact. To date, no one has reported on how supercharged GFPs are arranged in ferritin cages. Using anisotropy measurements, we aim to shed light on this process.

In this work, we investigate the charge magnitude and distribution requirements for GFP to template assembly of AfFtn and we also seek to understand the loading behavior of the cargo.

We investigate the loading of GFP(+36), GFP(+28), GFP(+14), and GFP(+9) in order to elucidate how much charge is required. To learn about the effect of the charge localization, we look at three different Janus-faced GFPs that were designed using a probabilistic protein design method[69,183,184] in collaboration with the Saven laboratory. These are GFP(+16)bottom which has all of the charge on what we arbitrarily define as bottom of the barrel (the with both the N and C termini), GFP(+16)side which has all of the charge on one face of the barrel, and GFP(+16)BE (both ends) which has all of the charge on the top and the bottom of the barrel. Furthermore, we explore the effect of pH on the ability to load cargo within AfFtn and how it affects the loading number.

We were able to draw several conclusions from these studies. We found that +28 charge is sufficient to promote cargo encapsulation at pH 7.6, and by lowering the pH to 5.8 even GFP(+9) can promote loading into ferritin. This opens the possibility of loading native proteins that contain basic surface residues and overall charge of at least +9. The two single-sided Janus-faced GFPs did not induce assembly at pH 7.6, but the dual-sided GFP(+16)BE did to a small extent, indicating that a bilobally charged protein may be more effective at templating assembly. Nevertheless, the magnitude of the theoretical total surface charge appears to be a more reliable predictor of which protein cargo will get encapsulated.

3.2 Results and Discussion

AfFtn and GFP(+36), GFP(+28), GFP(+14), and GFP(+9) were mixed at a ratio of 1:1 in 20 mM phosphate buffer, pH 7.6 and loaded onto a size exclusion column (Figure 3.1). GFP(+36) and GFP(+28) both induced assembly of the AfFtn 24mer, but when mixed with GFP(+14) or GFP(+9) the AfFtn remained as dimer at pH 7.6. Based on comparing the A280 and A488 values of the size exclusion chromatography (SEC) trace, GFP(+36) and GFP(+28) load at similar levels, 3 GFPs per AfFtn cage.

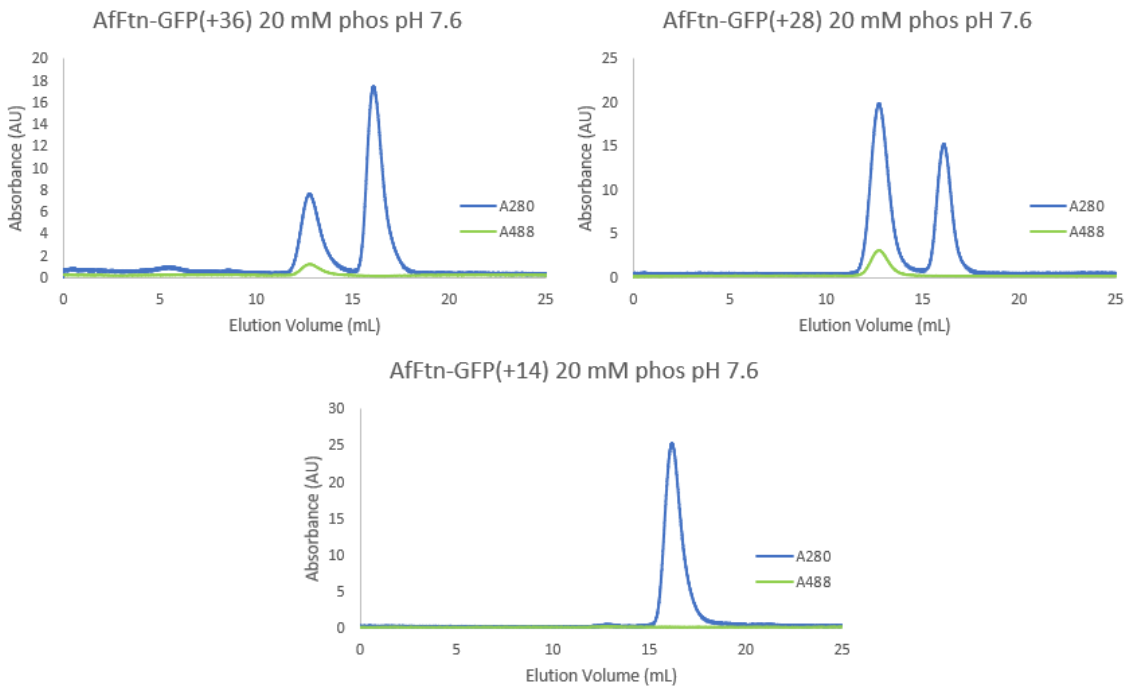

Figure 3.1. SEC of AfFtn-GFP complexes. SEC of AfFtn-GFP(+36) (left), AfFtn-GFP(+28) (middle), and AfFtn-GFP(+14) (right) show that GFP(+36) and GFP(+28) both template 24mer formation, whereas GFP(+14) mixed with AfFtn dimers results in no 24mer assembly at pH 7.6. A280 in blue is a measure of all proteins in the trace, whereas A488 is a measurement solely corresponding to the GFP chromophore.

GFP, approximated as a cylinder of 3 nm diameter x 4 nm height, is theoretically too small to interact directly with all 24 subunits of AfFtn at the same time. This motivated the design of three GFP(+16) variants that maximize the charge in different regions of the GFP beta-barrel. The resulting GFP(+16) variants were GFP(+16)bottom, in which all added positive charges were localized to the bottom of the barrel (where the N and C termini are located), GFP(+16)side where charges were only added to half (a 180° arc) of the barrel, and GFP(+16)BE where charges were added to the top and bottom surfaces of the GFP barrel (Figure 3.2).

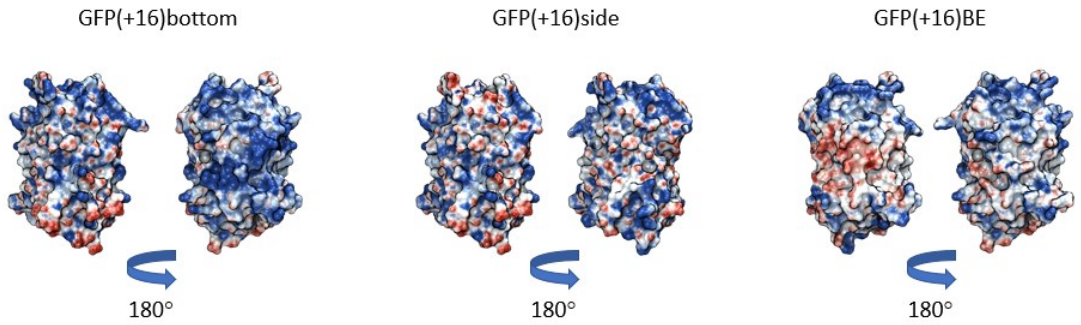

Figure 3.2. Electrostatic surface maps of designed GFPs. GFP(+16)bottom (left) has all of the additional positive charges added to the bottom of the barrel, GFP(+16)side (middle) has all of the additional positive charges added to only one 180° face of the barrel, and GFP(+16)BE (right) has additional positive charges added at both ends (top and bottom faces of the barrel). An electrostatic surface potential map is shown, with positive charges in blue and negative charges in red.

Again mixing at a ratio of 1:1 in 20 mM phosphate buffer, pH 7.6 and running the resulting samples on SEC, it was found that GFP(+16)bottom and GFP(+16)side yielded similar results to GFP(+14) and GFP(+9), with no evidence of 24mer formation (Figure 3.3). However, incubation with GFP(+16)BE promoted formation of some 24mer ferritin, with loading of ~2.5 GFPs per AfFtn. This result suggests that GFP might bridge multiple clusters of AfFtn dimers along their E-helices, helping to stabilize the cage.

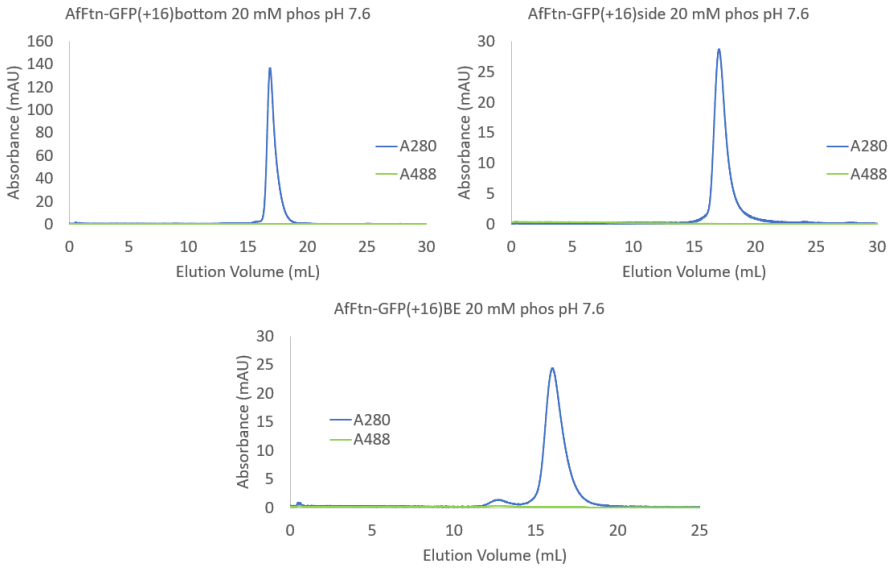

Figure 3.3 SEC of AfFtn and designed GFPs. SEC of AfFtn-GFP(+16)bottom (top left) and AfFtn-GFP(+16)side (top right) show that the Janus-faced GFPs do not induce assembly of AfFtn dimers at pH 7.6. SEC of AfFtn-GFP(+16)BE (bottom) shows that a small amount of 24mer is formed with the bilobal GFP.

To determine how the actual charge of the GFPs in solution differs from the theoretical charge under different conditions, zeta potential was measured for each of the superpositively charged GFPs (Table 3.1). The GFPs followed the general trend of the overall theoretical charge, but the Janus-faced GFPs all had lower zeta potentials than their GFP(+14) counterpart that had evenly distributed charge. Zeta potential measures the electrical potential of the slipping plane of the protein and is not a direct measurement of the protein itself. Many factors, including the pH, buffer composition, co-solutes, or even choice of buffer salt can influence the measurements. As a result, we chose to measure zeta potential with 20 mM HEPES at pH 7.5 due to the wider separation of zeta potentials achieved relative to other conditions tested.

sample	average	stdev
GFP(+36)	19.7	2.8
GFP(+28)	13.5	4.5
GFP(+14)	10.7	0.5
GFP(+9)	-1.7	0.2
GFP(+16)bottom	0.9	0.3
GFP(+16)side	6.7	1.2
GFP(+16)BE	6.6	0.5

Table 3.1. Zeta potential of GFPs measured in 50 mM HEPES, pH 7.5.

As electrostatic repulsion between subunits is an obstacle to overcome in AfFtn 24mer formation, we next lowered the pH of the buffer from 7.6 to 5.8 to reduce the overall negative charge on the ferritin. By doing so, we found that a small amount of AfFtn (~20%) remained assembled even at 0 mM NaCl (Figure 3.4). Upon mixing the GFP variants with AfFtn, we found that each positively charged GFP was able to get encapsulated within AfFtn, while eGFP (with a theoretical net overall charge of -7 at pH 7.6) was excluded (Figure 3.5). We propose that this is due to decreasing electrostatic repulsions between AfFtn subunits rather than increasing the overall net charge of the GFPs by lowering the pH, since some of the AfFtn remained assembled even under no salt conditions. At pH 5.8, mixing AfFtn and GFP(+16)BE resulted in significant precipitation at a range of mixing stoichiometries (Figure 3.6). In the process of testing each GFP variant's ability to be encapsulated within AfFtn, we found that GFP(+36) seemingly formed a 1:1 complex based on the stoichiometry of the A280 and A488 when mixed at a 1:1 ratio. Upon varying the stoichiometry of mixing GFP(+36) and AfFtn, we found we could get a range of loadings, from 1:1, 2:1, 2.5:1, and 3:1, with loading seeming to plateau around ~3.5:1 (Table 3.2).

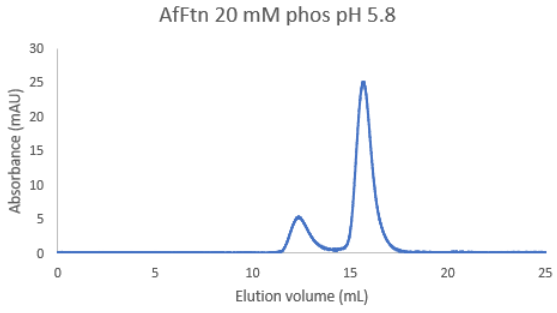

Figure 3.4. SEC of AfFtn wt in 20 mM phos at pH 5.8. AfFtn still remains ~20% assembled despite the absence of NaCl.

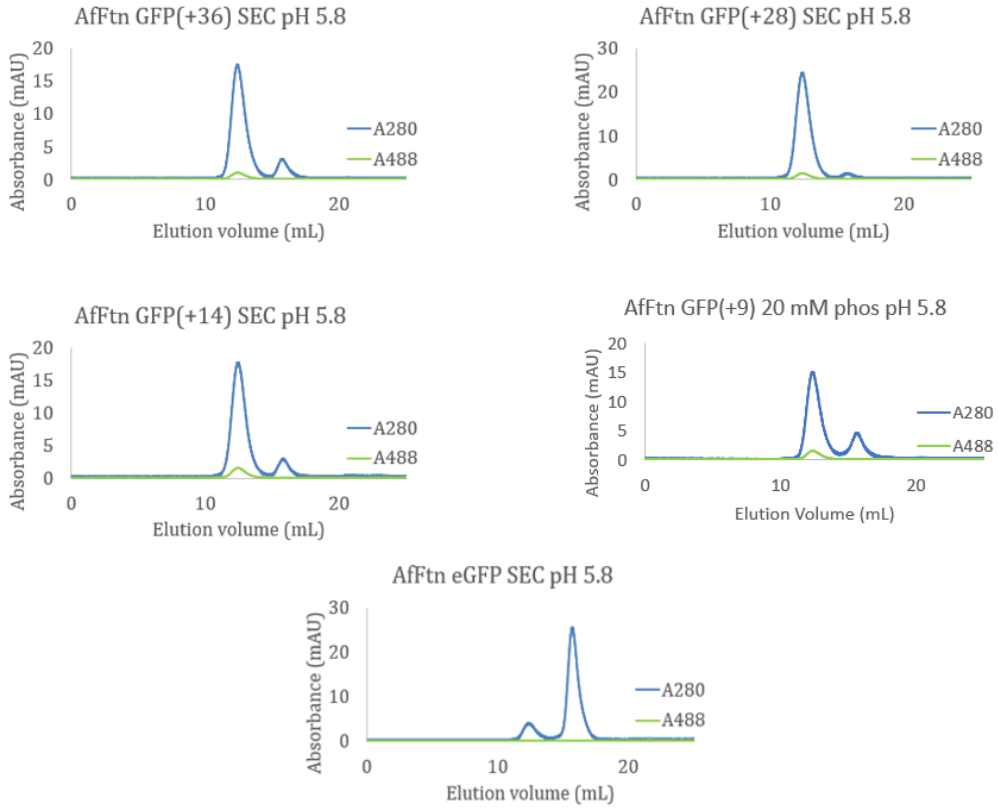

Figure 3.5. SEC of AfFtn-GFPs at pH 5.8. SEC of AfFtn-GFP(+36) (top left), AfFtn-GFP(+28) (top right), AfFtn-GFP(+14) (middle left), and AfFtn-GFP(+9) (middle right) show that all of the superpositively charged GFPs template 24mer formation, while eGFP (bottom) cannot.

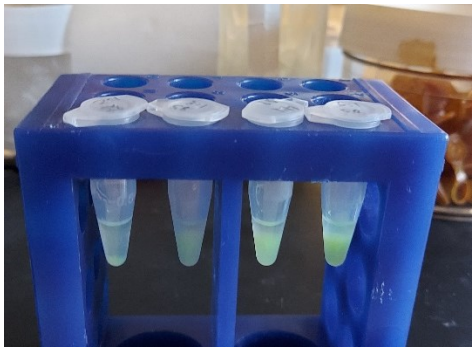

Figure 3.6. AfFtn-GFP(+16)BE precipitation. Mixing AfFtn and GFP(+16)BE (1:1, 1:2, 1:3, 1:4) at pH 5.8 led to significant precipitation.

mixing stoichiometry	loading
1:1	1
1:2	2
1:3	2.6
1:4	3.2
1:5	3.3
1:6	3.3
1:7	3.4
1:8	3.3

Table 3.2. Loading number based on starting mixing stoichiometry of AfFtn:GFP(+36) as determined by SEC. A 1:1 mixing ratio leads to single encapsulation, while 1:2 loading achieves a 1:2 ratio and 1:3 achieves a ratio of 2.6. Starting with a higher mixing stoichiometry sees diminishing returns, seeming to plateau around 3.4.

To determine the stability conferred by encapsulation within AfFtn, we performed a differential scanning fluorimetry-based assay using the fluorescence of the GFP chromophore. Despite stGFP's naturally high T_m, at pH 7.6, all of the GFPs that were encapsulated gained thermal stability. GFP(+36) gained the most thermal stability (85 °C → 90 °C), followed by GFP(+28) (83.2 °C → 86.2 °C), with the least charged GFP(+16)BE gaining the most modest benefit (84.5 °C → 86.5 °C) (Figure 3.7, Table 3.3). Surprisingly, at pH 5.8, all of the GFPs decreased in T_m, with GFP(+36) and GFP(+16)BE experiencing the smallest decrease (Figure 3.8, Table 3.3).

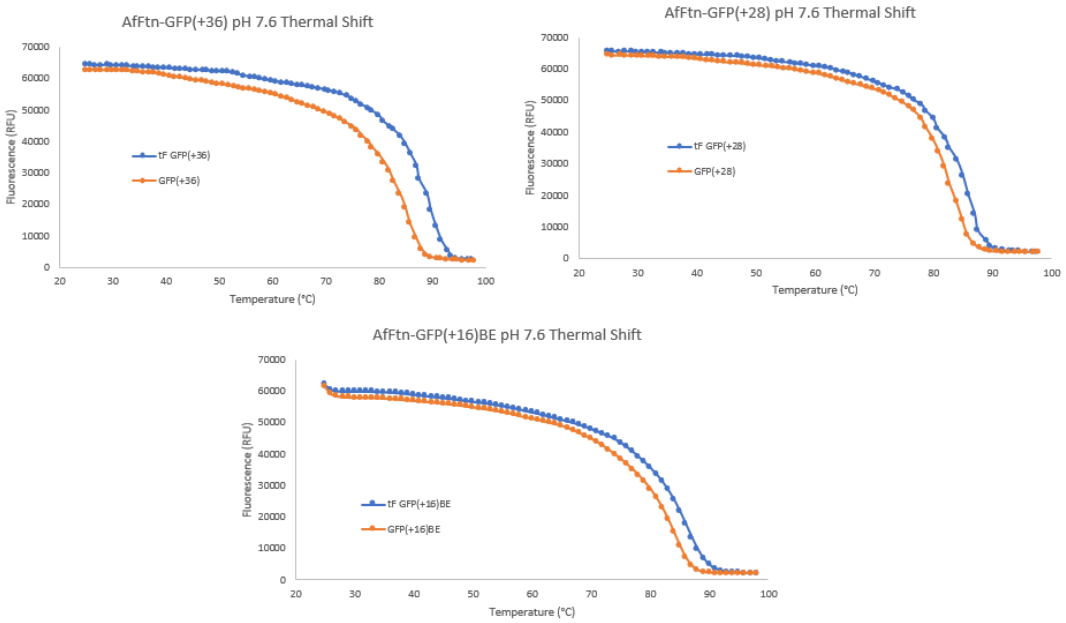

Figure 3.7. Thermal shift assays of AfFtn-GFPs at pH 7.6. Thermal shift assay of AfFtn-GFP(+36), AfFtn-GFP(+28), and AfFtn-GFP(+16)BE based on differential scanning fluorimetry of the GFP chromophore at pH 7.6. GFP(+36) gained the most thermal stability (+5 °C), GFP(+28) gained 3 °C, while GFP(+16)BE gained the most modest benefit (+2 °C). T_m was determined where -R'(T) was at a maximum. All measurements were performed in triplicate.

	pH 7.6	
sample	-AfFtn	+AfFtn
GFP(+36)	85	90
GFP(+28)	83.2	86.2
GFP(+16)BE	84.5	86.5

	pH 5.8	
sample	-AfFtn	+AfFtn
GFP(+36)	84	83
GFP(+28)	83.2	80
GFP(+14)	81.4	77.1
GFP(+16)side	81.5	78.3
GFP(+16)bottom	81.1	79.1
GFP(+16)BE	84.5	83.5

Table 3.3. Thermal shift assay results of all the AfFtn-GFP combinations at both pH 7.6 and pH 5.8 where applicable. T_m was determined where -R'(T) was at a maximum. All measurements were performed in triplicate.

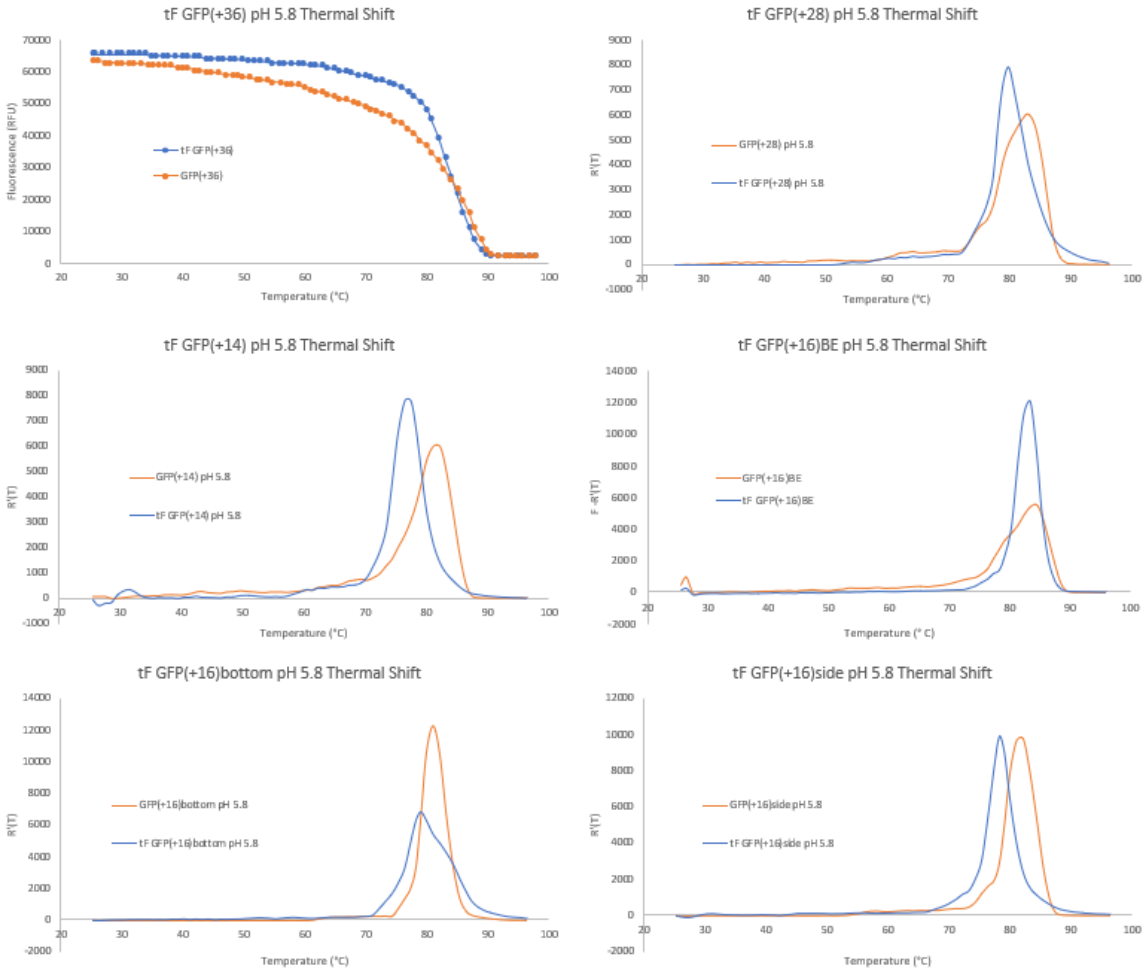

Figure 3.8. Thermal shift assays of AfFtn-GFPs at pH 5.8. Thermal shift assay of AfFtn-GFP(+36), AfFtn-GFP(+28), and AfFtn-GFP(+16)BE based on differential scanning fluorimetry of the GFP chromophore at pH 5.8. T_m was determined where -R'(T) was at a maximum. -R'(T) was calculated for AfFtn-GFP(+36) based on raw fluorescence data whereas a direct readout of -R'(T) was collected for all other samples. All measurements were performed in triplicate.

As an additional measure of cage stability, we want to measure how well the cargo is retained after extended storage time of the AfFtn-GFP(+36) complex. By running freshly prepared samples and comparing them to samples that have been stored at 4 °C, we can see how much of the GFP is released from the cage following prolonged incubations. The AfFtn-GFP, which has

been observed to be very stable, will likely retain most or all of the cargo. The stability of the complex is important to know for applications where it needs to stay assembled for extended lengths, from nanomaterials to formulated drug products.

As informative as a crystal structure of the AfFtn-GFP complex would be, it has been equally difficult to get full crystallographic data for the complex. Many initial attempts to crystallize the complex resulted in non-fluorescent crystals with no observable protein density within the cage. Moving to pH 5.8 and using the 1:1 AfFtn-GFP(+36) complex resulted in green fluorescent crystals, but resolving electron density within the cage has still proven difficult. In order to get a better understanding of the interactions between AfFtn and its supercharged cargo, we turned to fluorescence anisotropy. Using this technique, we hoped to see if GFP interacting with the cage results in an observable increase in anisotropy versus tumbling free in solution, as the complex increases in mass ~17-fold. Surprisingly, the anisotropy for GFP(+36) decreases upon encapsulation, from 283 to 131, a similar trend seen for other GFPs. One plausible explanation for this is rather than slowing down tumbling due to interactions with the AfFtn cage, the GFP is partially desolvated[185,186]. We then turned to time-resolved anisotropy to see if we could distinguish between single GFP loading versus loading multiple GFPs per cage. Only when multiple GFPs inhabit the same AfFtn cage are they in range to undergo homo-FRET. In the cases of multiply loaded AfFtns, we have preliminarily observed homo-FRET. When using the 1:1-loaded AfFtn-GFP(+36) complex at pH 5.8, we hope observe whether or not we indeed have single GFP loading within the AfFtn cage, rather than multiple GFPs occupying the same cage and ending up with a mix of loaded cages and empty cages. To get an even better look at how GFP(+36) chooses to occupy AfFtn cages, we will look at time-resolved anisotropy of GFP(+36) within AfFtn E65R, a mutant which remains as a 24mer regardless of the ionic strength of the solution but is still able to encapsulate GFP cargo[65]. Homo-FRET data from E65R-GFP(+36) loaded at a 1:1 ratio indicate whether the GFPs will preferentially load multiple copies into a single cage or one copy per cage first when possible before doubling up. This behavior will give important insight into how cargo orders itself within electrostatically assembled cages.

3.3 Conclusions

In this work, we have shown that a +36 overall net charge is not required for encapsulation of GFP within an AfFtn cage, GFP(+28) and GFP(+16)BE are sufficient for mediating this process. Furthermore, we show that lowering the pH reduces the barrier to encapsulation to GFPs with charges as low as +9, due to reducing the electrostatic repulsion between AfFtn subunits. The localization of the charge on the surface of the GFP seems to play a role in whether or not the cage forms, with GFP(+16)BE able to form some amount of 24mer while GFP(+16)bottom and GFP(+16)side do not form any 24mer. Measuring zeta potential shows that there is an experimentally observable charge difference between the GFPs in solution. Thermal shift assays indicate that the GFPs interacting more strongly with ferritin gain more protective effects upon encapsulation, and further stability studies will be interesting to monitor this behavior. Time-resolved fluorescence anisotropy will give insight into how the GFPs behave in the cage and the pattern in which they occupy. Through this work, we outline how to expand the types of protein cargo able to be encapsulated within AfFtn. This method could pave the way for increased uses for these complexes as the protein cages are increasingly used for drug delivery, nanomaterials, and more as this method of electrostatic encapsulation becomes increasingly generalizable through these discoveries.

3.4 Experimental Procedures

Ferritin purification

Ferritin was expressed and purified as previously published[69].

Supercharged GFP purification

Supercharged GFPs were expressed and purified with slight modifications to our previous publication[67]. GFP(+36) was purchased from DNA 2.0 (now ATUM), GFP(+28), GFP(+14), and GFP(+9) were gifts from David Liu (Plasmids 89250, 89252, and 89247),

GFP(+16)bottom and GFP(+16)side were purchased from ATUM, and GFP(+16)BE was made via Gibson assembly[187,188] on a plasmid purchased from ATUM.

GFP sequences

All three GFP(+16) designs have the pJ411 backbone. The insert sequences are as follows:

GFP(+16)bottom:

AAGGAGGTAAAAAATGGGTCATCATCATCATCATCACGGCGGTCGTAGCAAGGGTAAGCGT
CTGTTTCGCGGTAAGGTTCCGATCCTGGTTGAACTGGATGGTGACGTGAATGGTCACAAGTT
TTCTGTTCGCGGCGAGGGTGAGGGCGATGCAACCCGTGGCAAGTTGACCCTGAAGTTTATC
TGCACCACGGGTAAGCTGCCGGTCCCGTGGCCGACGTTAGTGACCACGCTGACCTACGGC
GTCCAGTGTTTCAGCCGTTACCCGAAACACATGAAACGCCACGACTTCTTCAAAAGCGCCAT
GCCGGAAGGCTACGTGCAGGAACGTACCATTAGCTTCAAAGACGACGGTACGTATAAGACT
CGTGCCGAAGTTAAGTTTAAGGGTCGTACCCTGGTGAACAGAATTGAGCTGAAAGGTATCGA
CTTCAAAGAGGATGGTAATATCCTGGGCCACAAATTGGAGTATAACTTTAACAGCCATAACG
TTTACATTACCGCGGATAAGCGCAAAAATGGCATTAAAGCAAATTTCAAAATCCGTCACAACG
TTGAGGATGGTAGCGTGCAACTGGCGGACCACTATCAACAGAATACTCCTATTGGTCGTGG
CCCGGTCCTGCTGCCACGCAATCACTATCTGTCCACCCAATCGGCGCTGAGCAAAGACCCG
AACGAAAAACGTGATCACATGGTCTTGCTGGAATTCGTAACGGCTGCGGGTATCAAACACG
GCCGTGACGAGCGCTACAAGTGATAA

GFP(+16)side:

AAGGAGGTAAAAAATGGGTCATCATCATCATCATCACGGCGGCGCGTCTAAAGGTGAACGT
CTGTTTCGCGGTAAGGTCCCTATTTTGGTTAAGCTGAAGGGTGATGTGAATGGCCACAAGTT
TAGCGTTCGTGGTAAAGGCAAGGGTGATGCGACTCGTGGTAAACTGACCTTGAAATTCATCT
GCACGACGGGTAAGCTGCCGGTCCCGTGGCCGACCCTGGTAACGACCCTGACCTATGGTG

TTCAATGTTTCAGCCGTTACCCGGACCACATGAAACAGCACGATTTCTTCAAAAGCGCGATG
CCGAAAGGCTACGTGCAAGAGCGTACCATCTCGTTTAAAGACGACGGTACGTATAAGACCC
GTGCAGAAGTGAAGTTCGAGGGTCGTACTCTGGTCAACCGCATTGAGTTAAAGGGCATCGA
CTTTAAGGAAGATGGCAATATTCTGGGTCACAAACTGCGCTACAACTTCAACTCCCACAATG
TGTACATTACCGCGGACAAACAGAAAAACGGTATCAAGGCTAACTTTAAGATCCGTCACAAT
GTTGAGGATGGCAGCGTTCAACTGGCCGACCACTATCAGCAGAACACCCCGATTGGTCGTG
GCCCGGTGTTGCTGCCGGACAATCACTATCTGAGCACGCGCAGCGCGCTGAGCAAAGATC
CAAAAGAAAAGCGCGACCACATGGTTCTGCTGGAATTCGTCACGGCCGCAGGCATCACCCA
TGGTATGGATGAACTCTACAAATGATAA

GFP(+16)BE:

AAGGAGGTAAAAAATGGGTCATCATCATCACCATCATGGCGGTGCCTCGAAGGGCGAGCGT
CTTTTCACTGGTGTAGTCCCAATCCTGGTGGAATTGGACGGCGATGTGAACGGTCACAAATT
CTCAGTGCGTGGGGAGGGCGAAGGCGACGCTACCCGTGGCAAGCTGACGCTTAAGTTCAT
TTGCACCACAGGGAAACTGCCGGTGCCGTGGCCTACGTTGGTAACGACTCTTACGTATGGA
GTTCAGTGTTTTTCCCGTTACCCGAAACACATGAAGCGTCACGATTTTTTTAAATCCGCCATG
CCCGAAGGGTACGTACAAGAACGTACGATCTCATTTAAAAAGGACGGAACTTACAAAACTCG
CGCGGAAGTTAAGTTCGAGGGACGTACGTTGGTTAACCGCATTGAATTGAAGGGCCGTGAT
TTTAAGGAAAAAGGTAACATCTTGGGGCACAAATTGCGTTATAATTTCAACTCCCACAACGTC
TACATTACAGCGGATAAACGTAAAAATGGCATCAAAGCCAATTTTAAAATTCGCCACAATGTA
AAAGACGGATCTGTTCAGTTAGCAGATCACTATCAACAAAATACTCCGATTGGCCGCGGTCC
GGTGTTACTGCCTCGTAACCACTACTTAAGTACCCAGTCTGTCTTATCAAAAGACCCAAAAGA
GAAACGCGACCACATGGTACTTCTTGAATTTGTCACGGCTGCTGGTATTACCCACGGGATGG
ACGAGCTGTACAAA

Size exclusion chromatography sample preparation

AfFtn-GFP complexes were formed by mixing AfFtn and GFP in a 1:x ratio in no salt buffer (20 mM phos, pH 7.6 or 5.8) at a concentration of 6 μM and equilibrating at 4 °C for 3 – 24 hours.

Analytical size exclusion chromatography

Analytical size exclusion chromatography was done on an AKTA Pure FPLC system using a Superdex200 Increase 10/300 GL column equilibrated with no salt buffer (20 mM phos, pH 7.6 or 5.8). 200 μL of sample was injected and A280 and A488 were monitored. Sample was eluted at 4 °C using a flow rate of 1.0 mL/min.

Native gel electrophoresis

Native gels (0.7% agarose) were prepared using 5 mM NaCl, 20 mM phos, pH 7.6. Samples were mixed with glycerol (final concentration 16% v/v). Gels were run at 100 V for 20 min on ice, with the lights off. Gels were imaged using a Typhoon FLA7000 imager using an excitation wavelength of 472 nm and PMT setting of 500 V. Following fluorescence imaging, gels were stained with Coomassie Brilliant Blue R-250.

Determination of GFP loading

Loading of GFP was determined as previously described with the modification that comparisons were made using SEC A280 and A488.

Differential scanning fluorimetry

Melting temperature (T_m) was measured by performing differential scanning fluorimetry on the GFP fluorophore. 100 μL of 0.5 μM GFP per sample was prepared in no salt buffer at pH 7.6 or 5.8 and added to a 0.2 mL non-skirted 96-well PCR plate (Thermo scientific AB-0600) sealed with Microseal® 'B' seal seals (BioRad MSB1001). Plates were run on a Stratagene Mx3000P using the SYBR Green method (FAM filter set, 1x gain, ex: 492 nm em: 516 nm) measuring residual GFP fluorescence while the temperature was increased from 25 °C to 99 °C

at 1 °C per min and T_m was determined based on where -R'(T) reached its maximum. All samples were measured in triplicate.

Zeta potential

Zeta potential was measured on a Malvern Zetasizer Nano ZS (2 min equilibration time). 1 μM GFP samples in 50 mM HEPES pH 7.5 buffer were loaded into folded capillary cells (Malvern Panalytical, DTS1070) and all measurements were done in triplicate.

Fluorescence polarization/anisotropy

100 μL of 1 μM GFP samples were loaded into a black 96 well plate (Greiner Bio, 655906). Samples were measured on a Tecan Infinite F200 Fluorescence Microplate Reader using the fluorescence polarization method equipped with the fluorescein polarization filter (ex 485 nm: em: 535 nm) and the gain manually set to 50. All samples were measured in triplicate.

3.5 Acknowledgments

Funding for this work was provided by the NSF (CHE-1905203), the Vagelos Institute for Energy Science and Technology (graduate fellowship), and the LRSM MRSEC IRG-3 (NSF DMR-1720530). Grey Guo and Dr. Jeffery G. Saven are acknowledged for their work computationally designing GFP(+16)bottom and GFP(+16)side. Tom Troxler and Dr. Sergei Vinogradov are acknowledged for helpful discussions and the design and execution of time-resolved fluorescence anisotropy measurements. We are grateful to Dr. Julie Blendy for the use of her qPCR and to Julia Ferrante for instruction on how to use the instrument. We are also grateful to D. Miklos Robkis and Kristen Fiore for providing protocols for Gibson assembly and helpful discussions.

CHAPTER 4: CONCLUSIONS AND FUTURE DIRECTIONS

The work described in this dissertation has demonstrated the versatility of AfFtn for the encapsulation of protein and enzyme cargo and has provided a blueprint for generalizable approaches for continuing to expand the variety of cargo that can template ferritin assembly. We have successfully designed and purified an active superpositively charged enzyme, hCAII(+21), and shown that it is able to form AfFtn 24mers. Furthermore, the enzyme remains highly active within the ferritin cage. The AfFtn-hCAII(+21) complex was amenable to immobilization on a solid substrate, and gained thermal stability upon immobilization. We have expanded the working knowledge of charge requirements for cargo encapsulation by AfFtn at physiological pH by probing a variety of supercharged GFPs as well as Janus-faced and bilobal GFP variants. Lowering the pH to help overcome electrostatic repulsion between AfFtn subunits greatly reduces the amount of charge necessary to get cargo inside the cage. We have also introduced several novel encapsulation assays and stability studies.

While significant effort has gone toward understanding GFP charge magnitude and distribution requirements for encapsulation, there is still considerable work to be done. A GFP protein with 16 positive charges distributed at both ends (top and bottom) of the protein (GFP(+16)BE) is able to form a modest amount of AfFtn 24mer, whereas GFP(+16)side, GFP(+16)bottom, and GFP(+14) variants cannot template ferritin assembly. Further studies are necessary to ascertain why this phenomenon is seen. Preliminary molecular dynamics simulations have shown that the ends of the GFP interact first with the E-helices of different AfFtn dimers, which presents an interesting hypothesis that GFP might bridge and brace two sets of hexamers. It will be interesting to see if a GFP(+28)BE or GFP(+36)BE design might form even more stable assemblies.

A majority of the efforts for understanding the assembly have gone towards cargo engineering while there remain many fascinating areas to explore with ferritin interior design. As a result of the same molecular dynamics simulations described in the previous paragraph, we have designed two AfFtn mutants, AfFtn3posE and AfFtn4negE as described in Appendix A, which

either have additional positive or negative charges added to the E-helix. We expect to see that the more positively charged E-helix would disfavor encapsulation, while a more negatively charged E-helix should increase the interaction with positively charged cargo. The positively charged E-helix mutant may also be able to help expand the variety of nanoparticles encapsulated, as many nanoparticles have negative overall surface charges due to their capping ligands.

Based on the advances made in loading, single enzyme studies are now possible within the AfFtn cage. Any protein small enough to fit in the AfFtn cage can feasibly be fused with GFP(+36) and be loaded at pH 5.8 to study the difference between single enzyme loading vs multiple copies occupying the same cage, or the surface can be redesigned to be more positively charged for encapsulation. Molecular crowding can also be simulated with high encapsulation molarity. It remains to be seen if further improvement of enzymes and expanding the variety of immobilized surfaces in conjunction with improving hCAII(+21) activity and thermostability, for example, can increase the utility of AfFtn-immobilized enzymes.

Another exciting area for exploration is AfFtn for the delivery of therapeutics. Advancements have been made in the realm of biocompatibility with the design HuAfFtn, but current delivery strategies with AfFtn rely on either using HuAfFtn targeting TfR1 or labeling the surface of AfFtn with antibodies. HuAfFtn loading has only been explored in the context of salt-dependent assembly, it remains to be explored how well it would work for cargo-templated assembly. Additionally, while proteins are useful for enabling post-synthetic modifications, this does not represent the most efficient route to targeted drug delivery. Other ferritins have been successfully genetically fused at the N terminus with large complexes like SARS-CoV-2 proteins and peptides forming trimeric-presenting assemblies at the 3-fold pores[54,56,58,189]. They have also been fused with *N*-terminal targeting peptides, but loading cargo still requires disassembly at very low or very high pH. Initial attempts at genetically fusing AfFtn with peptides still has troubleshooting to be performed, but successful genetic fusions of AfFtn with targeting peptides

or nanobodies could reduce the inefficiencies and issues with pH-based assembly/disassembly and surface labeling.

In conclusion, our results help pave the way for greatly expanded cargo loading using AfFtn beyond just highly supercharged proteins/protein fusions or very specific nanoparticles while also allowing for more precise control over cargo loading stoichiometry. The resulting assemblies could expand applications of protein-based nanocapsules for heterogeneous catalysis, single-enzyme studies, green chemistry, targeted drug delivery, vaccine presentation, and bioimaging.

APPENDIX A: FERRITIN MODIFICATIONS

A.1 AfFtn in drug delivery

As mentioned in the introduction, there are many uses for ferritin as a vehicle for drug delivery. The use of AfFtn has been shown to have its benefits, with the ability to disassemble, load, and reassemble the cage under mild pH conditions using ionic strength[15,72], but so far no one has leveraged cargo-templated assembly to further simplify the loading process. The current strategy requires the conjugation of the cargo to AfFtn with an interior cysteine mutation (after reduction by TCEP) under low salt conditions, increasing the salt concentration to assemble the cages, crosslinking the cages, then moving back to low salt in order to antibody label the surface of the cage[15] (Figure A.1). Not only is this process five steps, but each step requires purification as well. Using cargo-templated assembly of AfFtn would eliminate the need to move back and forth between low and high salt to assemble, forgo the requirement to cross-link the cage as well, and remove the associated additional purification steps.

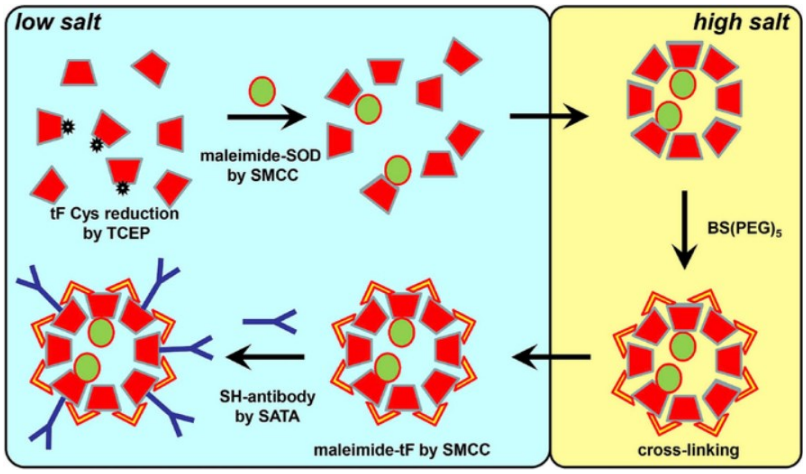

Figure A.1. Scheme of antibody/AfFtn/cargo preparation. Preparation of antibody/AfFtn/cargo complexes requires single-cysteine-containing thermophilic ferritin reduction by TCEP, followed by conjugated with maleimide-SOD, transfer to high salt to reassemble and to cross-link using $BS(PEG)_5$, where crosslinked ferritin is next transferred back to low salt then antibodies are conjugated to the surface of reassembled particles. Figure reproduced from reference 15.

To test the delivery of cargo-templated AfFtn, we first chose the desired cargo. In previous work, superoxide dismutase (SOD) from bovine erythrocyte, a 32.5 kDa dimeric Cu-Zn enzyme which catalyzes the dismutation of superoxide in to O_2 and H_2O_2, was used. One of the challenges of fusing GFP(+36) with a dimeric enzyme is that we are unsure of how the activity would be affected or if the fusion would get encapsulated by AfFtn. To circumvent this, we fused GFP(+36) with a monomeric SOD from *E. coli*[190]. This GFP(+36)-SOD fusion was able to be encapsulated by AfFtn and loaded very similarly to GFP(+36) alone. AfFtn/GFP(+36)-SOD was also found to have very similar activity to GFP(+36)-SOD, indicating that encapsulation does not affect the activity of the enzyme (Figure A.2). Initially testing crosslinking of the complex with $BS(PEG)_5$, AfFtn-GFP(+36) lost over 90% of its activity. Directly modifying the surface of AfFtn with SMCC then conjugating MECA32 (an antibody for caveolar targeting) to the surface led to a 40% reduction in activity. Using non-crosslinked complexes, we were able to inject them in mice and then challenge the mice with lipopolysaccharide, but little therapeutic effect was seen for treated vs untreated mice. Using GFP fluorescence to image the process, it appears that they are finding their target, but monomeric bacterial SOD might not be the best enzyme to use for therapeutics.

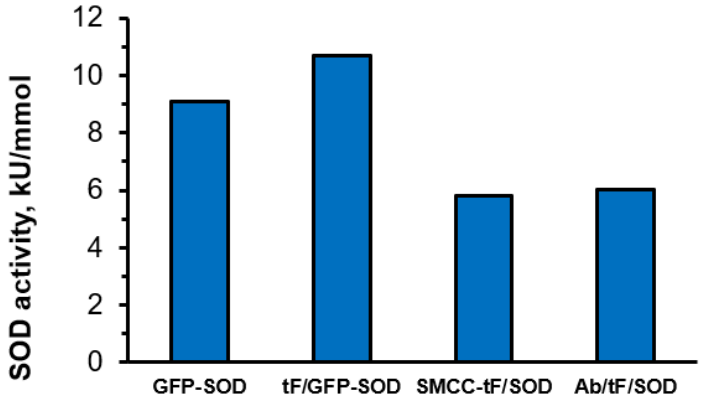

Figure A.2. GFP-SOD activity. GFP(+36)-SOD and AfFtn/GFP(+36)-SOD had very similar activity, indicating that encapsulation did not affect SOD activity, but surface modification of

AfFtn/GFP(+36)-SOD resulted in a decrease of activity. Subsequent conjugation of antibodies to the SMCC-modified AfFtn did not further decrease activity.

Going forward, we would like to try loading more active enzymes into the cage that are able to have a therapeutic effect. Using an obscure monomeric SOD from *E. coli* might not have the same activity as a more conventional dimeric mammalian SOD, especially *in vivo*. The AfFtn cage should have space to accommodate a dimeric GFP(+36)-SOD fusion, so fusing GFP(+36) with SOD from bovine erythrocytes seems like a natural next step, as well as any other therapeutic GFP(+36)-enzyme fusion a collaborator may be interested in trying. Preliminary data using GFP(+36) in AfFtn to image the delivery process *in vivo* seems promising and could be a great alternative to dye-labeling.

A.2 AfFtn protein arrays

Nanoparticles have interesting catalytic and optical properties that are distinct from their atomic or molecular precursors and their bulk counterparts. Due to the wide variety of compositions, sizes, and other properties of nanoparticles, they have many uses as heterogeneous catalysts, semiconductors, imaging agents and more[191]. Managing the spacing and assembly state of these particle affords precise control of the properties of these materials. This led to the field of programmable nanomaterials, where superlattices of nanoparticles are formed using different linkers to manipulate the spacing and geometry of these particles[192]. One of the main strategies employed involves attaching DNA oligos to the surface of the nanoparticles. These oligos hybridize via canonical Watson-Crick base pairing with oligos on the surface of other nanoparticles to form the connections between nanoparticles. Oligo sequence and length can be varied in order to control which particles interact and the spacing of these particles. Despite these advances, the use of DNA oligos is costly, and site-specifically attaching these oligos and determining coverage density remains a challenge. Furthermore, the perfection of the lattice is partially dependent on the monodispersity of the nanoparticles themselves, which often can be challenging to produce[193]. To achieve the goals of developing materials with better

control of linker attachment and stoichiometry as well as using a more uniformly sized building block, we turned to AfFtn. Ferritins provide stable protein cages, amenable to many modifications via site-directed mutagenesis and synthetic chemistry. We previously demonstrated efficient encapsulation of inorganic nanoparticles within AfFtn[61,63]. One previous study introduced a tetrahedral Zn^{2+}-binding site at the small, 3-fold symmetric channels of HuHFtn via a T122H mutation and linked together cages using a bishydroxamate linker[50]. Here, we seek to expand on and improve this technology (Figure A.3).

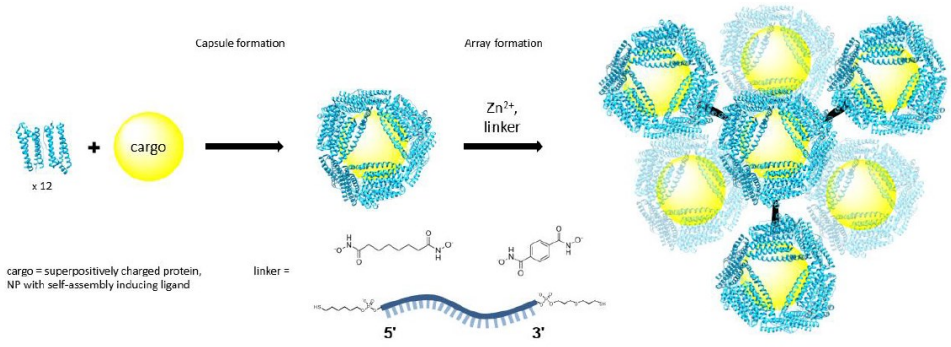

Figure A.3. Scheme of proposed AfFtn capsule and array formation. Using nanoparticle or superpositively charged protein cargo, AfFtn capsules are formed, to which Zn^{2+} and a variety of linkers can be added to form arrays of cargo-templated protein capsules with tunable distances and geometries.

To modify AfFtn to have 4 tetrahedrally-arranged Zn^{2+}-binding sites at the small, 3-fold symmetrical pores, we introduced a similar mutation to the previous work at Y119H (Figure A.4), with the resulting cages would link in a tetrahedral geometry. We synthesized a bishydroxamate linker, benzene-1,4-dihydroxamate, which is capable of bridging Zn^{2+}-binding sites of adjacent HuHFtn T122H cages. We observe that without all 3 components--the AfFtn cage, Zn^{2+} and linker--larger supramolecular assemblies do not form, but adding all 3 together with 1.4 μM empty, assembled AfFtn, 75 μM Zn^{2+} and 1 mM linker, produces larger structures as observed by dynamic light scattering (DLS) (Figure A.5). Unfortunately, the arrays are not observable by small

angle x-ray scattering, and larger structures are not produced with cargo loaded in Y119H. While it might be easier to load cargo into AfFtn over another ferritin like HuHFtn, there are still significant roadblocks to overcome with getting loaded AfFtn to form these supramolecular assemblies.

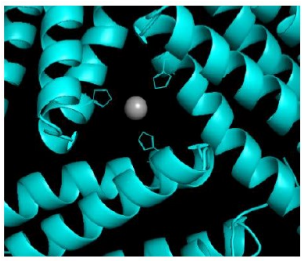

Figure A.4. AfFtn Y119H Zn2+ binding. AfFtn Y119H introduces His residues to the small, 3-fold symmetric pore, with this figure showing the side-chains as sticks and a theoretical Zn^{2+} that cand bind at this site as a grey sphere.

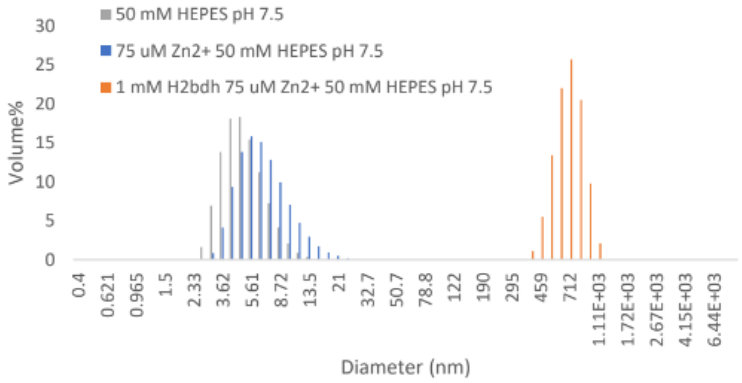

Figure A.5. DLS of Y119H assemblies. DLS of 1.4 μM AfFtn Y119H in HEPES buffer alone (grey) and with 75 μM Zn^{2+} (blue) show no larger supramolecular assembly, while adding 75 μM Zn^{2+} and 1 mM benzene-1,4-dihydroxamate (orange) shows >99% assembly into some larger order structure.

A.3 AfFtn as a platform for vaccine presentation

For the past 24+ months, the world has been enduring the SARS-CoV-2 pandemic. The development of safe and effective vaccines against this novel coronavirus have provided protection to individuals from severe symptoms of the disease, as well as curbed the actual spread of the disease from vaccinated individuals. The FDA has authorized three COVID-19 vaccines for emergency use in the US, manufactured by Pfizer-BioNTech, Moderna, and Janssen. The former two mRNA-based vaccines exhibit a relatively high efficacy of about 95% but require ultra-cold chain transportation and storage in -20 °C and -80 °C, while the latter viral vector-based vaccine could elicit strong immune responses with one single shot but with more frequent and severe side effects[194]. Some examples exist of ferritin-based vaccine platforms[54,56,58,189]. In these cases, *H. pylori* ferritin or HuHFtn will display 24 full-length spike proteins or truncated spike protein-derived peptides in a trimeric presentation, which boosts the immune response. The Maris lab at UPenn released a computational study predicting that specific 33mer peptide antigens can activate CD4 and CD8 T-cells in 99.4% of the population[195]. We seek to use a AfFtn-based platform displaying these 33mer peptides on the surface, which can be expressed in *E. coli* rather than requiring expression in mammalian cells by selecting sequences that do not require glycosylation (Figure A.6). The AfFtn-based system has the added advantage of easy loading of GFP(+36) for imaging, forgoing the need for fluorescent labels on the outer surface.

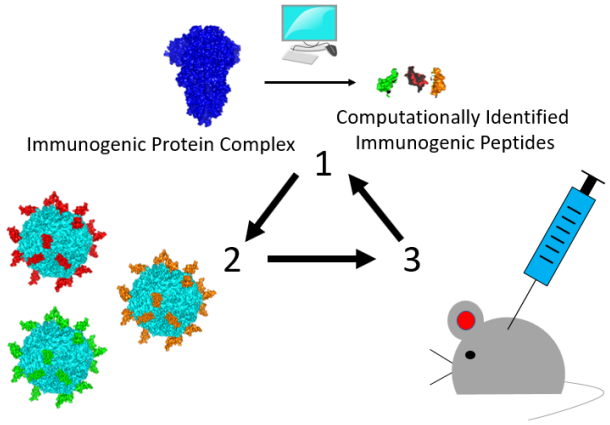

Figure A.6 Scheme for antigen presentation using AfFtn. Promising 33mer peptides from non-glycosylated regions the antigen of interest are identified *in silico*, and will be expressed in *E. coli* and purified as ferritin-peptide conjugates, which can then be used to elicit and immune response in mice.

The AfFtn-based vaccine platform was designed with an N-terminal 33mer COVID spike peptide from the receptor binding domain (LPDPSKPSKRSFIEDLLFNKVTLADAGFIKQYG) linked to E65R AfFtn. E65R was chosen because it exists as 24mers at neutral pH at all ionic strengths, unlike AfFtn wt, which disassembles into dimers at low ionic strength. Efforts to purify the 33mer-E65R fusion lead to very wide peaks by SEC where the 33mer-E65R fusion were inseparable from something the size of ferritin without the 33mer fusion. Mutagenesis of M1G in the E65R portion did not yield any noticeable differences, so an N-terminal His tag was introduced to allow for the separation of full-length fusion from ferritin. Upon purification, it was found that 33mer-E65R exists as dimers, even under high ionic strength conditions (Figure A.7). This 33mer-E65R dimer complex could still form 24mer when incubated with AfFtn wt under high salt conditions in a 1:11 ratio, however (Figure A.8). The 33mer-E65R – AfFtn wt complexes were incubated with Ni-NTA to ensure that the complex observed contains the 33mer-E65R, which has a His tag.

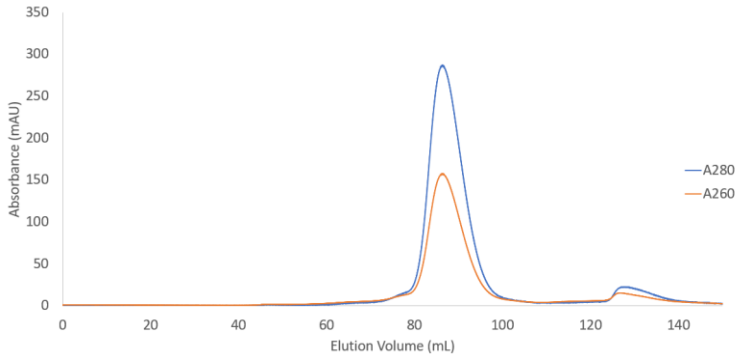

Figure A.7 33mer-E65R SEC. The 33mer-E65R fusion elutes around 90 mL on the HiLoad Superdex200 column, where AfFtn dimer normally elutes.

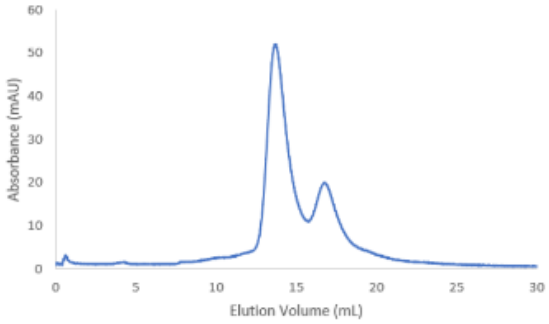

Figure A.8. 33mer-E65R 24mer formation. 33mer-E65R fusion incubated with AfFtn wt in a 1:11 ratio at 800 mM NaCl forms a ferritin complex incorporating the 33mer-E65R fusion.

Going forward, it still remains to be seen if GFP(+36) can template assembly of a mixture of 33mer-E65R and AfFtn wt around it for use in fluorescence imaging. Peptide-ferritin conjugates can be tested in mice, looking for neutralizing antibody and T-cell responses. Based on these results, we may fuse other 33mer peptides with ferritin to use in a cocktail for optimal immune response. If a low immune response is observed, we may have to fuse the 33mer peptide with different ferritins or use a different method of attachment like a SpyTag/SpyCatcher system in order to get trimeric presentation of the antigen on the surface of the ferritin. Eventually, being able to get a 33-mer-E65R complex that can assemble in solution on its own might lead to the potential to make this an mRNA vaccine for the organism to express directly. For now, more work

needs to be done to see how N-terminal fusion of the 33mer peptide interferes with AfFtn 24mer assembly.

APPENDIX B: Supplementary Figures

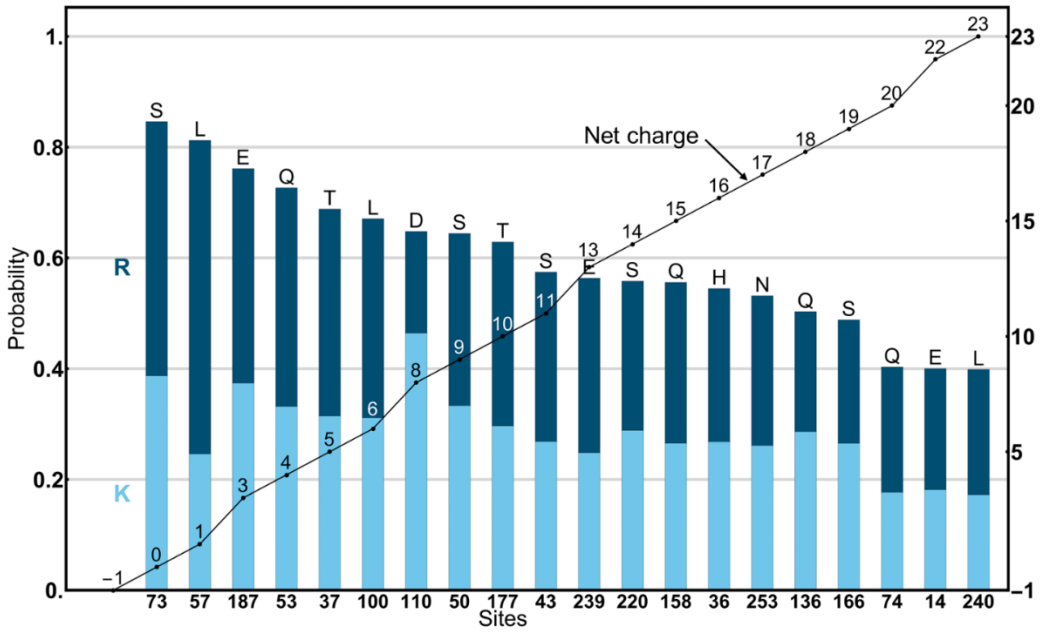

Figure B.1. Probability (p+) of K and R for incorporation at exterior residues ranked from highest to lowest. This set has the largest values of p_+ among the 48 sites considered for mutation to increase positive charge. The probability of K is plotted as light blue bars, and the probability of R is plotted as dark blue bars stacking on top of K for each residue. The x-axis indicates the site number, and the letter above the bars shows the wild type amino acid at the site. The line plot shows how the putative net charge at pH 7 of hCAII changes if mutations (from wild type to K or R) are made in succession, where the starting charge of -1 at neutral pH is the net charge of wild-type hCAII.

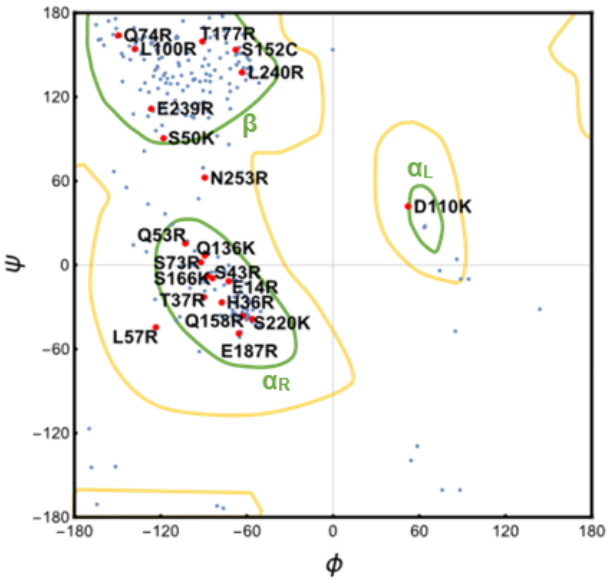

Figure B.2. Ramachandran plot showing torsional angles, φ and ψ, of all residues in hCAII. Designed 21 residues (including S152C and 20 mutations) are indicated in red; remaining (nonmutated) residues are blue. Residue 110 is D (wt) in the +21 mutant hCAII(+21). Green contours outline regions of secondary structure: β sheet structures; α_R right-handed α-helices; and α_L the α-left region.

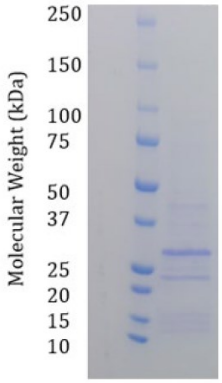

Figure B.3. SDS-PAGE analysis of overexpression of hCAII(+23). SDS-PAGE of the insoluble fraction indicates that overexpression of the hCAII(+23) mutant containing D110K resulted in inclusion bodies.

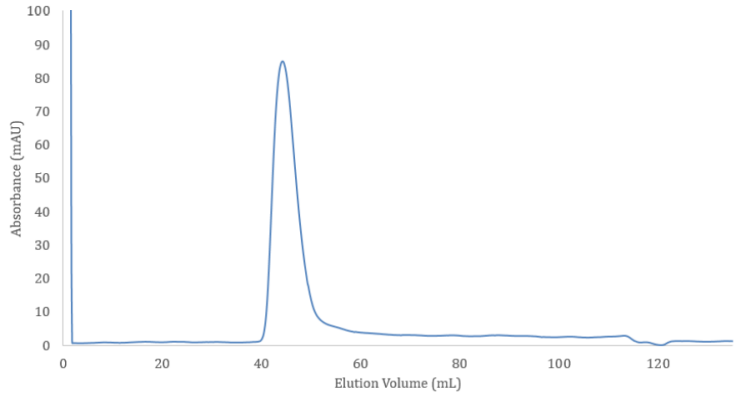

Figure B.4. SEC analysis of hCAII(+23) mutant. Elution of the small soluble fraction of D110K-containing mutant hCAII(+23) results in inactive, soluble aggregates eluting in the void volume of the sizing column.

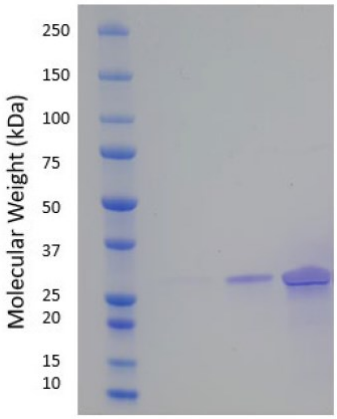

Figure B.5. SDS-PAGE analysis of hCAII(+21) mutant. SDS-PAGE of hCAII(+21) indicates the correct MW and expected purity (> 95%).

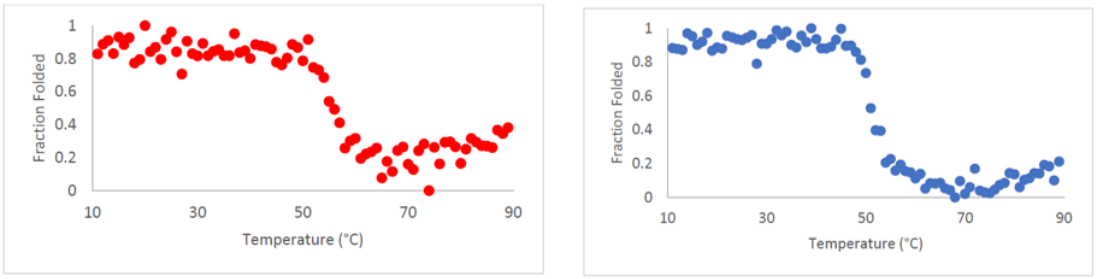

Figure B.6. CD thermal melts of hCAII wt (left) and hCAII(+21) (right) monitored at 205 nm. CD thermal melting curves of hCAII wt (A) and hCAII(+21) (B) show that the superpositively charged mutant loses only 4 °C of thermal stability relative to the wild-type enzyme (Tm = 55 °C → 51 °C).

```
                 •    10    •    20    •    30    •    40    •    50    •    60
hCAII            MAHHWGYGKHNGPEHWHKDFPIAKGERQSPVDIDTHTAKYDPSLKPLSVSYDQATSLRIL
hCAII(+21)       MAHHWGYGKHNGPRHWHKDFPIAKGERQSPVDIDTRRAKYDPRLKPLSVKYDRATSRRIL
                 •    70    •    80    •    90    •   100    •   110    •   120
hCAII            NNGHAFNVEFDDSQDKAVLKGGPLDGTYRLIQFHFHWGSLDGQGSEHTVDKKKYAAELHL
hCAII(+21)       NNGHAFNVEFDDRRDKAVLKGGPLDGTYRLIQFHFHWGSRDGQGSEHTVDKKKYAAELHL
                 •   131    •   141    •   151    •   161    •   171    •   181
hCAII            VHWNTKYGDFGKAVQQPDGLAVLGIFLKVGSAKPGLQKVVDVLDSIKTKGKSADFTNFDP
hCAII(+21)       VHWNTKYGDFGKAVKQPDGLAVLGIFLKVGCAKPGLRKVVDVLDKIKTKGKSADFRNFDP
                 •   191    •   201    •   211    •   221    •   231    •   241
hCAII            RGLLPESLDYWTYPGSLTTPPLLECVTWIVLKEPISVSSEQVLKFRKLNFNGEGEPEELM
hCAII(+21)       RGLLPRSLDYWTYPGSLTTPPLLECVTWIVLKEPISVSKEQVLKFRKLNFNGEGEPERRM
                 •   251    •   261
hCAII            VDNWRPAQPLKNRQIKASFK
hCAII(+21)       VDNWRPAQPLKRRQIKASFK
```

Figure B.7. Sequence alignment of hCAII wt and hCAII(+21). Changes between the wt and +21 sequence are shown in blue.

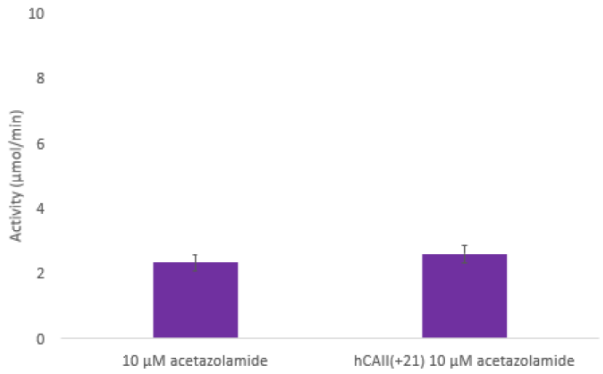

Figure B.8. Inhibition of hCAII(+21) by acetazolamide. hCAII(+21) showed no pNPA esterase activity after adding 10 µM acetazolamide, confirming that hCAII(+21) is responsible for activity. Error bars indicate the standard error of triplicate measurements.

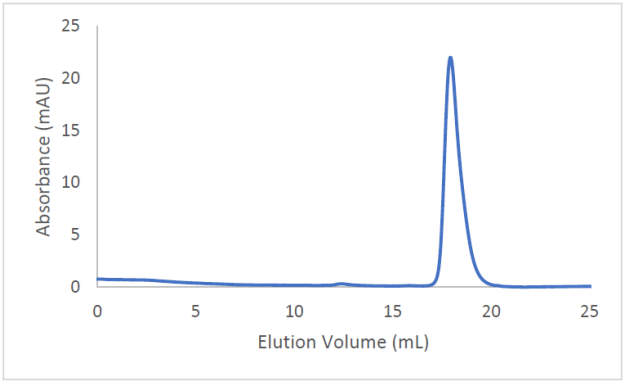

Figure B.9. SEC analysis of AfFtn-hCAII wt at 0 mM NaCl. AfFtn does not form 24mer cages around hCAII wt, as indicated by the elution of only a single peak corresponding to AfFtn dimer.

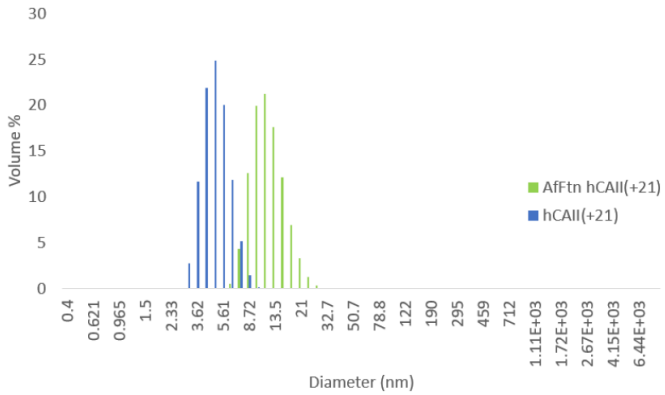

Figure B.10. DLS analysis of hCAII(+21) and AfFtn-hCAII(+21). The purified host-guest complex shows size (roughly 13 nm diameter) that is consistent with AfFtn 24mer.

BIBLIOGRAPHY

(1) Rother, M., Nussbaumer, M. G., Renggli, K., and Bruns, N. (2016) Protein cages and synthetic polymers: a fruitful symbiosis for drug delivery applications, bionanotechnology and materials science. *Chem. Soc. Rev. 45*, 6213–6249.

(2) Sommer, M., Cai, F., Melnicki, M., and Kerfeld, C. A. (2017) β-Carboxysome bioinformatics: identification and evolution of new bacterial microcompartment protein gene classes and core locus constraints. *J. Exp. Bot. 68*, 3841–3855.

(3) Corchero, J. L., and Cedano, J. (2011) Self-assembling, protein-based intracellular bacterial organelles: Emerging vehicles for encapsulating, targeting and delivering therapeutical cargoes. *Microb. Cell Fact. 10*, 92.

(4) Kedersha, N. L., Heuser, J. E., Chugani, D. C., and Rome, L. H. (1991) Vaults. III. Vault ribonucleoprotein particles open into flower-like structures with octagonal symmetry. *J. Cell Biol. 112*, 225–235.

(5) Ding, K., Zhang, X., Mrazek, J., Kickhoefer, V. A., Lai, M., Ng, H. L., Yang, O. O., Rome, L. H., and Zhou, Z. H. (2018) Solution Structures of Engineered Vault Particles. *Structure 26*, 619-626.e3.

(6) Roos, W. H., Ivanovska, I. L., Evilevitch, A., and Wuite, G. J. L. (2007) Viral capsids: mechanical characteristics, genome packaging and delivery mechanisms. *Cell. Mol. Life Sci. 64*, 1484–1497.

(7) Matsuura, K. (2018) Synthetic approaches to construct viral capsid-like spherical nanomaterials. *Chem. Commun. 54*, 8944–8959.

(8) de Ruiter, M. V., van der Hee, R. M., Driessen, A. J. M., Keurhorst, E. D., Hamid, M., and Cornelissen, J. J. L. M. (2019) Polymorphic assembly of virus-capsid proteins around DNA and the cellular uptake of the resulting particles. *J. Control. Release 307*, 342–354.

(9) Uchida, M., Kang, S., Reichhardt, C., Harlen, K., and Douglas, T. (2010) The ferritin superfamily: Supramolecular templates for materials synthesis. *Biochim. Biophys. Acta - Gen. Subj. 1800*, 834–845.

(10) Jutz, G., Van Rijn, P., Santos Miranda, B., and Böker, A. (2015) Ferritin: A versatile building block for bionanotechnology. *Chem. Rev. 115*, 1653–1701.

(11) Patterson, D. P., Prevelige, P. E., and Douglas, T. (2012) Nanoreactors by programmed enzyme encapsulation inside the capsid of the bacteriophage P22. *ACS Nano 6*, 5000–5009.

(12) Azuma, Y., Edwardson, T. G. W., and Hilvert, D. (2018) Tailoring lumazine synthase assemblies for bionanotechnology. *Chem. Soc. Rev. 47*, 3543–3557.

(13) Khoshnejad, M., Parhiz, H., Shuvaev, V. V., Dmochowski, I. J., and Muzykantov, V. R. (2018) Ferritin-based drug delivery systems: Hybrid nanocarriers for vascular immunotargeting. *J. Control. Release 282*, 13–24.

(14) Khoshnejad, M., Shuvaev, V. V., Pulsipher, K. W., Dai, C., Hood, E. D., Arguiri, E., Christofidou-Solomidou, M., Dmochowski, I. J., Greineder, C. F., and Muzykantov, V. R. (2016) Vascular accessibility of endothelial targeted ferritin nanoparticles. *Bioconjug. Chem. 27*, 628–637.

(15) Shuvaev, V. V., Khoshnejad, M., Pulsipher, K. W., Kiseleva, R. Y., Arguiri, E., Cheung-Lau, J. C., LeFort, K. M., Christofidou-Solomidou, M., Stan, R. V., Dmochowski, I. J., and Muzykantov, V. R. (2018) Spatially controlled assembly of affinity ligand and enzyme cargo enables targeting ferritin nanocarriers to caveolae. *Biomaterials 185*, 348–359.

(16) Macone, A., Masciarelli, S., Palombarini, F., Quaglio, D., Boffi, A., Trabuco, M. C., Baiocco, P., Fazi, F., and Bonamore, A. (2019) Ferritin nanovehicle for targeted delivery of cytochrome C to cancer cells. *Sci. Rep. 9*, 11749.

(17) Edwardson, T. G. W., Mori, T., and Hilvert, D. (2018) Rational engineering of a designed protein cage for siRNA delivery. *J. Am. Chem. Soc. 140*, 10439–10442.

(18) Palombarini, F., Fabio, E. Di, Boffi, A., Macone, A., and Bonamore, A. (2020) Ferritin nanocages for protein delivery to tumor cells. *Molecules 25*, 825.

(19) Zhang, W., Xu, C., Yin, G. Q., Zhang, X. E., Wang, Q., and Li, F. (2017) Encapsulation of inorganic nanomaterials inside virus-based nanoparticles for bioimaging. *Nanotheranostics 1*, 358–368.

(20) Khoshnejad, M., Greineder, C. F., Pulsipher, K. W., Villa, C. H., Altun, B., Pan, D. C., Tsourkas, A., Dmochowski, I. J., and Muzykantov, V. R. (2018) Ferritin nanocages with biologically orthogonal conjugation for vascular targeting and imaging. *Bioconjug. Chem. 29*, 1209–1218.

(21) Chakraborti, S., Lin, T. Y., Glatt, S., and Heddle, J. G. (2020) Enzyme encapsulation by protein cages. *RSC Adv. 10*, 13293–13301.

(22) Brasch, M., Putri, R. M., De Ruiter, M. V., Luque, D., Koay, M. S. T., Castón, J. R., and Cornelissen, J. J. L. M. (2017) Assembling enzymatic cascade pathways inside virus-based nanocages using dual-tasking nucleic acid tags. *J. Am. Chem. Soc. 139*, 1512–1519.

(23) Azuma, Y., Bader, D. L. V., and Hilvert, D. (2018) Substrate sorting by a supercharged nanoreactor. *J. Am. Chem. Soc. 140*, 860–863.

(24) Schoonen, L., Nolte, R. J. M., and Van Hest, J. C. M. (2016) Highly efficient enzyme encapsulation in a protein nanocage: Towards enzyme catalysis in a cellular nanocompartment mimic. *Nanoscale 8*, 14467–14472.

(25) Schoonen, L., Maassen, S., Nolte, R. J. M., and Van Hest, J. C. M. (2017) Stabilization of a virus-like particle and its application as a nanoreactor at physiological conditions. *Biomacromolecules 18*, 3492–3497.

(26) Giessen, T. W., and Silver, P. A. (2016) A catalytic nanoreactor based on in vivo encapsulation of multiple enzymes in an engineered protein nanocompartment. *ChemBioChem 17*, 1931–1935.

(27) Lizatović, R., Assent, M., Barendregt, A., Dahlin, J., Bille, A., Satzinger, K., Tupina, D., Heck, A. J. R., Wennmalm, S., and André, I. (2018) A protein-based encapsulation system with calcium-controlled cargo loading and detachment. *Angew. Chemie - Int. Ed. 57*, 11334–11338.

(28) Quin, M. B., Perdue, S. A., Hsu, S. Y., and Schmidt-Dannert, C. (2016) Encapsulation of multiple cargo proteins within recombinant Eut nanocompartments. *Appl. Microbiol. Biotechnol. 100*, 9187–9200.

(29) Cassidy-Amstutz, C., Oltrogge, L., Going, C. C., Lee, A., Teng, P., Quintanilla, D., East-Seletsky, A., Williams, E. R., and Savage, D. F. (2016) Identification of a minimal peptide tag for in vivo and in vitro loading of encapsulin. *Biochemistry 55*, 3461–3468.

(30) Sutter, M., Boehringer, D., Gutmann, S., Günther, S., Prangishvili, D., Loessner, M. J., Stetter, K. O., Weber-Ban, E., and Ban, N. (2008) Structural basis of enzyme encapsulation into a bacterial nanocompartment. *Nat. Struct. Mol. Biol. 15*, 939–947.

(31) Putri, R. M., Allende-Ballestero, C., Luque, D., Klem, R., Rousou, K. A., Liu, A., Traulsen, C. H. H., Rurup, W. F., Koay, M. S. T., Castón, J. R., and Cornelissen, J. J. L. M. (2017) Structural characterization of native and modified encapsulins as nanoplatforms for in vitro catalysis and cellular uptake. *ACS Nano 11*, 12796–12804.

(32) Patterson, D. P., Schwarz, B., El-Boubbou, K., Van Der Oost, J., Prevelige, P. E., and Douglas, T. (2012) Virus-like particle nanoreactors: Programmed encapsulation of the thermostable CelB glycosidase inside the P22 capsid. *Soft Matter 8*, 10158–10166.

(33) O'Neil, A., Prevelige, P. E., Basu, G., and Douglas, T. (2012) Coconfinement of fluorescent proteins: Spatially enforced communication of GFP and mCherry encapsulated within the P22 capsid. *Biomacromolecules 13*, 3902–3907.

(34) Sánchez-Sánchez, L., Tapia-Moreno, A., Juarez-Moreno, K., Patterson, D. P., Cadena-Nava, R. D., Douglas, T., and Vazquez-Duhalt, R. (2015) Design of a VLP-nanovehicle for CYP450 enzymatic activity delivery. *J. Nanobiotechnology 13*, 66.

(35) Kickhoefer, V. A., Garcia, Y., Mikyas, Y., Johansson, E., Zhou, J. C., Raval-Fernandes, S., Minoofar, P., Zink, J. I., Dunn, B., Stewart, P. L., and Rome, L. H. (2005) Engineering of vault nanocapsules with enzymatic and fluorescent. *Proc. Natl. Acad. Sci. U. S. A. 102*, 4348–4352.

(36) Liu, X., and Theil, E. C. (2005) Ferritins: dynamic management of biological iron and oxygen chemistry. *Acc. Chem. Res. 38*, 167–175.

(37) Mohanty, A., Parida, A., Raut, R. K., and Behera, R. K. (2022) Ferritin: A Promising Nanoreactor and Nanocarrier for Bionanotechnology. *ACS Bio Med Chem Au 2*, 258–281.

(38) Behera, R. K., and Theil, E. C. (2014) Moving Fe2+ from ferritin ion channels to catalytic OH centers depends on conserved protein cage carboxylates. *Proc. Natl. Acad. Sci. U. S. A. 111*, 7925–7930.

(39) Tosha, T., Ng, H.-L., Bhattasali, O., Alber, T., and Theil, E. C. (2010) Moving Metal Ions through Ferritin−Protein Nanocages from Three-Fold Pores to Catalytic Sites. *J. Am. Chem. Soc.*

132, 14562–14569.

(40) Toussaint, L., Bertrand, L., Hue, L., Crichton, R. R., and Declercq, J.-P. (2007) High-resolution X-ray structures of human apoferritin H-chain mutants correlated with their activity and metal-binding sites. *J. Mol. Biol. 365*, 440–452.

(41) Honarmand Ebrahimi, K., Hagedoorn, P. L., and Hagen, W. R. (2015) Unity in the biochemistry of the iron-storage proteins ferritin and bacterioferritin. *Chem. Rev. 115*, 295–326.

(42) Kasyutich, O., Ilari, A., Fiorillo, A., Tatchev, D., Hoell, A., and Ceci, P. (2010) Silver Ion Incorporation and Nanoparticle Formation inside the Cavity of Pyrococcus furiosus Ferritin: Structural and Size-Distribution Analyses. *J. Am. Chem. Soc. 132*, 3621–3627.

(43) Kanbak-Aksu, S., Nahid Hasan, M., Hagen, W. R., Hollmann, F., Sordi, D., Sheldon, R. A., and Arends, I. W. C. E. (2012) Ferritin-supported palladium nanoclusters: selective catalysts for aerobic oxidations in water. *Chem. Commun. (Camb). 48*, 5745–5747.

(44) Xing, R., Wang, X., Yan, L., Zhang, C., Yang, Z., Wang, X., and Guo, Z. (2009) Fabrication of water soluble and biocompatible CdSe nanoparticles in apoferritin with the aid of EDTA. *Dalton Trans.* 1710–1713.

(45) Turyanska, L., Bradshaw, T. D., Sharpe, J., Li, M., Mann, S., Thomas, N. R., and Patanè, A. (2009) The Biocompatibility of Apoferritin-Encapsulated PbS Quantum Dots. *Small 5*, 1738–1741.

(46) Sun, C., Yang, H., Yuan, Y., Tian, X., Wang, L., Guo, Y., Xu, L., Lei, J., Gao, N., Anderson, G. J., Liang, X.-J., Chen, C., Zhao, Y., and Nie, G. (2011) Controlling Assembly of Paired Gold Clusters within Apoferritin Nanoreactor for in Vivo Kidney Targeting and Biomedical Imaging. *J. Am. Chem. Soc. 133*, 8617–8624.

(47) Nasrollahi, F., Sana, B., Paramelle, D., Ahadian, S., Khademhosseini, A., and Lim, S. (2020) Incorporation of Graphene Quantum Dots, Iron, and Doxorubicin in/on Ferritin Nanocages for Bimodal Imaging and Drug Delivery. *Adv. Ther. 3*, 1900183.

(48) Sano, K.-I., and Shiba, K. (2008) Stepwise accumulation of layers of aptamer-ornamented ferritins using biomimetic layer-by-layer. *J. Mater. Res. 23*, 3236–3240.

(49) Rourk, C., Huang, Y., Chen, M., and Shen, C. (2021) Indication of Strongly Correlated Electron Transport and Mott Insulator in Disordered Multilayer Ferritin Structures (DMFS). *Mater. (Basel, Switzerland) 14*.

(50) Sontz, P. A., Bailey, J. B., Ahn, S., and Tezcan, F. A. (2015) A Metal Organic Framework with Spherical Protein Nodes: Rational Chemical Design of 3D Protein Crystals. *J. Am. Chem. Soc. 137*, 11598–11601.

(51) Golub, E., Subramanian, R. H., Esselborn, J., Alberstein, R. G., Bailey, J. B., Chiong, J. A., Yan, X., Booth, T., Baker, T. S., and Tezcan, F. A. (2020) Constructing protein polyhedra via orthogonal chemical interactions. *Nature 578*, 172–176.

(52) Li, L., Fang, C. J., Ryan, J. C., Niemi, E. C., Lebrón, J. A., Björkman, P. J., Arase, H., Torti, F. M., Torti, S. V, Nakamura, M. C., and Seaman, W. E. (2010) Binding and uptake of H-ferritin are mediated by human transferrin receptor-1. *Proc. Natl. Acad. Sci. 107*, 3505–3510.

(53) Montemiglio, L. C., Testi, C., Ceci, P., Falvo, E., Pitea, M., Savino, C., Arcovito, A., Peruzzi, G., Baiocco, P., Mancia, F., Boffi, A., des Georges, A., and Vallone, B. (2019) Cryo-EM structure of the human ferritin–transferrin receptor 1 complex. *Nat. Commun. 10*, 1121.

(54) Powell, A. E., Zhang, K., Sanyal, M., Tang, S., Weidenbacher, P. A., Li, S., Pham, T. D., Pak, J. E., Chiu, W., and Kim, P. S. (2021) A Single Immunization with Spike-Functionalized Ferritin Vaccines Elicits Neutralizing Antibody Responses against SARS-CoV-2 in Mice. *ACS Cent. Sci. 7*, 183–199.

(55) Carmen, J. M., Shrivastava, S., Lu, Z., Anderson, A., Morrison, E. B., Sankhala, R. S., Chen, W.-H., Chang, W. C., Bolton, J. S., Matyas, G. R., Michael, N. L., Joyce, M. G., Modjarrad, K., Currier, J. R., Bergmann-Leitner, E., Malloy, A. M. W., and Rao, M. (2021) SARS-CoV-2 ferritin nanoparticle vaccine induces robust innate immune activity driving polyfunctional spike-specific T cell responses. *npj Vaccines 6*, 151.

(56) Joyce, M. G., King, H. A. D., Elakhal-Naouar, I., Ahmed, A., Peachman, K. K., Macedo Cincotta, C., Subra, C., Chen, R. E., Thomas, P. V, Chen, W.-H., Sankhala, R. S., Hajduczki, A., Martinez, E. J., Peterson, C. E., Chang, W. C., Choe, M., Smith, C., Lee, P. J., Headley, J. A., Taddese, M. G., Elyard, H. A., Cook, A., Anderson, A., McGuckin Wuertz, K., Dong, M., Swafford, I., Case, J. B., Currier, J. R., Lal, K. G., Molnar, S., Nair, M. S., Dussupt, V., Daye, S. P., Zeng, X., Barkei, E. K., Staples, H. M., Alfson, K., Carrion, R., Krebs, S. J., Paquin-Proulx, D., Karasavva, N., Polonis, V. R., Jagodzinski, L. L., Amare, M. F., Vasan, S., Scott, P. T., Huang, Y., Ho, D. D., de Val, N., Diamond, M. S., Lewis, M. G., Rao, M., Matyas, G. R., Gromowski, G. D., Peel, S. A., Michael, N. L., Bolton, D. L., and Modjarrad, K. (2022) A SARS-CoV-2 ferritin nanoparticle vaccine elicits protective immune responses in nonhuman primates. *Sci. Transl. Med. 14*, eabi5735.

(57) Rodrigues, M. Q., Alves, P. M., and Roldão, A. (2021) Functionalizing Ferritin Nanoparticles for Vaccine Development. *Pharmaceutics 13*.

(58) Zhang, B., Chao, C. W., Tsybovsky, Y., Abiona, O. M., Hutchinson, G. B., Moliva, J. I., Olia, A. S., Pegu, A., Phung, E., Stewart-Jones, G. B. E., Verardi, R., Wang, L., Wang, S., Werner, A., Yang, E. S., Yap, C., Zhou, T., Mascola, J. R., Sullivan, N. J., Graham, B. S., Corbett, K. S., and Kwong, P. D. (2020) A platform incorporating trimeric antigens into self-assembling nanoparticles reveals SARS-CoV-2-spike nanoparticles to elicit substantially higher neutralizing responses than spike alone. *Sci. Rep. 10*, 18149.

(59) Sana, B., Johnson, E., Magueres, P. Le, Criswell, A., Cascio, D., and Lim, S. (2013) The role of nonconserved residues of archaeoglobus fulgidus ferritin on its unique structure and biophysical properties. *J. Biol. Chem. 288*, 32663–32672.

(60) Johnson, E., Cascio, D., Sawaya, M. R., Gingery, M., and Schröder, I. (2005) Crystal structures of a tetrahedral open pore ferritin from the hyperthermophilic Archaeon Archaeoglobus fulgidus. *Structure 13*, 637–648.

(61) Swift, J., Butts, C. A., Cheung-Lau, J., Yerubandi, V., and Dmochowski, I. J. (2009) Efficient self-assembly of Archaeoglobus fulgidus ferritin around metallic cores. *Langmuir 25*, 5219–5225.

(62) Butts, C. A., Swift, J., Kang, S.-G., Di Costanzo, L., Christianson, D. W., Saven, J. G., and Dmochowski, I. J. (2008) Directing noble metal ion chemistry within a designed ferritin protein. *Biochemistry 47*, 12729–12739.

(63) Cheung-Lau, J. C., Liu, D., Pulsipher, K. W., Liu, W., and Dmochowski, I. J. (2014) Engineering a well-ordered, functional protein-gold nanoparticle assembly. *J. Inorg. Biochem. 130*, 59–68.

(64) Pulsipher, K. W., Honig, S., Deng, S., and Dmochowski, I. J. (2017) Controlling gold nanoparticle seeded growth in thermophilic ferritin protein templates. *J. Inorg. Biochem. 174*, 169–176.

(65) Pulsipher, K. W., Villegas, J. A., Roose, B. W., Hicks, T. L., Yoon, J., Saven, J. G., and Dmochowski, I. J. (2017) Thermophilic ferritin 24mer assembly and nanoparticle encapsulation modulated by interdimer electrostatic repulsion. *Biochemistry 56*, 3596–3606.

(66) Tetter, S., and Hilvert, D. (2017) Enzyme encapsulation by a ferritin cage. *Angew. Chemie - Int. Ed. 56*, 14933–14936.

(67) Pulsipher, K. W., Bulos, J. A., Villegas, J. A., Saven, J. G., and Dmochowski, I. J. (2018) A protein–protein host–guest complex: Thermostable ferritin encapsulating positively supercharged green fluorescent protein. *Protein Sci. 27*, 1755–1766.

(68) Chakraborti, S., Korpi, A., Kumar, M., Stępień, P., Kostiainen, M. A., and Heddle, J. G. (2019) Three-dimensional protein cage array capable of active enzyme capture and artificial chaperone activity. *Nano Lett. 19*, 3918–3924.

(69) Bulos, J. A., Guo, R., Wang, Z., DeLessio, M. A., Saven, J. G., and Dmochowski, I. J. (2021) Design of a Superpositively Charged Enzyme: Human Carbonic Anhydrase II Variant with Ferritin Encapsulation and Immobilization. *Biochemistry 60*, 3596–3609.

(70) Ramos, R., Bernard, J., Ganachaud, F., and Miserez, A. (2022) Protein-Based Encapsulation Strategies: Toward Micro- and Nanoscale Carriers with Increased Functionality. *Small Sci. 2*, 2100095.

(71) de Turris, V., Cardoso Trabuco, M., Peruzzi, G., Boffi, A., Testi, C., Vallone, B., Celeste Montemiglio, L., Georges, A. Des, Calisti, L., Benni, I., Bonamore, A., and Baiocco, P. (2017) Humanized archaeal ferritin as a tool for cell targeted delivery. *Nanoscale 9*, 647–655.

(72) Palombarini, F., Masciarelli, S., Incocciati, A., Liccardo, F., Di Fabio, E., Iazzetti, A., Fabrizi, G., Fazi, F., Macone, A., Bonamore, A., and Boffi, A. (2021) Self-assembling ferritin-dendrimer nanoparticles for targeted delivery of nucleic acids to myeloid leukemia cells. *J. Nanobiotechnology 19*, 172.

(73) Wang, S., Sun, S., Li, Z., Zhang, R., and Xu, J. (2017) Accurate De Novo Prediction of Protein Contact Map by Ultra-Deep Learning Model. *PLoS Comput. Biol. 13*, e1005324.

(74) Huang, J., Rauscher, S., Nawrocki, G., Ran, T., Feig, M., de Groot, B. L., Grubmüller, H., and MacKerell, A. D. J. (2017) CHARMM36m: an improved force field for folded and intrinsically disordered proteins. *Nat. Methods 14*, 71–73.

(75) Park, H., Bradley, P., Greisen, P. J., Liu, Y., Mulligan, V. K., Kim, D. E., Baker, D., and DiMaio, F. (2016) Simultaneous Optimization of Biomolecular Energy Functions on Features from Small Molecules and Macromolecules. *J. Chem. Theory Comput. 12*, 6201–6212.

(76) Jumper, J., Evans, R., Pritzel, A., Green, T., Figurnov, M., Ronneberger, O., Tunyasuvunakool, K., Bates, R., Žídek, A., Potapenko, A., Bridgland, A., Meyer, C., Kohl, S. A. A., Ballard, A. J., Cowie, A., Romera-Paredes, B., Nikolov, S., Jain, R., Adler, J., Back, T., Petersen, S., Reiman, D., Clancy, E., Zielinski, M., Steinegger, M., Pacholska, M., Berghammer, T., Bodenstein, S., Silver, D., Vinyals, O., Senior, A. W., Kavukcuoglu, K., Kohli, P., and Hassabis, D. (2021) Highly accurate protein structure prediction with AlphaFold. *Nature 596*, 583–589.

(77) Varadi, M., Anyango, S., Deshpande, M., Nair, S., Natassia, C., Yordanova, G., Yuan, D., Stroe, O., Wood, G., Laydon, A., Žídek, A., Green, T., Tunyasuvunakool, K., Petersen, S., Jumper, J., Clancy, E., Green, R., Vora, A., Lutfi, M., Figurnov, M., Cowie, A., Hobbs, N., Kohli, P., Kleywegt, G., Birney, E., Hassabis, D., and Velankar, S. (2022) AlphaFold Protein Structure Database: massively expanding the structural coverage of protein-sequence space with high-accuracy models. *Nucleic Acids Res. 50*, D439–D444.

(78) Arnold, F. H. (2018) Directed evolution: bringing new chemistry to life. *Angew. Chemie - Int. Ed. 57*, 4143–4148.

(79) Lapenta, F., Aupič, J., Vezzoli, M., Strmšek, Ž., Da Vela, S., Svergun, D. I., Carazo, J. M., Melero, R., and Jerala, R. (2021) Self-assembly and regulation of protein cages from pre-organised coiled-coil modules. *Nat. Commun. 12*, 939.

(80) King, N. P., Bale, J. B., Sheffler, W., McNamara, D. E., Gonen, S., Gonen, T., Yeates, T. O., and Baker, D. (2014) Accurate design of co-assembling multi-component protein nanomaterials. *Nature 510*, 103–108.

(81) Hsia, Y., Bale, J. B., Gonen, S., Shi, D., Sheffler, W., Fong, K. K., Nattermann, U., Xu, C., Huang, P.-S., Ravichandran, R., Yi, S., Davis, T. N., Gonen, T., King, N. P., and Baker, D. (2016) Design of a hyperstable 60-subunit protein icosahedron. *Nature 535*, 136–139.

(82) King, N. P., Sheffler, W., Sawaya, M. R., Vollmar, B. S., Sumida, J. P., André, I., Gonen, T., Yeates, T. O., and Baker, D. (2012) Computational design of self-assembling protein nanomaterials with atomic level accuracy. *Science 336*, 1171–1174.

(83) Quijano-Rubio, A., Yeh, H.-W., Park, J., Lee, H., Langan, R. A., Boyken, S. E., Lajoie, M. J., Cao, L., Chow, C. M., Miranda, M. C., Wi, J., Hong, H. J., Stewart, L., Oh, B.-H., and Baker, D. (2021) De novo design of modular and tunable protein biosensors. *Nature 591*, 482–487.

(84) Polizzi, N. F., and DeGrado, W. F. (2020) A defined structural unit enables de novo design of small-molecule–binding proteins. *Science (80-.). 369*, 1227–1233.

(85) Tinberg, C. E., Khare, S. D., Dou, J., Doyle, L., Nelson, J. W., Schena, A., Jankowski, W.,

Kalodimos, C. G., Johnsson, K., Stoddard, B. L., and Baker, D. (2013) Computational design of ligand-binding proteins with high affinity and selectivity. *Nature 501*, 212–216.

(86) Joh, N. H., Wang, T., Bhate, M. P., Acharya, R., Wu, Y., Grabe, M., Hong, M., Grigoryan, G., and DeGrado, W. F. (2014) De novo design of a transmembrane Zn^{2+}-transporting four-helix bundle. *Science 346*, 1520–1524.

(87) Votteler, J., Ogohara, C., Yi, S., Hsia, Y., Nattermann, U., Belnap, D. M., King, N. P., and Sundquist, W. I. (2016) Designed proteins induce the formation of nanocage-containing extracellular vesicles. *Nature 540*, 292–295.

(88) Ma, C., Malessa, A., Boersma, A. J., Liu, K., and Herrmann, A. (2020) Supercharged proteins and polypeptides. *Adv. Mater. 32*, 1905309.

(89) Lawrence, M. S., Phillips, K. J., and Liu, D. R. (2007) Supercharging proteins can impart unusual resilience. *J. Am. Chem. Soc. 129*, 10110–10112.

(90) McNaughton, B. R., Cronican, J. J., Thompson, D. B., and Liu, D. R. (2009) Mammalian cell penetration, siRNA transfection, and DNA transfection by supercharged proteins. *Proc. Natl. Acad. Sci. U. S. A. 106*, 6111–6116.

(91) Wang, L., Geng, J., Chen, L., Guo, X., Wang, T., Fang, Y., Belingon, B., Wu, J., Li, M., Zhan, Y., Shang, W., Wan, Y., Feng, X., Li, X., and Wang, H. (2022) Improved transfer efficiency of supercharged 36 + GFP protein mediate nucleic acid delivery. *Drug Deliv. 29*, 386–398.

(92) Miklos, A. E., Kluwe, C., Der, B. S., Pai, S., Sircar, A., Hughes, R. A., Berrondo, M., Xu, J., Codrea, V., Buckley, P. E., Calm, A. M., Welsh, H. S., Warner, C. R., Zacharko, M. A., Carney, J. P., Gray, J. J., Georgiou, G., Kuhlman, B., and Ellington, A. D. (2012) Structure-based design of supercharged, highly thermoresistant antibodies. *Chem. Biol. 19*, 449–455.

(93) Simeonov, P., Berger-Hoffmann, R., Hoffmann, R., Sträter, N., and Zuchner, T. (2011) Surface supercharged human enteropeptidase light chain shows improved solubility and refolding yield. *Protein Eng. Des. Sel. 24*, 261–268.

(94) Haarmeyer, C. N., Smith, M. D., Chundawat, S. P. S., Sammond, D., and Whitehead, T. A. (2017) Insights into cellulase-lignin non-specific binding revealed by computational redesign of the surface of green fluorescent protein. *Biotechnol. Bioeng. 114*, 740–750.

(95) Whitehead, T. A., Bandi, C. K., Berger, M., Park, J., and Chundawat, S. P. S. (2017) Negatively supercharging cellulases render them lignin-resistant. *ACS Sustain. Chem. Eng. 5*, 6247–6252.

(96) Johnson, L. B., Park, S., Gintner, L. P., and Snow, C. D. (2016) Characterization of supercharged cellulase activity and stability in ionic liquids. *J. Mol. Catal. B Enzym. 132*, 84–90.

(97) Cronican, J. J., Thompson, D. B., Beier, K. T., McNaughton, B. R., Cepko, C. L., and Liu, D. R. (2010) Potent delivery of functional proteins into mammalian cells in vitro and in vivo using a supercharged protein. *ACS Chem. Biol. 5*, 747–752.

(98) Wang, M., Zuris, J. A., Meng, F., Rees, H., Sun, S., Deng, P., Han, Y., Gao, X., Pouli, D., Wu, Q.,

Georgakoudi, I., Liu, D. R., and Xu, Q. (2016) Efficient delivery of genome-editing proteins using bioreducible lipid nanoparticles. *Proc. Natl. Acad. Sci. U. S. A. 113*, 2868–2873.

(99) Sasaki, E., Böhringer, D., Van De Waterbeemd, M., Leibundgut, M., Zschoche, R., Heck, A. J. R., Ban, N., and Hilvert, D. (2017) Structure and assembly of scalable porous protein cages. *Nat. Commun. 8*, 14663.

(100) Clark, J., and Macquarrie, D. (2007) Handbook of green chemistry and technology. *Handb. Green Chem. Technol.*

(101) Zaks, A., and Klibanov, A. M. (1984) Enzymatic catalysis in organic media at 100°C. *Science (80-.). 224*, 1249–51.

(102) Burton, S. G., Cowan, D. A., and Woodley, J. M. (2002) The search for the ideal biocatalyst. *Nat. Biotechnol. 20*, 37–45.

(103) Reetz, M. T. (2013) Biocatalysis in organic chemistry and biotechnology: Past, present, and future. *J. Am. Chem. Soc. 135*, 12480–12496.

(104) Woodley, J. M. (2013) Protein engineering of enzymes for process applications. *Curr. Opin. Chem. Biol. 17*, 310–316.

(105) Turner, N. J., and O'reilly, E. (2013) Biocatalytic retrosynthesis. *Nat. Chem. Biol. 9*, 285–288.

(106) Sheldon, R. A., and Pereira, P. C. (2017) Biocatalysis engineering: The big picture. *Chem. Soc. Rev. 46*, 2678–2691.

(107) Denard, C. A., Ren, H., and Zhao, H. (2015) Improving and repurposing biocatalysts via directed evolution. *Curr. Opin. Chem. Biol. 25*, 55–64.

(108) Sheldon, R. A., Brady, D., and Bode, M. L. (2020) The Hitchhiker's guide to biocatalysis: Recent advances in the use of enzymes in organic synthesis. *Chem. Sci. 11*, 2587–2605.

(109) Qu, G., Liu, B., Jiang, Y., Nie, Y., Yu, H., and Sun, Z. (2019) Laboratory evolution of an alcohol dehydrogenase towards enantioselective reduction of difficult-to-reduce ketones. *Bioresour. Bioprocess. 6*, 18.

(110) Nanda, V., Senn, S., Pike, D. H., Rodriguez-Granillo, A., Hansen, W. A., Khare, S. D., and Noy, D. (2016) Structural principles for computational and de novo design of 4Fe-4S metalloproteins. *Biochim. Biophys. Acta - Bioenerg. 1857*, 531–538.

(111) Rittle, J., Field, M. J., Green, M. T., and Tezcan, F. A. (2019) An efficient, step-economical strategy for the design of functional metalloproteins. *Nat. Chem. 11*, 434–441.

(112) Hayashi, T., Hilvert, D., and Green, A. P. (2018) Engineered metalloenzymes with non-canonical coordination environments. *Chem. - A Eur. J. 24*, 11821–11830.

(113) Lu, C., Shen, F., Wang, S., Wang, Y., Liu, J., Bai, W. J., and Wang, X. (2018) An engineered self-sufficient biocatalyst enables scalable production of linear α-olefins from carboxylic acids.

ACS Catal. 8, 5794–5798.

(114) Stenner, R., Steventon, J. W., Seddon, A., and Anderson, J. L. R. (2020) A de novo peroxidase is also a promiscuous yet stereoselective carbene transferase. *Proc. Natl. Acad. Sci. U. S. A. 117*, 1419–1428.

(115) Fessner, N. D. (2019) P450 monooxygenases enable rapid late-stage diversification of natural products via C−H bond activation. *ChemCatChem 11*, 2226–2242.

(116) Seel, C. J., and Gulder, T. (2019) Biocatalysis fueled by light: On the versatile combination of photocatalysis and enzymes. *ChemBioChem 20*, 1871–1897.

(117) Li, P., Chen, Q., Wang, T. C., Vermeulen, N. A., Mehdi, B. L., Dohnalkova, A., Browning, N. D., Shen, D., Anderson, R., Gómez-Gualdrón, D. A., Cetin, F. M., Jagiello, J., Asiri, A. M., Stoddart, J. F., and Farha, O. K. (2018) Hierarchically engineered mesoporous metal-organic frameworks toward cell-free immobilized enzyme systems. *Chem 4*, 1022–1034.

(118) Chen, Y., Jiménez-Ángeles, F., Qiao, B., Krzyaniak, M. D., Sha, F., Kato, S., Gong, X., Buru, C. T., Chen, Z., Zhang, X., Gianneschi, N. C., Wasielewski, M. R., Olvera de la Cruz, M., and Farha, O. K. (2020) Insights into the enhanced catalytic activity of cytochrome c when encapsulated in a metal–organic framework. *J. Am. Chem. Soc. 142*, 18576–18582.

(119) Lee, C. H., Jin, E. S., Lee, J. H., and Hwang, E. T. (2020) Immobilization and stabilization of enzyme in biomineralized calcium carbonate microspheres. *Front. Bioeng. Biotechnol. 8*, 1191.

(120) Das, S., Zhao, L., Elofson, K., and Finn, M. G. (2020) Enzyme stabilization by virus-like particles. *Biochemistry 59*, 2870–2881.

(121) Guzik, U., Hupert-Kocurek, K., and Wojcieszyńska, D. (2014) Immobilization as a strategy for improving enzyme properties-application to oxidoreductases. *Molecules 19*, 8995–9018.

(122) Pedersen, J. N., Zhou, Y., Guo, Z., and Pérez, B. (2019) Genetic and chemical approaches for surface charge engineering of enzymes and their applicability in biocatalysis: A review. *Biotechnol. Bioeng. 116*, 1795–1812.

(123) Rochelle, G. T. (2009) Amine scrubbing for CO2 capture. *Science (80-.). 325*, 1652–1654.

(124) Snæbjörnsdóttir, S. Ó., Sigfússon, B., Marieni, C., Goldberg, D., Gislason, S. R., and Oelkers, E. H. (2020) Carbon dioxide storage through mineral carbonation. *Nat. Rev. Earth Environ. 1*, 90–102.

(125) Singh, J., and Dhar, D. W. (2019) Overview of carbon capture technology: Microalgal biorefinery concept and state-of-the-art. *Front. Mar. Sci. 6*, 29.

(126) Qasem, N. A. A., Ben-Mansour, R., and Habib, M. A. (2018) An efficient CO2 adsorptive storage using MOF-5 and MOF-177. *Appl. Energy 210*, 317–326.

(127) Britt, D., Furukawa, H., Wang, B., Glover, T. G., and Yaghi, O. M. (2009) Highly efficient separation of carbon dioxide by a metal-organic framework replete with open metal sites. *Proc.*

Natl. Acad. Sci. U. S. A. 106, 20637–20640.

(128) Shao, L., Sang, Y., Huang, J., and Liu, Y. N. (2018) Triazine-based hyper-cross-linked polymers with inorganic-organic hybrid framework derived porous carbons for CO2 capture. *Chem. Eng. J. 353*, 1–14.

(129) Wang, W., Zhou, M., and Yuan, D. (2017) Carbon dioxide capture in amorphous porous organic polymers. *J. Mater. Chem. A 5*, 1334–1347.

(130) Basnayake, S. A., Su, J., Zou, X., and Balkus, K. J. (2015) Carbonate-based zeolitic imidazolate framework for highly selective co2 capture. *Inorg. Chem. 54*, 1816–1821.

(131) Krishnamurthy, V. M., Kaufman, G. K., Urbach, A. R., Gitlin, I., Gudiksen, K. L., Weibel, D. B., and Whitesides, G. M. (2008) Carbonic anhydrase as a model for biophysical and physical-organic studies of proteins and protein-ligand binding. *Chem. Rev. 108*, 946–1051.

(132) Effendi, S. S. W., and Ng, I. S. (2019) The prospective and potential of carbonic anhydrase for carbon dioxide sequestration: A critical review. *Process Biochem. 87*, 55–65.

(133) Vinoba, M., Bhagiyalakshmi, M., Jeong, S. K., Yoon, Y. I. I., and Nam, S. C. (2012) Immobilization of carbonic anhydrase on spherical SBA-15 for hydration and sequestration of CO 2. *Colloids Surfaces B Biointerfaces 90*, 91–96.

(134) Jing, G., Pan, F., Lv, B., and Zhou, Z. (2015) Immobilization of carbonic anhydrase on epoxy-functionalized magnetic polymer microspheres for CO2 capture. *Process Biochem. 50*, 2234–2241.

(135) Kanbar, B., and Ozdemir, E. (2010) Thermal stability of carbonic anhydrase immobilized within polyurethane foam. *Biotechnol. Prog. 26*, 1474–1480.

(136) Bilal, M., Asgher, M., Shahid, M., and Bhatti, H. N. (2016) Characteristic features and dye degrading capability of agar-agar gel immobilized manganese peroxidase. *Int. J. Biol. Macromol. 86*, 728–740.

(137) Min, K. H., Son, R. G., Ki, M. R., Choi, Y. S., and Pack, S. P. (2016) High expression and biosilica encapsulation of alkaline-active carbonic anhydrase for CO2 sequestration system development. *Chemosphere 143*, 128–134.

(138) Seebeck, F. P., Woycechowsky, K. J., Zhuang, W., Rabe, J. P., and Hilvert, D. (2006) A simple tagging system for protein encapsulation. *J. Am. Chem. Soc. 128*, 4516–4517.

(139) Pulsipher, K. W., and Dmochowski, I. J. (2014) Ferritin encapsulation and templated synthesis of inorganic nanoparticles, in *Protein Cages: Methods and Protocols*, pp 27–37.

(140) Pulsipher, K. W., and Dmochowski, I. J. (2016) Ferritin: Versatile host, nanoreactor, and delivery agent. *Isr. J. Chem. 56*, 660–670.

(141) Kim, C. S., Yang, Y. J., Bahn, S. Y., and Cha, H. J. (2017) A bioinspired dual-crosslinked tough silk protein hydrogel as a protective biocatalytic matrix for carbon sequestration. *NPG Asia*

Mater. 9, e391.

(142) Jo, B. H., Seo, J. H., Yang, Y. J., Baek, K., Choi, Y. S., Pack, S. P., Oh, S. H., and Cha, H. J. (2014) Bioinspired silica nanocomposite with autoencapsulated carbonic anhydrase as a robust biocatalyst for CO2 sequestration. *ACS Catal. 4*, 4332–4340.

(143) Guo, H. H., Choe, J., and Loeb, L. A. (2004) Protein tolerance to random amino acid change. *Proc. Natl. Acad. Sci. U. S. A. 101*, 9205–9210.

(144) Rennell, D., Bouvier, S. E., Hardy, L. W., and Poteete, A. R. (1991) Systematic mutation of bacteriophage T4 lysozyme. *J. Mol. Biol. 222*, 67–86.

(145) Axe, D. D., Foster, N. W., and Fersht, A. R. (1998) A search for single substitutions that eliminate enzymatic function in a bacterial ribonuclease. *Biochemistry 37*, 7157–7166.

(146) Haarmeyer, C. N., Smith, M. D., Chundawat, S. P. S., Sammond, D., and Whitehead, T. A. (2017) Insights into cellulase-lignin non-specific binding revealed by computational redesign of the surface of green fluorescent protein. *Biotechnol. Bioeng. 114*, 740–750.

(147) Whitehead, T. A., Bandi, C. K., Berger, M., Park, J., and Chundawat, S. P. S. (2017) Negatively supercharging cellulases render them lignin-resistant. *ACS Sustain. Chem. Eng. 5*, 6247–6252.

(148) Kono, H., and Saven, J. G. (2001) Statistical theory for protein combinatorial libraries. Packing interactions, backbone flexibility, and the sequence variability of a main-chain structure. *J. Mol. Biol. 306*, 607–628.

(149) Swift, J., Wehbi, W. A., Kelly, B. D., Stowell, X. F., Saven, J. G., and Dmochowski, I. J. (2006) Design of functional ferritin-like proteins with hydrophobic cavities. *J. Am. Chem. Soc. 128*, 6611–6619.

(150) Diaz, J. E., Lin, C.-S., Kunishiro, K., Feld, B. K., Avrantinis, S. K., Bronson, J., Greaves, J., Saven, J. G., and Weiss, G. A. (2011) Computational design and selections for an engineered, thermostable terpene synthase. *Protein Sci. 20*, 1597–1606.

(151) Perez-Aguilar, J. M., Xi, J., Matsunaga, F., Cui, X., Selling, B., Saven, J. G., and Liu, R. (2013) A Computationally Designed Water-Soluble Variant of a G-Protein-Coupled Receptor: The Human Mu Opioid Receptor. *PLoS One 8*, e66009.

(152) Fraczkiewicz, R., and Braun, W. (1998) Exact and efficient analytical calculation of the accessible surface areas and their gradients for macromolecules. *J. Comput. Chem. 19*, 319–333.

(153) Behnke, C. A., Le Trong, I., Godden, J. W., Merritt, E. A., Teller, D. C., Bajorath, J., and Stenkamp, R. E. (2010) Atomic resolution studies of carbonic anhydrase II. *Acta Crystallogr. D. Biol. Crystallogr. 66*, 616–627.

(154) Calhoun, J. R., Kono, H., Lahr, S., Wang, W., DeGrado, W. F., and Saven, J. G. (2003) Computational design and characterization of a monomeric helical dinuclear metalloprotein. *J. Mol. Biol. 334*, 1101–1115.

(155) Gasteiger, E., Hoogland, C., Gattiker, A., Duvaud, S., Wilkins, M. R., Appel, R. D., and Bairoch, A. (2005) Protein identification and analysis tools on the ExPASy server, in *The Proteomics Protocols Handbook*, pp 571–607.

(156) Wang, Y., Roose, B. W., Philbin, J. P., Doman, J. L., and Dmochowski, I. J. (2016) Programming A molecular relay for ultrasensitive biodetection through 129XeNMR. *Angew. Chemie - Int. Ed. 55*, 1733–1736.

(157) Anderson, J., Byrne, T., Woelfel, K. J., Meany, J. E., Spyridis, G. T., and Pocker, Y. (1994) The hydrolysis of p-nitrophenyl acetate: A versatile reaction to study enzyme kinetics. *J. Chem. Educ. 71*, 715.

(158) Khalameyzer, V., Fischer, I., Bornscheuer, U. T., and Altenbuchner, J. (1999) Screening, nucleotide sequence, and biochemical characterization of an esterase from Pseudomonas fluorescens with high activity towards lactones. *Appl. Environ. Microbiol. 65*, 477–482.

(159) Avvaru, B. S., Kim, C. U., Sippel, K. H., Gruner, S. M., Agbandje-McKenna, M., Silverman, D. N., and McKenna, R. (2010) A short, strong hydrogen bond in the active site of human carbonic anhydrase II. *Biochemistry 49*, 249–251.

(160) Hovmöller, S., Zhou, T., and Ohlson, T. (2002) Conformations of amino acids in proteins. *Acta Crystallogr. Sect. D Biol. Crystallogr. D58*, 768–776.

(161) Jurrus, E., Engel, D., Star, K., Monson, K., Brandi, J., Felberg, L. E., Brookes, D. H., Wilson, L., Chen, J., Liles, K., Chun, M., Li, P., Gohara, D. W., Dolinsky, T., Konecny, R., Koes, D. R., Nielsen, J. E., Head-Gordon, T., Geng, W., Krasny, R., Wei, G.-W., Holst, M. J., McCammon, J. A., and Baker, N. A. (2018) Improvements to the APBS biomolecular solvation software suite. *Protein Sci. 27*, 112–128.

(162) Humphrey, W., Dalke, A., and Schulten, K. (1996) VMD: Visual molecular dynamics. *J. Mol. Graph. 14*, 33–38.

(163) Comellas-Aragonès, M., Engelkamp, H., Claessen, V. I., Sommerdijk, N. A. J. M., Rowan, A. E., Christianen, P. C. M., Maan, J. C., Verduin, B. J. M., Cornelissen, J. J. L. M., and Nolte, R. J. M. (2007) A virus-based single-enzyme nanoreactor. *Nat. Nanotechnol. 2*, 635–639.

(164) Zucca, P., Fernandez-Lafuente, R., and Sanjust, E. (2016) Agarose and its derivatives as supports for enzyme immobilization. *Molecules 21*, 1577.

(165) Lian, X., Erazo-Oliveras, A., Pellois, J.-P., and Zhou, H.-C. (2017) High efficiency and long-term intracellular activity of an enzymatic nanofactory based on metal-organic frameworks. *Nat. Commun. 8*, 2075.

(166) Gawande, P. V, and Kamat, M. Y. (1998) Preparation, characterization and application of Aspergillus sp. xylanase immobilized on Eudragit S-100. *J. Biotechnol. 66*, 165–175.

(167) Mazlan, S. Z., and Hanifah, S. A. (2017) Effects of temperature and pH on immobilized laccase activity in conjugated methacrylate-acrylate microspheres. *Int. J. Polym. Sci.* (Schnabelrauch, M., Ed.) *2017*, 5657271.

(168) Homaei, A. A., Sajedi, R. H., Sariri, R., Seyfzadeh, S., and Stevanato, R. (2010) Cysteine enhances activity and stability of immobilized papain. *Amino Acids 38*, 937–942.

(169) Azuma, Y., Zschoche, R., Tinzl, M., and Hilvert, D. (2016) Quantitative packaging of active enzymes into a protein cage. *Angew. Chemie - Int. Ed. 55*, 1531–1534.

(170) Cannon, K. A., Park, R. U., Boyken, S. E., Nattermann, U., Yi, S., Baker, D., King, N. P., and Yeates, T. O. (2020) Design and structure of two new protein cages illustrate successes and ongoing challenges in protein engineering. *Protein Sci. 29*, 919–929.

(171) Jones, J. A., Cristie-David, A. S., Andreas, M. P., and Giessen, T. W. (2021) Triggered Reversible Disassembly of an Engineered Protein Nanocage**. *Angew. Chemie Int. Ed. 60*, 25034–25041.

(172) Pekarik, V., Peskova, M., Guran, R., Novacek, J., Heger, Z., Tripsianes, K., Kumar, J., and Adam, V. (2017) Visualization of stable ferritin complexes with palladium, rhodium and iridium nanoparticles detected by their catalytic activity in native polyacrylamide gels. *Dalt. Trans. 46*, 13690–13694.

(173) Peskova, M., Ilkovics, L., Hynek, D., Dostalova, S., Sanchez-Carnerero, E. M., Remes, M., Heger, Z., and Pekarik, V. (2019) Detergent-modified catalytic and enzymomimetic activity of silver and palladium nanoparticles biotemplated by Pyrococcus furiosus ferritin. *J. Colloid Interface Sci. 537*, 20–27.

(174) Yamashita, I. (2001) Fabrication of a two-dimensional array of nano-particles using ferritin molecule. *Thin Solid Films 393*, 12–18.

(175) Yoshimura, H. (2006) Protein-assisted nanoparticle synthesis. *Colloids Surfaces A Physicochem. Eng. Asp. 282–283*, 464–470.

(176) Hennequin, B., Turyanska, L., Ben, T., Beltrán, A. M., Molina, S. I., Li, M., Mann, S., Patanè, A., and Thomas, N. R. (2008) Aqueous Near-Infrared Fluorescent Composites Based on Apoferritin-Encapsulated PbS Quantum Dots. *Adv. Mater. 20*, 3592–3596.

(177) Sato, D., Takebe, S., Kurobe, A., Ohtomo, H., Fujiwara, K., and Ikeguchi, M. (2016) Electrostatic repulsion during ferritin assembly and its screening by ions. *Biochemistry 55*, 482–488.

(178) Dayel, M. J., Hom, E. F., and Verkman, A. S. (1999) Diffusion of green fluorescent protein in the aqueous-phase lumen of endoplasmic reticulum. *Biophys. J. 76*, 2843–2851.

(179) Swaminathan, R., Hoang, C. P., and Verkman, A. S. (1997) Photobleaching recovery and anisotropy decay of green fluorescent protein GFP-S65T in solution and cells: cytoplasmic viscosity probed by green fluorescent protein translational and rotational diffusion. *Biophys. J. 72*, 1900–1907.

(180) Tang, J., Jofre, A. M., Lowman, G. M., Kishore, R. B., Reiner, J. E., Helmerson, K., Goldner, L. S., and Greene, M. E. (2008) Green Fluorescent Protein in Inertially Injected Aqueous Nanodroplets. *Langmuir 24*, 4975–4978.

(181) Korobko, I., Mazal, H., Haran, G., and Horovitz, A. (2020) Measuring protein stability in the GroEL chaperonin cage reveals massive destabilization. *Elife* (Kay, L. E., Ron, D., and Thirumalai, D., Eds.) *9*, e56511.

(182) Smith, T. A., and Ghiggino, K. P. (2015) A review of the analysis of complex time-resolved fluorescence anisotropy data. *Methods Appl. Fluoresc. 3*, 22001.

(183) Guo, R., Sinha, N. J., Misra, R., Tang, Y., Langenstein, M., Kim, K., Fagan, J. A., Kloxin, C. J., Jensen, G., Pochan, D. J., and Saven, J. G. (2022) Computational Design of Homotetrameric Peptide Bundle Variants Spanning a Wide Range of Charge States. *Biomacromolecules 23*, 1652–1661.

(184) Villegas, J. A., Sinha, N. J., Teramoto, N., Von Bargen, C. D., Pochan, D. J., and Saven, J. G. (2022) Computational Design of Single-Peptide Nanocages with Nanoparticle Templating. *Molecules 27*.

(185) Wand, A. J., Ehrhardt, M. R., and Flynn, P. F. (1998) High-resolution NMR of encapsulated proteins dissolved in low-viscosity fluids. *Proc. Natl. Acad. Sci. U. S. A. 95*, 15299–15302.

(186) Koldewey, P., Stull, F., Horowitz, S., Martin, R., and Bardwell, J. C. A. (2016) Forces Driving Chaperone Action. *Cell 166*, 369–379.

(187) Gibson, D. G., Young, L., Chuang, R.-Y., Venter, J. C., Hutchison, C. A., and Smith, H. O. (2009) Enzymatic assembly of DNA molecules up to several hundred kilobases. *Nat. Methods 6*, 343–345.

(188) Fiore, K. E., Phan, H. A. T., Robkis, D. M., Walters, C. R., and Petersson, E. J. (2021) Incorporating thioamides into proteins by native chemical ligation. *Methods Enzymol. 656*, 295–339.

(189) Ma, X., Zou, F., Yu, F., Li, R., Yuan, Y., Zhang, Y., Zhang, X., Deng, J., Chen, T., Song, Z., Qiao, Y., Zhan, Y., Liu, J., Zhang, J., Zhang, X., Peng, Z., Li, Y., Lin, Y., Liang, L., Wang, G., Chen, Y., Chen, Q., Pan, T., He, X., and Zhang, H. (2020) Nanoparticle Vaccines Based on the Receptor Binding Domain (RBD) and Heptad Repeat (HR) of SARS-CoV-2 Elicit Robust Protective Immune Responses. *Immunity 53*, 1315-1330.e9.

(190) Imlay, K. R. C., and Imlay, J. A. (1996) Cloning and analysis of sodC, encoding the copper-zinc superoxide dismutase of Escherichia coli. *J. Bacteriol. 178*, 2564–2571.

(191) Talapin, D. V., and Shevchenko, E. V. (2016) Introduction: Nanoparticle Chemistry. *Chem. Rev. 116*, 10343–10345.

(192) Jones, M. R., Seeman, N. C., and Mirkin, C. A. (2015) Programmable materials and the nature of the DNA bond. *Science (80-.). 347*, 1260901.

(193) Robertson, J. D., Rizzello, L., Avila-Olias, M., Gaitzsch, J., Contini, C., Magoń, M. S., Renshaw, S. A., and Battaglia, G. (2016) Purification of Nanoparticles by Size and Shape. *Sci. Rep. 6*, 27494.

(194) Krammer, F. (2020) SARS-CoV-2 vaccines in development. *Nature 586*, 516–527.

(195) Yarmarkovich, M., Warrington, J. M., Farrel, A., and Maris, J. M. (2020) Identification of SARS-CoV-2 Vaccine Epitopes Predicted to Induce Long-Term Population-Scale Immunity. *Cell Reports Med. 1*, 100036.